Universität Konstanz

Masterthesis

Master-Arbeit

Investigation of photonic band gaps with special emphasis on hyperuniform structures

Untersuchung photonischer Bandlücken mit Schwerpunkt auf hyperuniformen Strukturen

submitted by
Lukas Siedentop

supervised by
Prof. Dr. Georg Maret
Priv. Doz. Dr. Peter Keim

2. May 2016

Title image: Covert feather of an *Agapornis roseicollis* which gains its green color from yellow pigments combined with a blue, supposedly hyperuniform structure.

Contents

1. Introduction

Today's digital technology is based on electronic semi-conductors and lives from constant improvement, made possible by the ever smaller miniaturisation of electronic transistors. A huge industry, driven by consumers demand, ensures Moore's law, which states that the transistor density doubles every one or two years [1]. In not so distant future, however, further miniaturisation will face fundamental physical limits, enforced by the very nature of the particle involve: the electron. Problems with heat dissipation and signal propagation delays already prohibit progress in computational performance [2]. Apparently, a leap in technology is necessary once again, as it happened in the 1950s, when solid-state devices started to replaced electron tubes step-by-step.

The main draw back of technologies based on electrons is the fermionic nature of the electron. Due to the Pauli principle, electrons are not allowed to be in the same quantum state, prohibiting infinite miniaturisation. Furthermore, the electrons charge leads to induction of and interaction with magnetic and electric fields, yielding hard to control mutual interaction, especially when miniaturisation reaches distances as small as a few atom diameters across. Photons on the contrary, being bosons, are very well allowed in the same quantum state. Already, optical devices begin to replace electronic devices. One can think of optical fibres, providing an effective transport of information across oceans. To omit converters that are still necessary to transform electronic to optical signals and vice versa, the development of all-optical integrated circuits is the logical consequence [3].

To enable exciting new possibilities with photons, like quantum computation [4], guidance of the photons is needed. Plasmonic devices are realisable at the relevant telecommunication wavelengths [5], but posses high loss if short wavelengths need to be guided [6]. In 1987, Eli Yablonovitch and Sajeev John published two groundbreaking articles. They postulated materials that posses not an electronic but a photonic band gap. With these, the spontaneous emission could be inhibited [7] or photons could be strongly localised [8], yielding a kind of Anderson localisation [9]. Today, these materials count to the class of photonic meta materials that posses fascinating optical properties [10]. The secret of these materials lies in their micro- or nano-structuring, being the origin of peculiar effects like negative refraction or perfect absorption.

With regards to waveguides for photons, the photonic band gap is of special interest. Light of a specific frequency has a probability density function of exactly zero in such meta materials. By surrounding a volume with this material, any electromagnetic wave of this frequency is tightly confined to this very volume. Two dimensional photonic crystals are already used in state-of-the-art optical fibres, that confine the light with minimal absorption loss [11]. The concept is adapted from the theory of the band gaps in solid-state physics, for which reason photonic band gap materials are sometimes

dubbed “semi-conductors of light” [12]. Theoretically well understood are band gaps that occur in crystalline structures. There, the band gap width is dependant on the direction of the electron or photon, respectively, making the gap anisotropic. This gives constraints on the design of waveguides in those meta materials.

Propagation of waves in amorphous materials is theoretically far more challenging [13, 14]. Nevertheless, these random structures can also posses a band gap, in the electronic [15] and the photonic case [16]. New concepts had to be developed in order to explain the band gap formation in these media. Simple Bragg scattering can not serve as an explanation, as it does for crystal structures. How can one tell whether a random structure possesses a band gap? A classification of the random structures was needed, and the hyperuniformity emerged as an order metric. It is the property of vanishing density fluctuations in the large distance limit [17]. With amorphous, hyperuniform meta materials, it is possible to realise free form waveguides. This has already been proven for microwaves in the two dimensional case [18]. Three dimensional, amorphous structures that posses a photonic band gap have also already been found [19, 20].

As often the case, a glimpse at colourful mother nature is worthwhile. Raman noted already in 1934, that pigments are not always the cause for colour [21]. Another class of colours exist, the structural colours. Through interference of the visible light at complicated structures, flamboyant colours emerge. Those can be iridescent like the colour sometimes seen in fresh meat. There, multilayer interference occurs in muscle fibres [22, 23], causing destructive and constructive interference. This is much like a distributed Bragg reflector, which can be seen as a one dimensional photonic crystal. These structures could already be used to change the colour appearance of perovskite solar cells, making them more attractive for application [24]. Also, non-iridescent structural colours exist. Mostly, they origin from randomly arranged spherical particles [25, 26]. However, sponge like structures exist [27] as well, formed by a network of cylinders. The macaws are on example species which gains its beauty from random network structures [28]. To reproduce these structural colour is quite challenging, as the involved length scales are rather small. Typically, for a photonic band gap material with its characteristic length, the gap emerges for light of wavelengths approximately four times this length.

In the present thesis, the lead from Dirk Ropers [29] and Phillip Knappes [30] work is taken and the search for methods to investigate and moreover artificially fabricate amorphous photonic band gap material is pursued. The thesis at hand can be seen as a tool box with the aim to understand, fabricate and characterise materials with optical properties due to the structure of the material. In particular, a photonic band gap is desired, a range of frequencies where no propagation of light is allowed. The target band gap is in the near infra red, with regards to future applications. The first chapters shortly reviews the underlying theoretical concepts. In the next chapters the actual tools and experiments for simulation, fabrication and characterisation are discussed, already with an outlook for future work and ideas. Finally, in the last chapter, to which the impatient reader may be directed to, results are presented and discussed. This work may function as a foundation for future research and is far from being finished. Many tools are tested in a proof of concept manner and further fine tuning is essential to make this a powerful collection of useful instruments.

2. Theoretical Background

Band gap materials are closely related to *structural colours*. Contrary to pigments, they gain their wavelength selectivity by peculiar interference mechanisms due to spatial distribution variation of a refractive index material. Periodic and non-periodic examples can be found in nature which are briefly reviewed. Currently, no algorithm or protocol exists to produce an amorphous structure exhibiting a band gap, giving reason to investigate the structural colours. With this background, the physical theory is summarised, helping to understand the following experiments with photonic materials.

2.1. Structural Colour in Nature

There exists a vast amount of structural colour in nature. The materials are in principle photonic structures exhibiting at least a band stop at the wavelength corresponding to the colour of the structure. These structural colours reflect a certain spectrum of the incoming light, thus work fundamentally different to pigments, which absorb parts of the lights spectrum. Structural colours have the advantage not to fade in time, as no energy is absorbed that could eventually destroy colouring molecules. This is especially important for light of blue colour, i.e. high energy photons or short wavelengths, respectively. The short wavelengths give need for delicate and small structures in order to render possible destructive interference in a way, that propagation within the medium is disallowed and thus reflectance takes place. It is this reflectance that not only gives the colour a high stability, but also makes those colours strikingly flamboyant. It is thus no wonder that many animals use them for mating purposes.

During evolution nature assembled many different forms of such structural colour. As already done by Raman in 1934 [21], they can be divided in two classes, the iridescent and the non-iridescent ones. A small range of examples for iridescent colours is shown in Figure 2.1, ranging from the *pollia condensata* fruit a), b) over beetles c), d) and butterflies e)-j) to maritime bacteria k), shown in a Petri dish. For iridescent structural colours, the reflected wavelength or colour strongly depends on the orientation of the structure, giving a very colourful appearance. This is much like the behaviour of a distributed Bragg reflector and in fact, the origin of this appearance is often multibeam interference at parallel layers of different refractive index materials. As the reflected wavelength depends on the refractive index contrast of the materials, this wavelength changes by substituting one of the materials. For example, air voids can be filled with a liquid with a higher refractive index. The effects are shown in Figure 2.1 at the pure butterfly wings in e), f) versus the wings soaked with ethanol in i), j). This is an easy way to test whether a colour has structural origin. Another way is to grind or mill the

substance to a fine dust. If colour is still present despite the structure being destroyed, structural origin can be excluded.

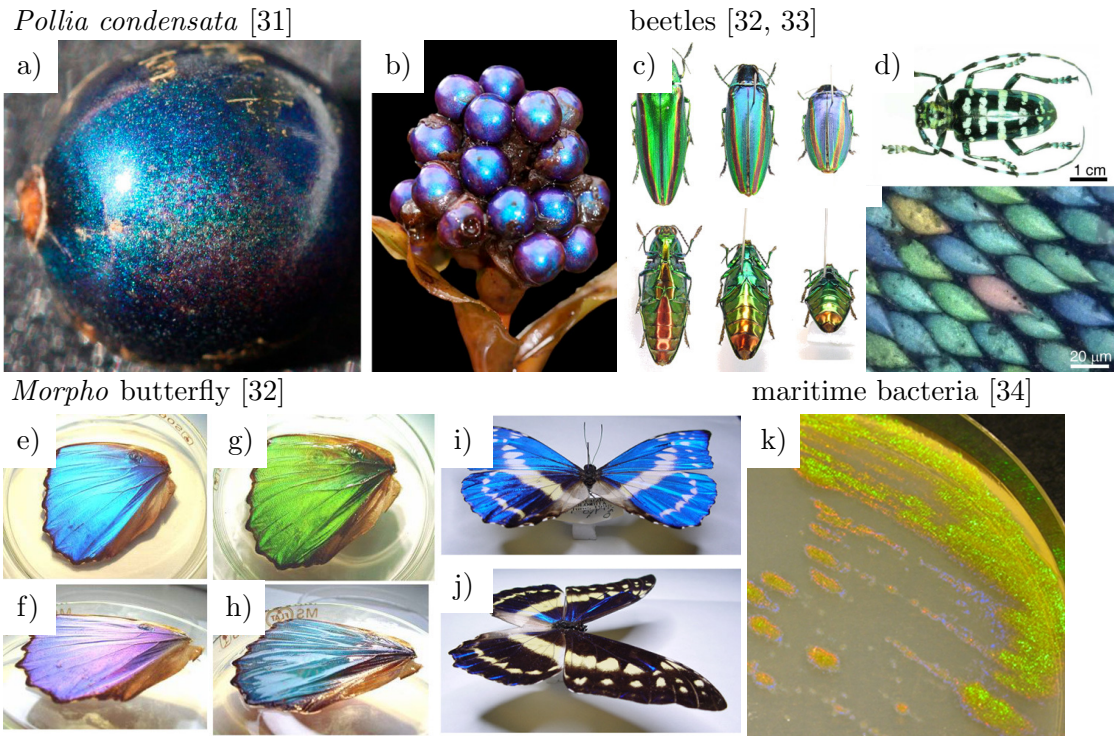

Figure 2.1.: Collage of some iridescent structural colours found in nature. The specimen show different colours dependant on the structures orientation. The change in colour for different refractive index contrast can be seen at the ethanol soaked *Morpho* specimen.

The other class of structural colours are the non-iridescent ones. A collage is shown in Figure 2.2, ranging from various birds a)-c) over mammals such as the mandrill d) or Robinson's mouse opossum e) to insects f). There, the reflected colour is independent of the specimens orientation. In order to produce this effect, the structure needs to be isotropic, i.e. amorphous. These structures are the most interesting ones for this work as they can not be described theoretically as easy as the non-iridescent ones. Some sort of multibeam interference takes place, as these specimen behave the same as the iridescent ones when milled or infiltrated with e.g. ethanol. But the origin is a disordered structure rather than periodically arranged layers. Figure 2.3 shows the amorphous, colour giving structure of a *agapornis roseicollis* in greater detail. For several reasons, the non-iridescent colour of this bird is of special interest in this work. First, the colour stems from an amorphous keratin network in air, whereby the network is bi-continuous and possibly similar to its inverse. Then, the refractive index of keratin, surprisingly low with $n_{\text{keratin}} \approx 1.54$ at $\lambda = 600\,\text{nm}$ [35, 36], is well known. Differences between various

bird species are neglected here.

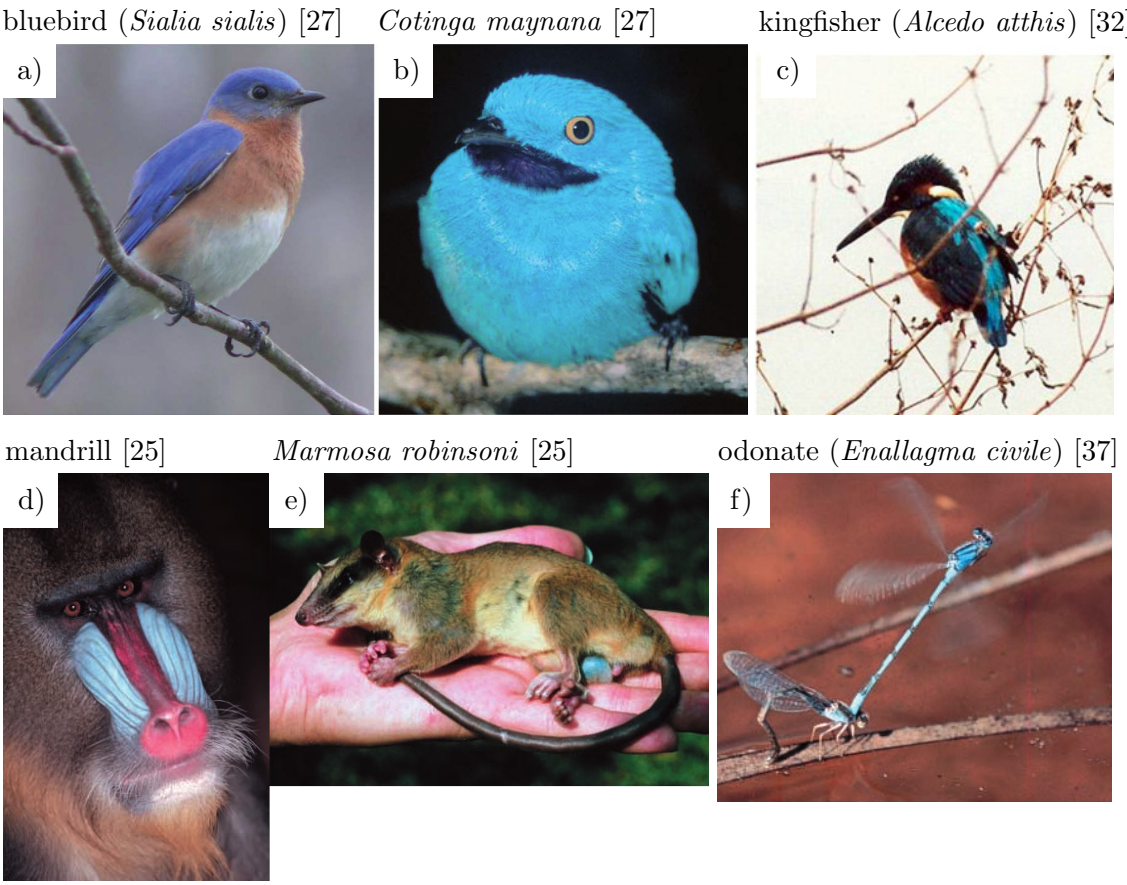

Figure 2.2.: Examples of non-iridescent structural colours found in nature. As feathers of birds are easily accessible, those are chosen as the objects of interest in this work. Nevertheless, structural iridescent colours also occur in many other colourful animals, ranging from bacteria over mammals and birds to insects.

Structural colours have fascinated many scientists, biologists as well as physicists, and thus many articles and reviews exist, e.g. Kinoshita *et. al.* [32] just to name one. A lot of research was done to identify structures as the origin of colour. With the help of scanning electron microscopes (SEM) it became a matter of finding and preparing a suitable sample to determine the structure. Also, electron tomography and transmission electron microscopy are often used as tools. Furthermore, the Fourier transform of the images [25–27, 36–39] can reveal characteristic directions and lengths, if present. If one or multiple rings are present in the Fourier transformed image, the sample exhibits a characteristic length with the inverse radius of the ring and is furthermore isotropic. Any anisotropy would appear as deformed rings or separated peaks. Such a ring can be seen in Figure 2.4, calculated from the bottom left image shown in Figure 2.3. There, it

is also depicted where exactly the structure can be found in the birds feathers.

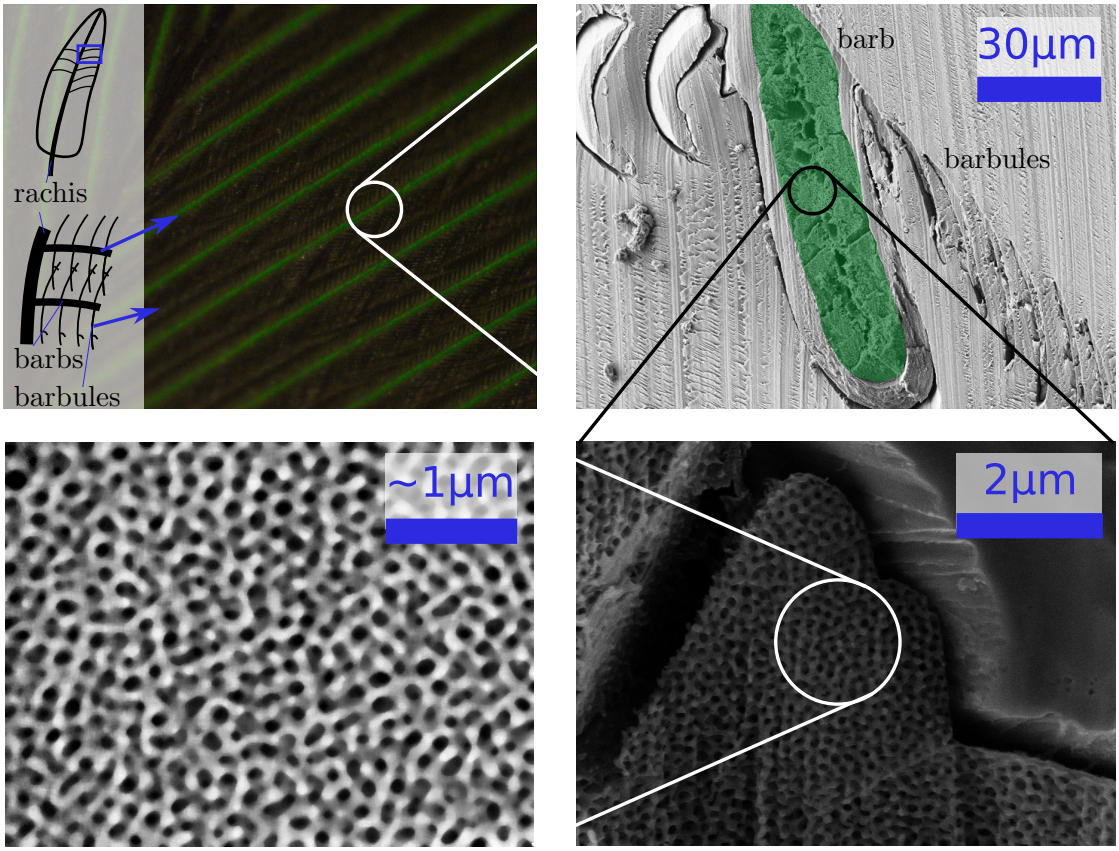

Figure 2.3.: Example of green feathers of *Agapornis roseicollis* and the feather anatomy. The top right image shows a SEM image with the feather embedded in epoxy resin. The largest magnification clearly shows the colour giving, sponge like network structure, whose Fourier transform is shown in Figure 2.4. Note that additionally to the structural colour, yellow pigments are present in the feather barbs and that it is their combination that gives *Agapornis roseicollis* their green appearance [36].

If the colour does stem from the structural distribution of the material, colour prediction should be possible from the microscope images. This is often done with reference to the work of Benedek in 1971 [13]. He describes why the cornea of the human eye, which consists of collagen fibres, is transparent even though a single fibre would only allow it to be opaque. Benedek concludes it is due to the spatial arrangement of the fibres that allows for constructive interference, making the cornea transparent. If the collagen fibres are driven apart by watery voids, e.g. due to the disease *cataract*, the cornea becomes opaque as the interference conditions are not met anymore. He deduces

$$\lambda_{\text{peak}} = n_{\text{avg}} \frac{4\pi}{|\boldsymbol{k}_{\text{peak}}|} \tag{2.1}$$

for the peak reflected wavelength by calculating the incident plane waves interference with the scattered field. This leads to the famous Bragg equation and, for backscattering, the above formula 2.1 is the received. Thereby point scatterers were assumed and $|\boldsymbol{k}_{\text{peak}}|$ is the magnitude of the peak position in reciprocal space, marked as the blue arrow in Figure 2.4. n_{avg} is the average or effective refractive index of the structure as defined in the next chapter, Equation 3.1.

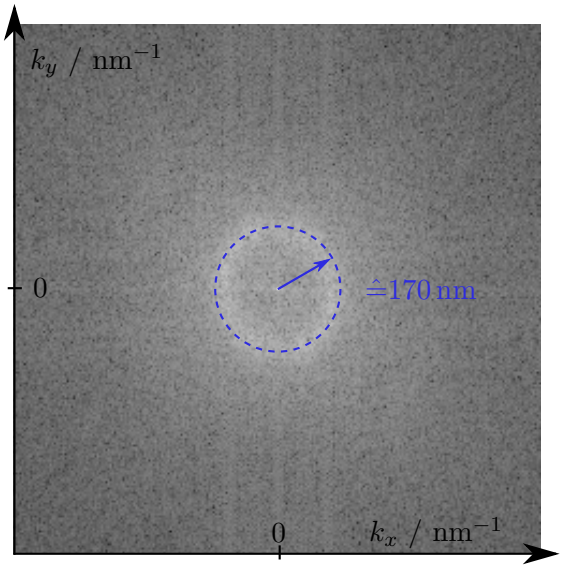

Figure 2.4.: Fourier transform of Figure 2.3, bottom left. A ring indicating isotropy and a characteristic length is clearly visible. The 170 nm characteristic length together with the mean refractive index of $n_{\text{avg}} \approx 1.283$ gives a peak reflectance at $\lambda_{\text{peak}} = 436\,\text{nm}$, or blue colour. The calculation details are given in the text.

Since Benedeks work a lot of research was done, which will reviewed below. Most importantly, the connection between electronic semiconductors to photonic structures could be established, leading to further, more sophisticated theories. Such biological structural colours from amorphous sponge like β-keratin structures are a proof that it is possible to create at least a stop band with materials of low refractive index. The next step is to reproduce these structural colours. Many applications are imaginable, examples are given in the introduction. It is worthwhile to know how the structures are formed in nature, where self assembly methods are widely spread. These methods are very elegant, as they originate from the fundamental physics of the interaction of the materials. However, the results are hard to predict and difficult to mimic in experiments. In [27] it is argued that phase separation by spinoidal decomposition takes place when the birds feather barbs are formed. This complex process is briefly described in section 4.2. To start with, natural structures can be used as a template, as e.g. done in [40] who used the original structure only as a template. They infiltrated the spongy structure, so that after calcination of the keratin an inverse structure made up out of silicon in air respectively titan dioxide in air was left. They utilised a sol-gel process,

described in section 5.3. There it is also discussed how the pattern could be extracted, to further analyse its properties. Again, many articles exist on the matter of biomimetics of structural colour, and it is referred to [41] for a general overview. As this work aims to understand photonic structures, well defined structures are in need to study the influence of the exact position of each node and the characteristics of the point pattern. Thus, self assembly methods are little of use and alternatively, three dimensional printing systems are used, described in chapter 4.

2.2. Fundamentals

In the following, the theory of band gaps and their formation is discussed, with emphasis on photonic band gaps. Originating from the band structure model for electrons in solid state physics, the theories of band gaps can be generalised to any quantity which can be expressed as waves, interacting with spatially distributed potentials. The goal here is to create a distribution of potential so that a band gap occurs. This inverse problem is difficult to solve, contrary to determining the band gap from a given structure.

Band gap structures can generally be divided into two subclasses, just as the structural colours described above. The one class are those structures with a strict periodic potential distribution, to which crystals count. Those produce iridescent colours. The second class is characterised by a non-periodic potential distribution. Examples are quasi-crystalline distributions but also amorphous ones. Both may form a band gap, to which quasi crystals can be counted and that produce non-iridescent colours. The exact origin of band gaps in the later class is still veiled, but intensively studied.

As being so promising for future design of optical devices, a vast amount of literature on photonic materials exists and is growing continuously. On the formation of photonic band gaps in periodic structures, e.g. *Molding the Flow of Light* by Joannopoulos *et. al.* [42] as a textbook to which can be referred to; or Yablonovitch [43] as an early review of photonic crystals. The model for the formation of a gap in amorphous structures is theoretically more challenging. Recent reviews are [16, 44, 45]. Saito [41] provides an approach inspired by biomimetics. General wave propagation in random media was already discussed in 1991 by Ishimaru [14]. The following sections represents a mélange of this literature with the goal to provide the fundamental models of photonic band gap formation and preparation for experiments to study those meta-materials.

Dealing with electromagnetic waves, Maxwell's equations are in need:

$$\nabla \cdot \boldsymbol{D} = \rho \qquad \text{Gauss's law} \tag{2.2}$$

$$\nabla \cdot \boldsymbol{B} = 0 \qquad \text{Gauss's law for magnetism} \tag{2.3}$$

$$\nabla \times \boldsymbol{E} = -\frac{\partial}{\partial t}\boldsymbol{B} \qquad \text{Faraday's law of induction} \tag{2.4}$$

$$\nabla \times \boldsymbol{H} = \boldsymbol{j} + \frac{\partial}{\partial t}\boldsymbol{D} \qquad \text{Ampère's circuital law with Maxwell's extension} \tag{2.5}$$

whereby $\boldsymbol{E}$ is the electric field, $\boldsymbol{D}$ the electric displacement field, $\boldsymbol{H}$ the magnetic field and $\boldsymbol{B}$ the magnetic induction field, ρ is the free charge density and $\boldsymbol{j}$ the electric current

density. Non-linear effects of the electric field in the given material are neglected and a refractive index constant with respect to the wavelength $n(\boldsymbol{r}) = \sqrt{\epsilon(\boldsymbol{r})}$ is assumed, with the relative permittivity (formerly called *dielectric constant*) $\epsilon(\boldsymbol{r})$. The discussion is restricted to bi-phase dielectric materials, for example a polymer structure with refractive index $n_\mathrm{d} = \sqrt{\epsilon_\mathrm{d}} > 1$ distributed in air $n_\mathrm{a} = \sqrt{\epsilon_\mathrm{a}} \approx 1$. Note that any loss, for example through absorption, can be modelled by an imaginary part in the refractive index. This, however, is omitted in this thesis and only lossless materials with real refractive index $n \in \mathbb{R}$ are assumed. Furthermore, no external charges or currents are assumed, thus $\rho = 0$ and $\boldsymbol{j} = \boldsymbol{0}$. The constitutive equations then simplify to $\boldsymbol{D} = \epsilon(\boldsymbol{r})\epsilon_0\boldsymbol{E}$ and $\boldsymbol{B} = \mu_0\boldsymbol{H}$, μ_0 being the vacuum permeability and ϵ_0 the vacuum permittivity. Furthermore, only the stationary solutions $\boldsymbol{E}(\boldsymbol{r}, t) = \boldsymbol{E}(\boldsymbol{r})\mathrm{e}^{-i\omega t}$ and $\boldsymbol{H}(\boldsymbol{r}, t) = \boldsymbol{H}(\boldsymbol{r})\mathrm{e}^{-i\omega t}$ are examined, so that $\frac{\partial}{\partial t} \to -i\omega$. This all leads to the four equations

$$\nabla \cdot (\epsilon(\boldsymbol{r})\boldsymbol{E}(\boldsymbol{r})) = 0 \tag{2.6}$$

$$\nabla \cdot \boldsymbol{H}(\boldsymbol{r}) = 0 \tag{2.7}$$

$$\nabla \times \boldsymbol{E}(\boldsymbol{r}) = -i\omega\mu_0\boldsymbol{H}(\boldsymbol{r}) \tag{2.8}$$

$$\nabla \times \boldsymbol{H}(\boldsymbol{r}) = i\omega\epsilon(\boldsymbol{r})\epsilon_0\boldsymbol{E}(\boldsymbol{r}) \tag{2.9}$$

from which Equation 2.9 can be substituted into Equation 2.8 to arrive at the *master equation* of electromagnetic waves propagating in a structured dielectric material:

$$\hat{A}\boldsymbol{H}(\boldsymbol{r}) = \nabla \times \left(\frac{1}{\epsilon(\boldsymbol{r})}\nabla \times \boldsymbol{H}(\boldsymbol{r})\right) = \left(\frac{\omega}{c}\right)^2 \boldsymbol{H}(\boldsymbol{r}), \tag{2.10}$$

where $\hat{A}$ is an operator containing the two curls and $c = 1/\sqrt{\mu_0\epsilon_0}$ is the speed of light in vacuum. This equation determines the eigenstates of the system. If $\boldsymbol{H}(\boldsymbol{r})$ is solved complying with Equation 2.7, $\boldsymbol{E}(\boldsymbol{r})$ can be calculated with Equation 2.6 and Equation 2.8. Equation 2.10 has the form of an eigenvalue equation and one approach to numerically solve it is introduced in section 3.4. The equation is similar to the Schrödinger equation for electrons in a bulk material. Therefore, basic concepts and theories of electronics can be adapted to photonics. Equation 2.10 could be generalised further for any quantity expressed as a wave.

Note that Maxwell's equations are scale invariant. This implies that if $\boldsymbol{H}(\boldsymbol{r})$ is a solution with eigenfrequency ω to Maxwell's equations for a given $\epsilon(\boldsymbol{r})$, $\boldsymbol{H}(s \cdot \boldsymbol{r})$ is a solution for the structure $\epsilon(s \cdot \boldsymbol{r})$, with scale parameter $s \in \mathbb{R}$ and eigenfrequency $s \cdot \omega$. Practically, this means if the dielectric structure described by $\epsilon(\boldsymbol{r})$ is scaled with factor s, the fields and their eigenvalues are simply scaled with the same factor s. A solution at one length scale determines the solutions at all other length scales. This has the important implication that if a structure with a band gap has been found, the gap can be shifted just by scaling the structure.

Still, different length regimes can be pointed out by comparing the wavelength λ to a characteristic length l_char. It is often useful to see a photonic structure as the accumulation of many scatterers. This allows for the separation of the structure into form- and structure factor in reciprocal space, as will be discussed later. Neglecting the

influence of the arrangement of the scatterers, those scatterers have a scattering cross section σ. It serves as an estimation for the ratio of incident light which is scattered. This effective area quantifies the likelihood of a scattering event and can also be given for the whole structure. The event can as well be dependant on the solid angle Ω in which is scattered. In this case a quantification with the differential cross section $\mathrm{d}\sigma/\mathrm{d}\Omega$ is useful.

If the spatial modulation of the structure, respectively the particle size, is on a smaller length scale than the wavelength λ, the scattering is called Rayleigh scattering. Any particle at this length scale can be approximated by a spherical shaped dielectric material of similar volume and diameter d, as long as an incident electric field is uniform within the particle. The interaction can then be described by the electromagnetic wave of wavelength λ inducing a dipole in the spherical particle, that in turn re-radiates an electromagnetic wave like a Hertzian dipole with the same wavelength. The typical $1/\lambda^4$ dependency of the relative scattered intensity arises

$$\frac{I}{I_0} = N \cdot \frac{2\pi^5 d^6}{3\lambda^4} \left(\frac{n^2 - 1}{n^2 + 2} \right)^2 . \tag{2.11}$$

Here, N denotes the scattering density in scatterers per volume and n the refractive index of the particle. The d^6 dependency arises from the polarizability of the particle, showing that its volume responds in a squared manner. An alternative and more detailed deduction of Equation 2.11 can be found in [46]. Rayleigh's scattering theory is usually applicable for $d < \lambda/10$ and the angle dependency explains for example the blueness and polarisation of the daylight sky.

For the intermediate regime, where $1\, l_{\mathrm{char}} \approx \lambda$, Mie theory applies. The scattering cross section can only be calculated analytically for perfect spheres. Peaks in the scattering cross section are called *Mie resonances*. It is this regime that is of interest here, as the typical length scale for photonic structures is a quarter of a wavelength. Calculations for the cross section have been done by [29]. The single particle scattering is hereby perturbed by nearby scatterers, dependant on the arrangement of the individual scatterers.

2.2.1. Dispersion Relation

With solving the master Equation 2.10, the dispersion relation $\omega(\boldsymbol{k})$ is obtained, relating energy and momentum of the wave. Here, the energy E is expressed with the frequency as the eigenvalue $\omega = E/\hbar$, $\hbar$ denoting the reduced Planck's constant, and the momentum $\boldsymbol{p}$ by the wave vector as eigenvectors $\boldsymbol{k} = \boldsymbol{p}/\hbar$. In the simplest case, for a homogeneous refractive index, there is a linear relation between frequency and wave vector magnitude

$$\omega(\boldsymbol{k}) = \frac{c}{n} \cdot |\boldsymbol{k}|. \tag{2.12}$$

By introducing a spatial structure to the refractive index, this relation can become arbitrarily complex. The dispersion relation depends on the direction of the wave vector $\boldsymbol{k}$, and for a given range of frequency it may happen that no solution exists for any $\boldsymbol{k}$. This

is called a *band gap*. The group velocity v of light is given by $\nabla_{\boldsymbol{k}}\omega(\boldsymbol{k})$. For the simplest case as in Equation 2.12 the velocity $v = c/n$ is independent of the direction. Various interesting effects can be obtained by tuning the dispersion relation or the structure of the refractive index material, respectively [44].

In the general case, the dispersion relation is a three dimensional scalar field, as it maps every vector $\boldsymbol{k}$ to one scalar number, or multiple numbers, as will be seen in subsection 2.5.1. This is quite difficult to depict on a two dimensional plane like on paper or on a monitor. Therefore, it is convenient to depict the areas of equal frequency ω in $\boldsymbol{k}$-space, the iso-frequency surfaces in 3D or iso-frequency lines in 2D. The so called *band structure* is also a way to depict the dispersion relation for periodic arrangements of refractive index in space, as discussed in subsection 2.3.2.

The direction of refraction is thus determined by the dispersion relation of the material. In its simplest form, when an electromagnetic wave couples into a homogeneous medium, this is described by Snell's law, as shown in a), Figure 2.5. For a structure with a more complicated dispersion relation, peculiar things like negative refraction can take place, see Figure 2.5, b). This would obey Snell's law for a *negative* refractive index. The component of the refracted waves velocity parallel to the surface is anti-parallel to the incident waves parallel velocity component. Note also that the direction of propagation is different to the wave vector, namely orthogonal on the iso-frequency surface of the dispersion relation. The construction of the refracted wave vector happens in the

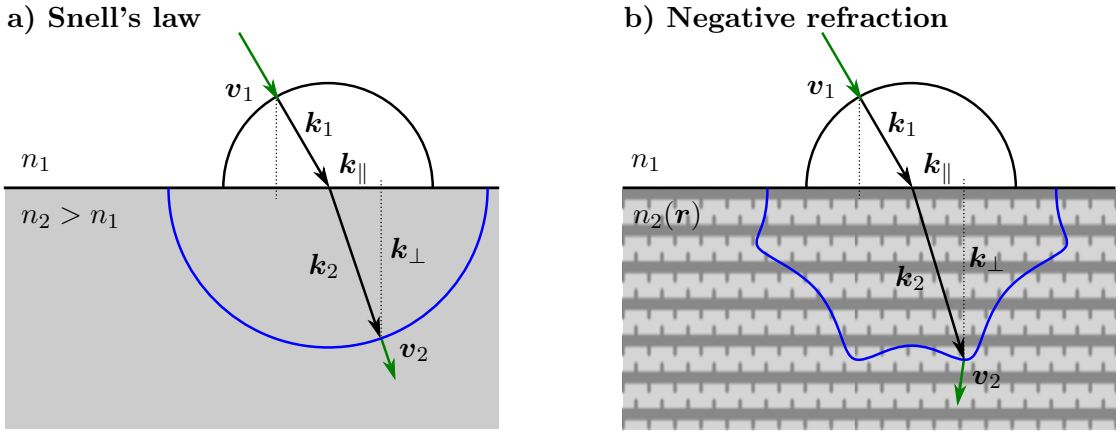

Figure 2.5.: On the coupling of light from a homogeneous material into a) homogeneous refractive index materials and b) heterogeneous refractive index materials. The black half-circle is the iso-frequency line of the dispersion relation in the homogeneous material with refractive index n_1. Sketched in blue is the iso-frequency line of the materials dispersion relation that is coupled into. The green arrow is the normal at the point, where the $\boldsymbol{k}$-vector in the medium hits the iso-frequency line. A similar process happens of course when light is decoupled from the material. Negative refraction can take place, as sketched in b) and studied in [47].

following way, for light of frequency ω coupling into a material with different refractive

index. Due to charge displacement, the component $\boldsymbol{k}_{\parallel}$ of the wave vector parallel to the surface of the material is conserved and only the component $\boldsymbol{k}_{\perp}$ perpendicular to the surface changes. Due to energy conservation[1], the refracted wave vector needs to comply the dispersion relation, in other words has to lie on a iso-frequency line respectively surface. With this, a unique construction is done. *Superprism effects* can be explained in the same manner, where small deviations in incident angle result in great changes of refracted angle. More complex processes like the self-collimation of light in photonic crystals [48] are also possible.

Density of States

An important quantity to actually define a band gap is the density of states (DOS), which can be derived from the dispersion relation. Analogue to the density of states in electronics or phononics [49], the DOS can be defined as the number of states in an infinitesimal frequency interval $(\omega, \omega + \mathrm{d}\omega)$

$$\mathrm{DOS}(\omega) = \frac{V}{(2\pi)^3} \int_{\omega=\mathrm{const}} \frac{\mathrm{d}S_k}{|\nabla_{\boldsymbol{k}} \omega(\boldsymbol{k})|} \tag{2.13}$$

with the (constant) volume of one state $V/(2\pi)^3$ in $\boldsymbol{k}$-space and an area element $\mathrm{d}S_k$ on the iso-frequency surface $\omega = const$. As above, $\nabla_{\boldsymbol{k}} \omega(\boldsymbol{k})$ is the group velocity of the wave in the material. In most cases, the quantitative DOS is of less interest than the order of magnitude, as a photonic band gap would be visible as a range with $\mathrm{DOS} = 0$. A band gap is then defined as this range, with the centre frequency ω_0, width $\Delta\omega$ and ratio $\Delta\omega/\omega_0$. The later number is used to quantify a band gap with a single number, as the centre frequency depends solely on the scaling of the structure. For an electromagnetic wave in a homogeneous medium, the DOS $\propto n/c \cdot \omega^2$, which can be seen for low frequencies respectively large wavelengths, where the wave behaves much like in a homogeneous medium. For an actual calculation, further discussion and implications of the dispersion relation, please refer to section 3.4.1 and section 6.2.

2.3. Structure Factor

The structure factor captures any structure of direct space by Fourier transforming it to reciprocal space. Within the Born approximation [50], it can be interpreted as how a material scatters light from incident planar radiation. This makes it a versatile tool to investigate patterns generated by scattering experiments. Thus, the structure factor from the Fourier transform of the refractive index distribution is quickly derived here.

In the Born approximation, weak interactions between the incident waves and scatterers is assumed. Therefrom it concludes that the scattered field is proportional to the scattering potential, and with that the scattered intensity can be written as

$$I(\boldsymbol{k}) \propto |n(\boldsymbol{k})|^2. \tag{2.14}$$

[1] Conservation of momentum is not given as homogeneity of space is broken by changing the material.

It could be realised by a weak potential, compared to the incident energy, and implies *single scattering*: The scattering potential is invisible to the once scattered wave which is also called *kinematic scattering*. Hereby, the potential which scatters an incoming planar wave is the refractive index, denoted by $n(\boldsymbol{r}) = \sqrt{\epsilon(\boldsymbol{r})}$. For electrons described by their probability density function the potential could be the electron charge distribution or for neutrons the mass distribution. By Fourier transforming this potential, it can be expressed with the spatial frequency $\boldsymbol{k}$ as $n(\boldsymbol{k})$. The scattering potential often consists of many scatterers $j = 1, ..., N$ at positions $\boldsymbol{R_j}$, each with a potential $f(\boldsymbol{r})$, also called form factor, so that

$$n(\boldsymbol{r}) = f(\boldsymbol{r}) * \sum_{j=1}^{N} \delta(\boldsymbol{r} - \boldsymbol{R_j}) \xrightarrow{\mathcal{F}} f(\boldsymbol{k}) \sum_{j=1}^{N} \mathrm{e}^{-i\boldsymbol{k}\boldsymbol{R_j}} = n(\boldsymbol{k}). \tag{2.15}$$

Here, the convolution theorem of the Fourier transform and the definition of the Dirac delta distribution δ in k-space it is used. By inserting $n(\boldsymbol{k})$ in the Born approximation Equation 2.14, the structure factor is derived:

$$\begin{aligned} I(\boldsymbol{k}) \propto |n(\boldsymbol{k})|^2 &= |f(\boldsymbol{k})|^2 \cdot \left(\sum_{i=1}^{N} \mathrm{e}^{-i\boldsymbol{k}\boldsymbol{R_i}} \right) \cdot \left(\sum_{j=1}^{N} \mathrm{e}^{i\boldsymbol{k}\boldsymbol{R_j}} \right) \\ &= N \cdot |f(\boldsymbol{k})|^2 \cdot \underbrace{\frac{1}{N} \sum_{i,j}^{N} \mathrm{e}^{-i\boldsymbol{k}(\boldsymbol{R_i} - \boldsymbol{R_j})}}_{:= S(\boldsymbol{k})}. \end{aligned} \tag{2.16}$$

To give an intuition of the structure factor, for a wave of wave vector $\boldsymbol{k}$ and spatial frequency $k = |\boldsymbol{k}|$, the phase difference between the scatterers centres is collected and normalised by their number. In general, the structure factor depends on the direction of $\boldsymbol{k}$. This is of importance for periodic potentials where the spatial distribution of potential strongly depends on the direction. In Figure 2.6 a) and b), two 2D-patterns and their structure factor $S(\boldsymbol{k})$ are shown schematically. However, for isotropically distributed scatterers, as shown in Figure 2.6 b), the dependency on direction averages out and only the magnitude k of the frequency is of interest. Calculations of the structure factor $S(k)$ for three totally different types of point patterns can also be seen in section 3.2, Figure 3.4. The structure factor peaks if an inverse characteristic length of the spatial distribution is hit by the spatial frequency k. For periodic patterns this is e.g. the distance between lattice planes formed by the scatterers. As shown in Figure 2.6, the first peak of the structure factor appears at $\boldsymbol{k_1}$ and corresponds to the average distance to the nearest neighbours. The second and third peaks at the vectors $\boldsymbol{k_2}$ and $\boldsymbol{k_3}$ correspond implicitly to the next and second next nearest neighbours, in the sense that small lattice plane distances in Figure 2.6 b) can only be constructed if the regions up to the second and third shells are sufficiently correlated.

As k scales inversely to the length scale of the spatial distribution of the scatterers, a low k describes large length scales. Any order in the long range regime leads to similar

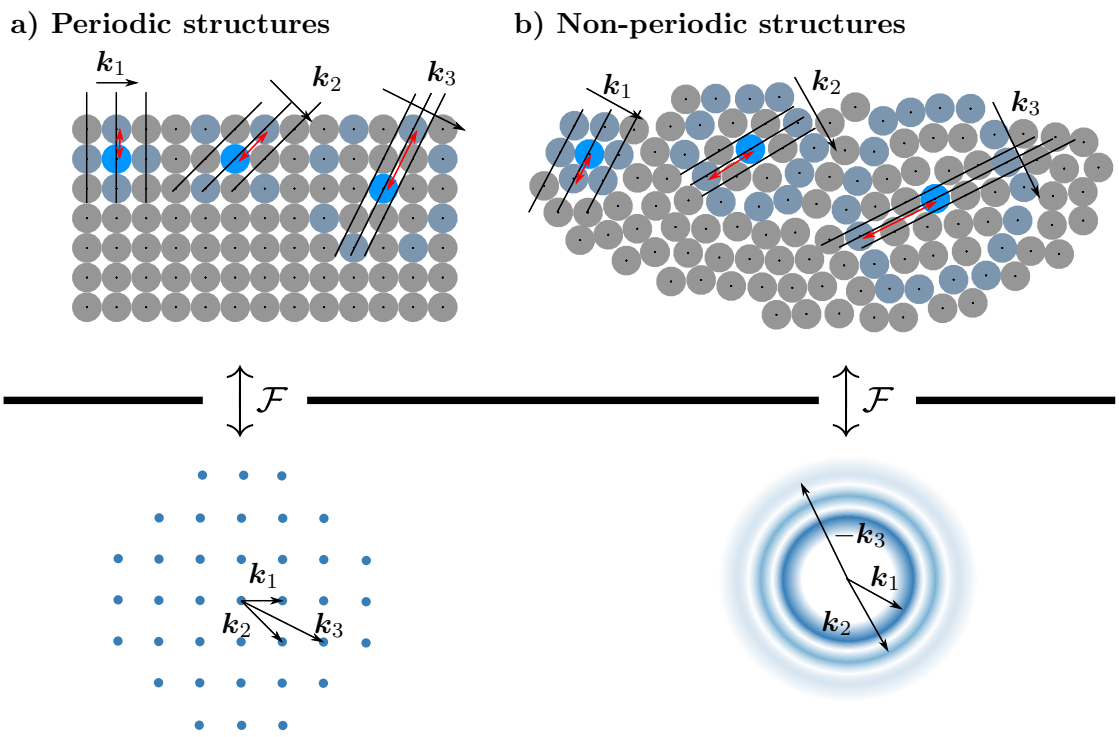

Figure 2.6.: Sketch on the formation of peaks in reciprocal space due to characteristic distances in direct space. In direct space, the black dots are scattering centres, the circles around them a potential. Marked blue are scatterers surrounded by their light blue neighbours. a) shows a 2D periodic square lattice and b) a 2D semi-random pattern. The black lines show places of equal phase for the corresponding wave vectors $\boldsymbol{k}_i$, the red double-arrows show the according scatterer distance on the lines, being the distance to the neighbouring shell. In b) can be seen that the centres of the scatterers do not exactly lie on the places of equal phase contrary to a), resulting in lower peaks.

phases and contributes to the structure factor. For example, if there is a clustering of particles on large length scales, a peak in the low k regime represents these clusters. However, if the particle density is homogeneous one obtains $S(k) \to 0$ for $k \to 0$.

The first peak in $S(k)$ corresponds to the largest characteristic length. This can be the first shell around each particle, if no long ranged clustering is present. This case is shown in Figure 2.6, denoted by $\boldsymbol{k_1}$. For slightly larger k, no characteristic length is present, the scattering reaches a minimum until the next shell contributes its phases for $\boldsymbol{k_2}$. This continues for larger k until the shells are too smeared out. $S(k)$ converges to the average number density of the pattern. For a periodic lattice, $S(k)$ smears out[2], however, $S(\boldsymbol{k})$ does not and there will be scattering only for discrete $\boldsymbol{k}$ which peak in $S(\boldsymbol{k})$. For Poisson

[2]Mathematically, the peaks of $S(k)$ become denser and denser and its practical to speak of the local average peak density that converges to the average number density. Experimentally, no such thing as a discrete peak exists, thus $S(k)$ smears out, converging to the same number.

patterns consistent of points with random and independent coordinates, no characteristic length is present at all. No phases can accumulate and the structure factor is a constant with the magnitude of the average number density.

These properties make the structure factor a valuable tool to discriminate all sorts of patterns, including random patterns, which are otherwise hard to tell apart. Figure 2.7 gives a classification for structures based on the properties of the structure factor $S(k)$ of patterns that are interesting for this work, based on the suggestions of Batten *et. al.*[51].

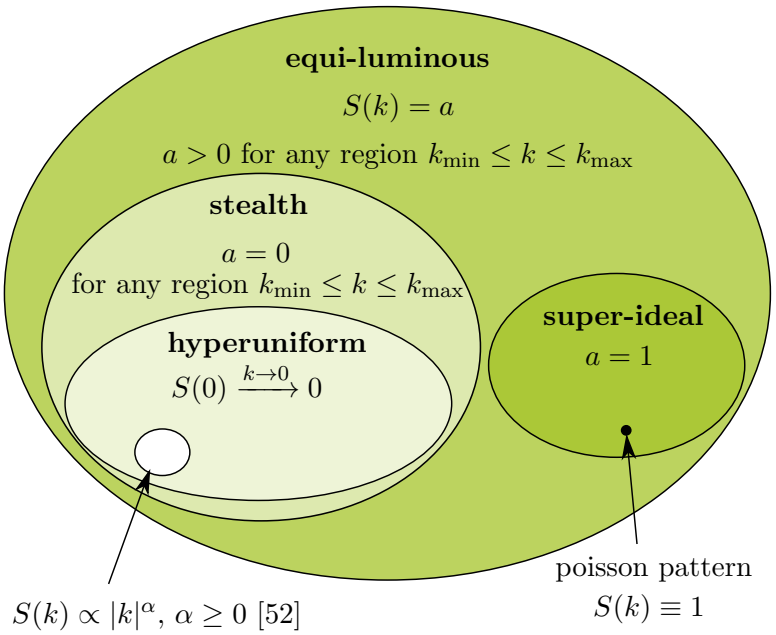

Figure 2.7.: Classification of different point patterns using properties of the structure factor $S(k)$. The subclass of hyperuniform patterns where $S(k) \sim |k|^{\alpha}$ is particularly interesting with $\alpha = 1$ for the Harrison-Zeldovitch model of the early universe, superfluid ^{4}He and jammed amorphous sphere packings [52]. The latter is most interesting in the field of amorphous photonic structures. Note that isotropy is not a criterion for a pattern to be in one of these classes, as all periodic patterns are hyperuniform [17].

The question arises how arrangements of the positions of scatterers can be found by fullfilling the desired characteristics. Deducing $S(k)$ from a given point pattern is straight forward. The inverse problem, to generate a pattern with a specific structure factor is non-trivial, as multiple solutions are conceivable and information needs to be generated (the exact position of each scatterer). Hyperuniform patterns are interesting in particular for this work, as [53] suggests that hyperuniformity is a criterion for a band gap to form, together with uniform local topology and short range geometric order. Recent studies strongly support this claim [54]. Also interesting is the fact that [55] found $S(k) \propto |k|^1$ for small k in jammed disordered hard-sphere packings. This could provide a possible "algorithm" to generate hyperuniform patterns, as done in [56]. Generating such patterns is a surprisingly large field of research as they can be used versatilely and

found in various places, from the distribution of photo-receptors in chickens eyes [57] and related on the question in which pattern images can be sampled [58], over hard sphere packings [55] to suprafluidic helium [52] and even theories of the early universe, namely the Harrison-Zeldovich model [52]. To artificially construct and examine such a pattern is thus of large interest. Very often the final static point pattern is defined as a minimal energy state of a potential. The desired properties of the pattern are put in the potential or energy landscape which is then minimised for some starting pattern. In [52], a collective coordinate approach is presented that makes it possible to generate patterns with desired structure factor.

Keep in mind that the Born approximation was assumed, that allows to interpret the structure factor as the outcome of a scattering experiment. According to Brüser *et. al.* [59], this is applicable for a maximal refractive index contrast of $\Delta n \approx 0.15$. The structure attempted to be fabricated here with $\Delta n > 0.5$ excesses this limit, and the kinematic scattering approach is not useful to interpret interference patterns. The resulting implications are further discussed in section 5.1.

2.3.1. Hyperuniformity

Another way to characterise point patterns is their *hyperuniformity*. Its determination is relatively easy to implement and statistically less critical. Hyperuniformity was first defined 2003 by Torquato *et. al.* [17] as follows: A point pattern in dimension d is hyperuniform, if the number variance in a d-dimensional volume within a point pattern grows as the $d-1$-dimensional surface area of this volume. The volume hereby has to be strictly convex and large compared to the characteristic length of the point pattern. In other terms, a pattern is hyperuniform, if it holds

$$\sigma(r) = \left\langle \left(N(r) - \langle N(r)\rangle\right)^2 \right\rangle = Ar^{(d-1)} \propto r^{(d-1)} \tag{2.17}$$

with the number $N(r)$ of points inside a d-dimensional sphere of radius r and its according expectancy $\langle N(r)\rangle$. The prefactor A can then be used to rank patterns and serves as an order metric for seemingly random point patterns. All periodic patterns are hyperuniform [17]. In the same work, it was shown that hyperuniformity implies $S(k) \xrightarrow{k\to 0} 0$, therefore excluding long range number density fluctuations. The concept of hyperuniformity has also been extended to heterogeneous two phase random media, where infinite-wavelength volume fraction fluctuations vanish [60] contrary to infinite-wavelength volume density fluctuations in random point patterns.

2.3.2. Brillouin Zone

The *Brillouin zone* (BZ) can be constructed for periodic structures by taking the bisecting planes between neighbouring reciprocal lattice points. Those planes are also called Bragg planes. According to the Bloch theorem, it is sufficient to solve the master Equation 2.10 for $\boldsymbol{k}$-vectors in the BZ. This results in multiple solutions for one wave vector $\omega_i(\boldsymbol{k})$, $i \in \mathbb{N}$ and ultimately in the band structure. Due to translational invariance, one

can imagine the dispersion relation origins in every reciprocal lattice point. For large enough $\boldsymbol{k}$ the solution thus appears in the neighbouring BZ. For homogeneous potentials, the dispersion relation has spherical shape. Thus the neighbouring spherical dispersion relation reaches into the BZ, creating what is sometimes referred to as "pockets". As stated above, the 3D dispersion relation is often depicted in a 1D plot, called the band structure, and this is how those bands arise: they are dispersion relations from neighbouring reciprocal lattice points. It is then sufficient to calculate the dispersion relation along high symmetry lines in the BZ, and the rest is obtained by symmetry operations. In literature, it is often stated that the dispersion relation is folded into the BZ, but to be pedantic it is more a translation or shifting instead of a folding process.

The convenient concept of the Brillouin zone is unfortunately not directly transferable to non-periodic structures. By applying the same construction and taking the bisecting planes between origin and first peaks of reciprocal space as boundaries, one would obtain a spherical BZ. However, the whole reciprocal space cannot be tiled with a spherical BZ and a band structure cannot be obtained. Nevertheless, a dispersion relation exists and it should be spherical in amorphous structures, due to their isotropy. As defined in Batten *et. al.* [51], the *stealthiness parameter* χ represents the fraction of constraint degrees of freedom to the total number of degrees of freedom of a point pattern. In Florescu *et. al.* [53] it is stated, that this order parameter χ gives the fraction of wave vectors $\boldsymbol{k}$ in the Brillouin zone, for which the structure factor $S(k)$ vanishes. This is equivalent to a cut off wave vector magnitude $|\boldsymbol{k}_C|$. The range $|\boldsymbol{k}| = [0, |\boldsymbol{k}_C|]$ can be seen as the range of "forbidden" scattering. If the order parameter χ exceeds a critical value of $\chi_C \approx 0.77$, long range translational order develops for 2D patterns [51]. Florescu *et. al.* [53] found a band gap to open below χ_C, again for the 2D case. The gaps is closing again for values lower than $\chi = 0.35$, as short range order is excluded then. They also found that the critical wavelength $2\pi/|\boldsymbol{k}_C|$ is directly related to the midgap frequency, and the band width is inversely proportional to the magnitude of the density fluctuations on length scales greater than this critical wavelength, for large enough χ. Similar behaviour can be expected for the 3D case.

2.4. Scattering

Before the actual band gap formation is discussed, single scattering experiments are explained. This is done in order to examine a sample that possibly exhibits photonic band gap properties. The characteristics of the sample need to be investigated, preferentially without destroying the sample, which makes scattering experiments ideal. Again, imagine a point pattern, neglecting the form factor and assume a planar wave with wave vector $\boldsymbol{k}_{\text{in}}$ incident on the sample.

Considering scattering experiments in crystallography, the scattering cross section is small despite a scatterer number density of $\sim 10^{22}\,\text{cm}^{-3}$, due to a low scattering potential. The kinematic scattering approach is well suitable. The aim of this thesis is to investigate structures with a band gap at the near infrared. Multiple scattering is required for the gap to form. The length scales are much larger than in crystallography, leading to lower

scatterer densities. With a scatterer number density of only $\sim 10^{15}\,\mathrm{cm}^{-3}$ for a band gap at a wavelength of $\lambda = 1550\,\mathrm{nm}$, the scattering potential ergo refractive index contrast needs to be accordingly large. To describe scattering experiments at those structures with the kinematic scattering approach it is thus necessary to reduce this high contrast, for example by infiltrating liquids with comparable refractive index into the structure.

The direction into an incoming wave is scattered can be determined by the Ewald construction. This is equivalent to the Bragg scattering mechanism, where planes occupied by the scatterers can be imagined in the structure of interest at which the incoming wave is partially reflected and interferes. Note that the Born approximation is not assumed and this scattering can happen many times, destroying the ordered pattern expected by the Fourier image. Only if single scattering is present for a low refractive index contrast, the once scattered direction can be kept until the wave decouples from the sample and the direction will be detectable on a screen. However, if scattered at a lattice multiple times below a certain limit, a pattern will still be visible. Again, elastic scattering is assumed where no energy transfer takes place between the wave and the scatterer. The scattered wave vector can thus point in all directions, forming a spherical shell.

The concept of reciprocal space marks the wave vectors at which scattering takes place. With the Ewald construction, as depicted in Figure 2.8, one can visualise that scattering takes place when the scattering vector $\boldsymbol{q} = \boldsymbol{k}_{\mathrm{out}} - \boldsymbol{k}_{\mathrm{in}}$ equals a reciprocal lattice vector $\boldsymbol{G}$. For the case of an amorphous material peaks at this scattering vector $\boldsymbol{q}$ need to be present. The condition that the scattering vector needs to equal a reciprocal lattice vector is also known as the *Laue condition*. Contrary to the formation of a band gap, light of a sufficient coherence length is needed, with coherence length around the specimen size. This is because usually the scattering potential is so small, that only a small fraction of the incident intensity is scattered and many events have to add up to reach sufficient intensity to be detected. By increasing the potential, more scattering events happen, until the incident light completely "forgot" the original direction and a speckle pattern is detected. In principle, the form factor has to be multiplied onto the diffraction pattern if extended scatterers are investigated. It was observed that this pattern is destroyed by even a little amount of multiple scattering.

2.5. Band Gap Formation

The mechanism of band gap formation for amorphous structures is not finally settled yet [44]. Most recent studies emphasise the role of short range order and hyperuniformity of the pattern [54]. In solid state theory for electrons, two complementary descriptions exist on the formation of band gaps, and the analogy to photons can be drawn. Both descriptions begin with opposing extreme assumption. Meeting in the middle, only both theories together can explain the formation of band gaps in amorphous structures [61, 62]. The formation of a band gap in periodic structures can be attributed to Bragg scattering at crystal planes and described with the adapted *nearly free electron* model. Single scatterer resonances are present as well and may widen a band gap. Due to the lack of long range order, the Bragg mechanism can not be as pronounced in amorphous

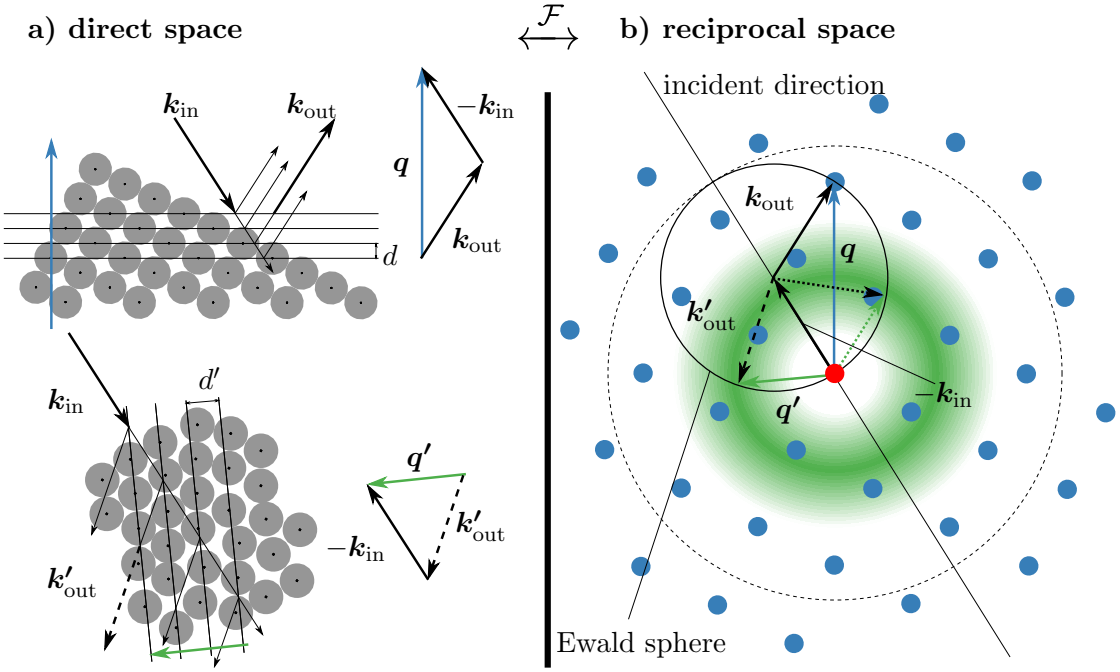

Figure 2.8.: Sketch of a) Bragg scattering and the analogue b) Ewald-construction in order to explain diffraction peaks. All points in the dashed circle can cause scattering if the scatterers are rotated collectively. It becomes clear, that if the magnitude of $\boldsymbol{k}_{\text{in}}$ becomes small (the associated wavelength long), the Ewald circle becomes small, and eventually no scattering can take place. Shown blue: crystalline specimen, green: semi-random specimen with characteristic length (inverse green circle radius). The blue/green arrow shows momentum that is gained by the incident wave.

structures. Here, the single scatterer resonances are of greater importance, possibly supported by a little amount of Bragg scattering in the close surrounding of a scatterer. By assuming this, the problem can then be formulated similar to the *tight-binding* theory of electronics. In the following, both theories are explained briefly, adapted from Edagawa [44] and the references therein.

2.5.1. Nearly Free Photon Theory

When adapted to the present case, the nearly free electron theory translates to the *nearly free photon theory*. It starts with a free photon. Then, the eigenstates are plane waves. With introducing a weak refractive index contrast, those waves scatter at lattice planes and interfere to form standing waves at the Bragg planes. This can be best imagined at a one dimensional photonic crystal, a distributed Bragg reflector (DBR) as depicted in Figure 2.9. It consists of equidistant layers of two alternating materials with different refractive index. If the wavelength reaches twice the periodicity of the DBR, a standing wave forms. This results in a vanishing group velocity and propagation is not possible

anymore. If the energy of the photons is increased further, propagation is allowed again. The standing waves antinodes are located in the regions of higher refractive index, those for the higher energies in the region of lower refractive index. Therefore, the dispersion relation below the band gap is called *dielectric band*, and the region above *air band*. The energy difference between both standing waves determines the band gap width. This Bragg scattering mechanism is believed to be the origin of a photonic band gap in a photonic crystal.

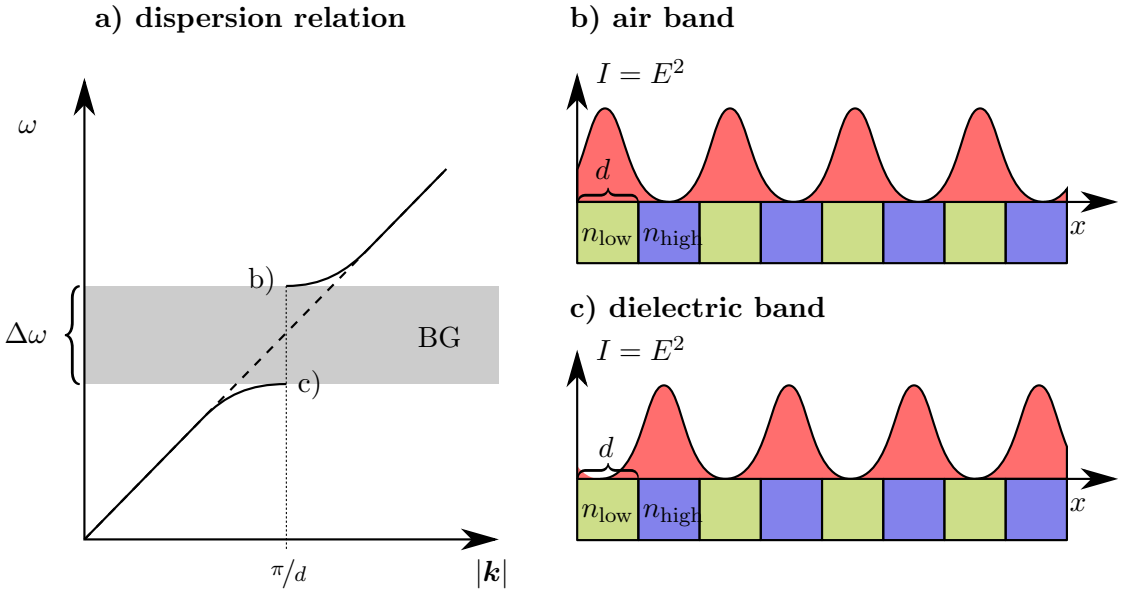

Figure 2.9.: Band gap formation for a 1D periodic structure at the example of a distributed Bragg reflector (DBR). Here, $n_{\text{low}} < n_{\text{high}}$ and both layers are of equal width d. In a) shown in grey is the photonic band gap (BG), which opens up as the two standing waves, whose intensity is shown in b) and c), having different energy. The energy difference occurs due to the different electric field distribution. The dispersion relation for a homogeneous medium with $n_{\text{eff}} = 0.5 \cdot n_{\text{low}} + 0.5 \cdot n_{\text{high}}$ is shown as the dashed line in a).

Note that the shape of a single scatterer plays a minor role as long as enough scatterers are on crystal planes, similar as depicted in Figure 2.8, a) and Figure 2.6, a). This allows for strong Bragg scattering. Due to a large refractive index contrast, multiple Bragg scattering occurs, disallowing the propagation of a wave of certain wavelength in a certain direction. A band gap created by such a mechanism is thus strongly anisotropic.

2.5.2. Tight-Binding Model

The tight-binding model is not transferable to the photonic case as easily as the nearly free electron model. It starts from the opposite assumption: electrons that are tightly bound to a potential, e.g. by an atom. There, they form localised states with the

energy of the state characteristic for the atom or potential, respectively. If the atoms are separated enough, like in a gaseous phase, the localised states will not couple and the localised bases become the eigenstates. The flow of electronic current is strongly suppressed, as it is only possible if electrons of the system tunnel from one atom to another, which is unlikely for the separated atoms. The total wave function of the system can be described by the sum of those separated localised states. The distance of the atoms can be decreased, for example by reducing the temperature or applying pressure. Then a liquid and eventually a solid phase is formed as the coupling between the localised states becomes stronger. Due to the overlap of the potentials, however, a dispersion relation is formed, making the energy of the electrons dependant their momentum. This is why the original energy levels smear out to form an energy band. With the decreased distance, tunneling is more likely and current flow is made possible. This process is illustrated in Figure 2.10 a) and b), adapted from [44]. A further introduction to the basics of the tight binding model which includes the calculation of the dispersion relation of electronic systems can be found e.g. in [63].

In this theory, the arrangement of the scatterers is not necessarily periodic, as long as the distance respectively coupling of the localised states is appropriate. Applied to optics and as already suggested in the initial paper of John [8], the regime where a band gap can be expected is right in the Mie regime and "connects" Rayleigh and geometric optics. Thus, Mie resonances possibly play the role of the localised states [61]. In [64] it is even suggested that the specific arrangement of the scatterers is irrelevant for the formation of a band gap, as long as the scatterers do not overlap and disturb the Mie resonances.

Florescu *et. al.* [53] argue that an isotropic band gap is formed, when short range order is present and long range is suppressed. Both kinds of order can not be varied completely independently, as strong long range order implies short range order. This would explain why crystals favour a band gap formation: order is present on every scale, allowing for multiple Bragg scattering and localised states to form a band gap. This interweaving of both mechanisms was also suggested in [65] for the three dimensional case. In terms of the order parameter χ introduced by Florescu *et. al.* [53], two critical values exist. A lower critical value $\chi_{\mathrm{C,\,l}}$ exists below which short range order is not present. Then uniform topology is not present and thereby the localised Mie resonances for a band gap to form are destroyed. An upper critical value $\chi_{\mathrm{C,\,u}}$ exists for which the pattern is long range ordered, destroying the isotropy of the band gap. It is argued, in order to get Mie resonances, a high enough refractive index contrast must be present and local uniform topology must be ensured. This implies a small variance in local characteristic lengths or angles.

2.6. Decoration

Due to the findings in the discussion above, the question on how to choose the form factor, e.g. how to decorate a given point pattern is quite non-trivial. Note that a heterogeneous two phase binary refractive index structure is intended to be fabricated

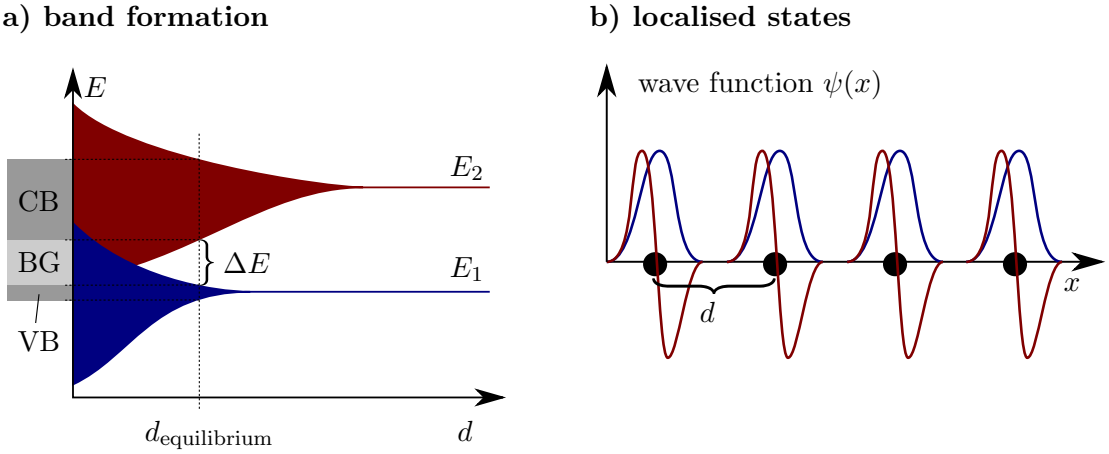

Figure 2.10.: Illustration of the tight-binding model to describe electronic states in solid materials. No periodicity is assumed. a) shows the formation of valence band (VB, analogue to the dielectric band) and conducting band (CB, analogue to the air band) for increased coupling strength by reducing the inter-atomic distance d. If both bands are energetically separated, a band gap (BG) occurs. b) shows two possible localised state wave functions $\psi(x)$ with different energies E_1 (blue) and E_2 (red) in one dimension. They can be provided by the atoms electron distribution, for example.

here, possessing an isotropic band gap, thus being amorphous. A general parameter for a decoration is the *filling fraction*, the ratio of high refractive index material in a representative volume. It determines the distance between interfaces of the two materials and thus governs the coupling of localised states as well as the distances at which Bragg scattering can take place. The calculation of the filling fraction for an arbitrary structure is not always trivial and is discussed in section 3.3. Following [65], localised states need to exist ideally at a similar frequency at which Bragg scattering takes place. This way, if a lack of lattice periodicity suppresses multiple Bragg scattering, localised states could compensate and develop a band gap. Starting with material selection, compromises need to be done. A minimal refractive index contrast is advantageous from a material selection point of view, contrary to the need of a high contrast in order to ensure Mie resonances.

The decorations can be classified in two different topologies. For the *cermet topology*, the structure consists of individual high refractive index inclusions in a low refractive index background. Those inclusions can be though of as individual scatterers. Studies, e.g. [66], found that scalar waves such as sound waves favour a cermet topology. Bi-continuous, tetrahedral *network topologies* are favoured by electromagnetic waves [67, 68], similar to a strongly distorted diamond network. A structure derived from a diamond, dubbed “photonic amorphous diamond” (PAD) has been found to posses a full 3D band gap [19, 20], in simulation as well as in experiments with microwaves. Additionally, it has been found that fourfold connections are advantageous for the band

gap. Interestingly, the electric field distribution in the dielectric and the air band is as expected from the nearly free photon model, despite the lack of periodicity. The network topology, however, contradicts the Mie mechanism, which requires isolated scatterers in order for strong resonances to form. It seems, this is the point where both theories meet. Considering the favoured tetrahedral bonds, analogy to electronics can be drawn, where band gaps for amorphous solids such as silicon (Si) or germanium (Ge) with these bonds is can be well described with the tight-binding method [15, 69].

Searching a photonic band gap material, the periodic woodpile structure was found by two groups simultaneously [70, 71]. It has the big advantage that it can be readily fabricated by means of regular 2D photo-lithography [72]. It consists of layers of gratings that are shifted half a period length, rotated and stacked on top of each other, as depicted in Figure 2.11. The woodpile structure derives from the diamond structure, as the contact points of the rods are distributed as a diamond pattern, if the rod spacing g and layer distance $c/4$ are chosen to be $c = \sqrt{2} \cdot g$. Then the direct crystal structure of the contact points is face centred cubic (fcc) and the reciprocal crystal structure is body centred cubic (bcc). For the general case, i.e. arbitrary ratios of g and c, the direct crystal structure is face centred tetragonal (fct). The exact shape of the rods has been found to be of minor importance, as long as the filling fraction is appropriate.

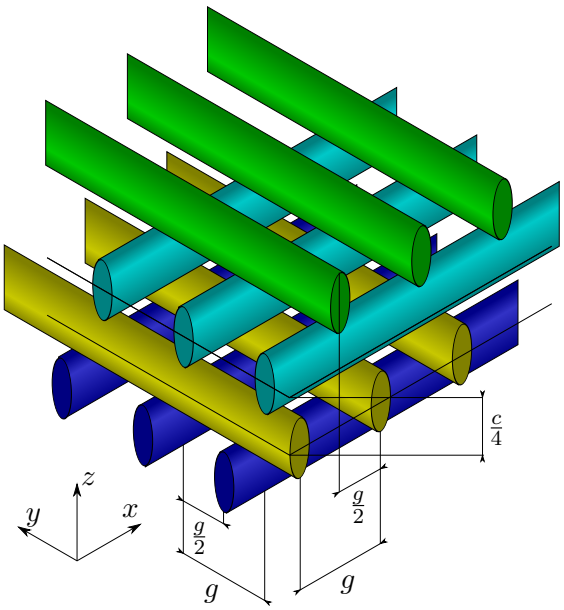

Figure 2.11.: Sketch of the woodpile structure, with elliptical decoration as explained in the text. It consists of layered gratings where every second layer is shifted perpendicular to the rods by half a rod spacing and every next layer is rotated by 90°. If the distance between four layers $c = \sqrt{2} \cdot g$, the points of contact of the rods are diamond distributed. It has been found that the cross section of the rods is of minor importance for the band gap formation.

A network topology, as found in the birds feather barbs, see Figure 2.3, can be created

straight forwardly by linking points with rods. This works whether the point pattern is amorphous or crystalline. The question is which points are to be linked. Suggested by the protocol by Florescu *et. al.* [53], the neighbours can be taken, defined by a Voronoi construction. The cross section of the rods and the number of neighbours define the form factor, the spatial extent of the rods the filling fraction. If the cross section of the rods is a circle it is referred to as a *cylindrical decoration*, if it is an ellipse it is called *elliptical decoration*. Those structures are well possible to fabricate with 3D printers. This distinction is used, since it is intended to use the direct laser writing (DLW) technique to fabricate samples. This method has the inherent property that a fabricated line has an elliptical cross section, in the present case with an aspect ratio of about $1:3$, elongated along the optical axis z. This is why only an elliptical decoration can be fabricated with this technique. Furthermore, the cross section of a rod depends on the angle of the rod with respect to the optical axis. This makes every cross section of the rods unique and the structure quite complicated. Similar to the woodpile structure, however, it is expected not to be critical for the band gap formation. As discussed in section 4.2, these kind of network topologies are self assembled with the spinoidal decomposition mechanism. The resulting structure looks much like a sponge. Due to the bi-continuous, interpenetrating nature, liquids can percolate the whole structure, allowing for material inversion.

3. Simulations and Calculations

Two different kinds of simulations where performed in order to understand photonic properties of various structured materials and to find appropriate parameters for band gap formation. The free[1] software package *MIT Photonic-Bands* (MPB) deals with periodic distributions of refractive index materials and utilises the plane wave expansion method to calculate the energy values of a electromagnetic wave within the dielectric medium for a given wave vector $\boldsymbol{k}$. Another free software package, *MIT Electromagnetic Equation Propagation* (Meep) calculates electric and magnetic fields of an electromagnetic wave propagating from a source through an arbitrary structured dielectric medium. Before going into detail for those methods, the *Pointpatterntool* is described. It was developed in scope of this thesis. Amongst other, it allows to handle different data formats that represent point patterns and to extract standard statistical data from those patterns. It is also used to put the data in a format the simulation software can process. An application of the Pointpatterntool on actual data is given.

Definition of units

As typical for simulations, the question of how the units are chosen needs to be clarified. Whenever reasonable, the characteristic length l_{char} of the respective pattern is used as a unit for lengths. However, the coordinates of points of a given pattern can be distributed in a cube, possibly with periodic boundary conditions. In many cases it is more convenient to use a tenth of a boxlength, denoted by the letter a as the unit of length. The boxlength is hereby one sidelength of the periodic pattern. This is reasonable because Maxwell's equations are scale invariant and the used simulation software uses exactly this unit a as unit of length, if the computational window is chosen properly. For the case of a diamond structure with an average point density of $1\,\text{pts}/a^3$, the characteristic length $l_{\text{char}} = \frac{2}{\sqrt{3}}\,a$. Additionally, the speed of light is set to unity in the software packages, $c = 1$, giving time and lengths the same unit. Frequencies are then expressed in units of c/a.

3.1. Pointpatterntool

This command line tool was designed to be a helper when handling of point patterns is required and basic statistics are to be examined. It is able to generate random or diamond patters and searches for four neighbours to each generated point. The algorithm to define

[1] *Free* by means of the GNU Operating System definition; the software is distributed under the GNU General Public License.

the neighbours is not very sophisticated yet. The points of the pattern are randomly chosen and the four neighbours are assigned to them, under the condition that every point has exactly four neighbours. This can result in odd neighbourhoods, e.g. if the last two points with three neighbours are maximally separated in the dataset. In future work, the Voronoi construction can be implemented. However, a tetrahedral network arises for the diamond case already. Additionally, the tool can read in existing patterns for further processing. The statistics that can be evaluated are the number of neighbours of each node, the length distribution of the distance of a node to its neighbour (similar to a bond length), the angle between the links to two neighbours of a node (similar to a bond angle) and other basic statistics like point density and total number of nodes. The patterns can be of periodic or non-periodic nature. For the non-periodic ones, boundary nodes are defined as nodes that are farther away from any boundary than $1.5\, l_{\mathrm{char}}$, where l_{char} is calculated prior to the exclusion as the expectancy in the length histogram. This has been found to be a well defined measure. Two examples of 2D periodic and non-periodic patterns with linked neighbours are given in Figure 3.1 a), b), respectively, with the excluded area marked blue. All following statistics will exclude these boundary nodes from statistics but uses them if the nodes are neighbours and thus needed for calculation. This way unphysical angles or lengths that can occur at the boundary are excluded. Also the hyperuniformity as defined in subsection 2.3.1 is implemented quite efficiently, where, if present, the periodicity is used to improve statistics. Otherwise the boundary nodes are excluded again to omit any edge effects. The calculation of the difference vectors described in subsection 5.3.3 is also done with the Pointpatterntool. Last but not least, patterns can be visualised with *Gnuplot* or outputted with spherical or cylindrical decorations in *POV-Ray* [73], Meep and MPB, where the latter two are described in the following sections.

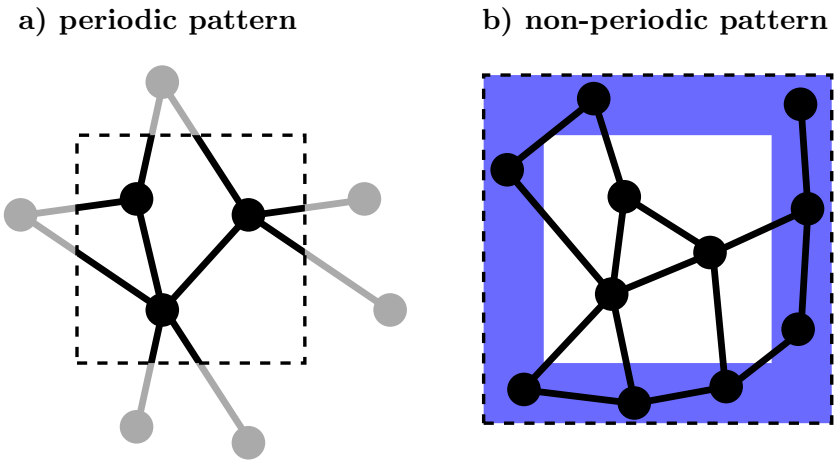

Figure 3.1.: Examples of a a) periodic and a b) non-periodic pattern. Their points are shown black and boundaries dashed. Neighbouring points are connected with rods, depicted as black lines. For the non-periodic pattern shown in b), the points residing in the blue area are boundary nodes and are excluded from statistics. The grey rods and points of the periodic pattern, however, do contribute to the statistics.

I developed the Pointpatterntool particularly for this thesis. However, if research continues, it can serve as a basis for more features to be implemented. Thus, it is written in *C++* to guarantee maximum flexibility. It is also possible to include existing libraries such as *voro++* which calculates the Delaunay triangulation respectively the Voronoi diagram or the *Electromagnetic Template Library* (EMTL) to directly do finite difference time domain (FDTD) simulations. Many more application around point patterns can be thought of, such as generating files for 3D-printers including periodically continued patterns within a suitable supporting structure. It would be of interest to implement more sophisticated pattern generation methods, also to compare them against each other, e.g. by directly calculating the structure factor or pair correlation function. Not yet properly implemented but already working is the calculation of the filling fraction for different decorations with the Pointpatterntool. This is described in the second next section. The tool already proved useful to handle many little (and often annoying) tasks, and has definitely potential to grow further into a fully grown software.

3.2. Hyperuniform Data

Before explaining further methods, the data set which is used often in this thesis is explained. In this work the same hyperuniform point pattern as Ropers [29] had available from our collaborators[2] is used and its properties are reviewed shortly. The dataset can be periodically continued in all three directions, thus the points are occupying a cube of side length $10\,a$. The patterns are depicted in Figure 3.2 (green), together with length- and angle distribution of the bonds to the next neighbours. Additionally, a Poisson (red) and a diamond pattern (blue) are shown for comparison. The data are created and extracted with the *pointpatterntool*.

Each pattern consists of 1000 points that are distributed in a $(10a)^3$ cube with periodic boundary conditions, so that every point has an average volume of one a^3. The hyperuniform (HPU) pattern was constructed using a collective coordinate approach described in [52], with a stealthiness parameter $\chi = 0.13$ as the fraction of the number of constraint degrees of freedom, respectively, the fraction of wave vectors in the isotropic Brillouin zone (BZ) [54] at which the structure factor is set to zero. The neighbours where presumably constructed with the procedure described in [53], applied to three dimensions. However, as currently done with the *pointpatterntool*, choosing the four nearest points as neighbours was found to yield the same result.

Once the neighbours are found, angle and length distribution are straight forward to calculate. The statistics of the diamond pattern are as simple as expected with one single length defining one l_{char} and one single angle, the tetrahedral angle of $\sim 109.5°$. The statistics of the hyperuniform pattern fluctuate around these values with the standard deviation $(1.00 \pm 0.03)\, l_{\text{char}}$ and $(109.3 \pm 9.3)°$, respectively. The Poisson patterns length expectancy value $(0.97 \pm 0.59)\, l_{\text{char}}$ is close to the characteristic length of the hyperuniform sample. This can be explained with the point density that is equal for

[2] Marian Florescu, Paul Chaikin and Paul Steinhardt who also supported information about the optimal filling fraction and scaling.

each pattern. Its angle expectancy value is $(94.0 \pm 37.0)°$. The data is represented in Figure 3.2.

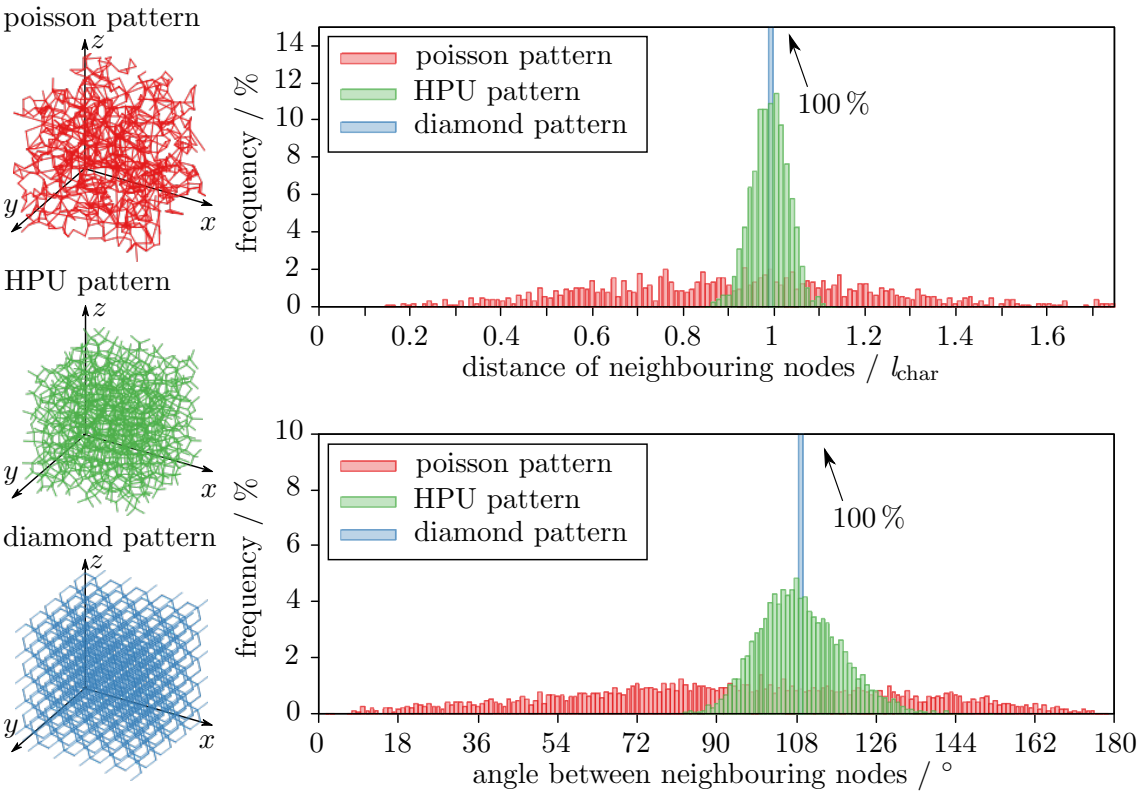

Figure 3.2.: Depiction, length- and angle statistics of three patterns: a Poisson pattern (red), the hyperuniform (HPU) pattern from collaborators (green) and a perfect periodic diamond pattern (blue). Each point in each pattern has exactly four neighbours. The length is normalised to the diamond neighbour distance, which is also the expected value of the hyperuniform pattern.

In order to visualise the structure, the raytracing software *POV-Ray* [73] is utilised to render an image. Shown in Figure 3.3 are cylindrical decorations with a rod-radius of $0.31\,a$, as suggested by our collaborators. Cuts shown in black help to visualise the filling fraction of about $\Phi \approx 37.3\,\%$ [29]. The hyperuniform pattern should resemble the one seen in nature, e.g. compare to birds feather cuts in Figure 5.8.

The structure factor as explained in section 2.3 was calculated with code from Herbert Kaiser [74] and plotted in Figure 3.4. The predictions are well met: for large k the structure factor converges to the average point density of the pattern and the limit $S(k \to 0) \to 0$ shows the absence of long range density fluctuations. The Poisson pattern possesses no order at all and fluctuates around its average point density of $1\,\text{pts}/a^3$. Only at small k a finite size effect is observable. This is the case for all patterns, as well as the noise coming from statistical uncertainty due to the relatively small number of points. Unfortunately, the stealthiness $\chi = 0.13$ for the hyperuniform

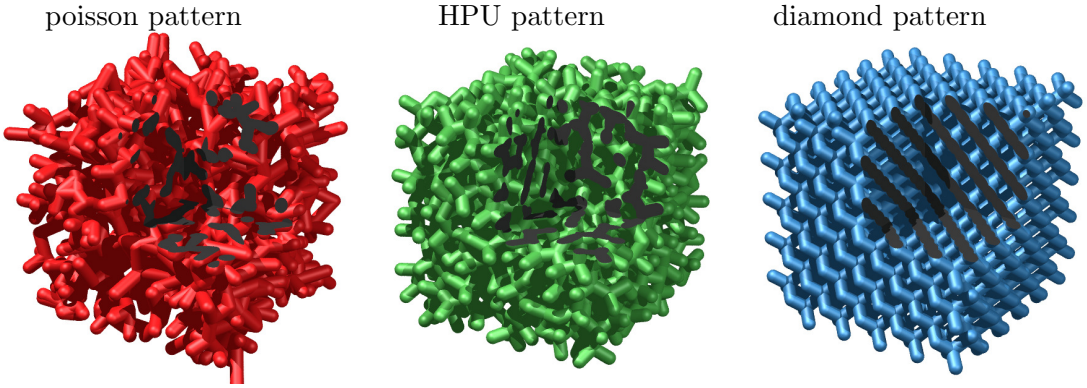

Figure 3.3.: Cylindrical decoration for three different point patterns, rendered with the open source software *POV-Ray*. The radius of the cylinders is $r = 0.31\,a$, which corresponds to a filling fraction of $\Phi \approx 39\,\%$ for the hyperuniform pattern, as calculated in the next section. One octant of the structures is cut away to reveal the inside, the cutting planes are shown in black.

pattern can not be determined due to the lack of data for low k, as the finite size effects and the little number of points does not allow to evaluate the structure factor close enough to $q = 0$. The first peaks of the structure factor of the hyperuniform pattern are essentially smeared out peaks of the diamond pattern, marking the similarity of the hyperuniform pattern and the diamond pattern.

Finally, the degrees of hyperuniformity of the patterns are compared. To calculate the number variance, as defined in Equation 2.17, 10 000 Poisson distributed midpoints are chosen within the pattern boundaries. The points within the sphere of radius $R = 0$ to $10\,a$ centred at the Poisson midpoints are counted. To improve statistics, each pattern was periodically continued, yielding 27 000 nodes for each pattern. For each radius, the expected value is calculated and therefrom the number variance $\sigma^2(R)$. In Figure 3.5 the results together with a quadratic fit for each pattern is shown. The difference between each pattern is strongly evident. The fit to the Poisson pattern is gratuitous, as the variance grows cubic with R rather than quadratic, but still shown for the sake of completeness. The hyperuniform pattern indeed possesses the property of $< N >^2 - < N^2 > \approx R^2$. Strong fluctuations for the diamond pattern occur, coming from its periodicity and leading to an implausible value for the hyperuniformity $A < 1$. Every infinitely periodic pattern should have vanishing point density fluctuations for large distances, thus $A = 1$ [17], shown as the black curve in Figure 3.5. This shows that the calculation of hyperuniformity as done here is more suitable for disordered patterns, but still qualitatively correct.

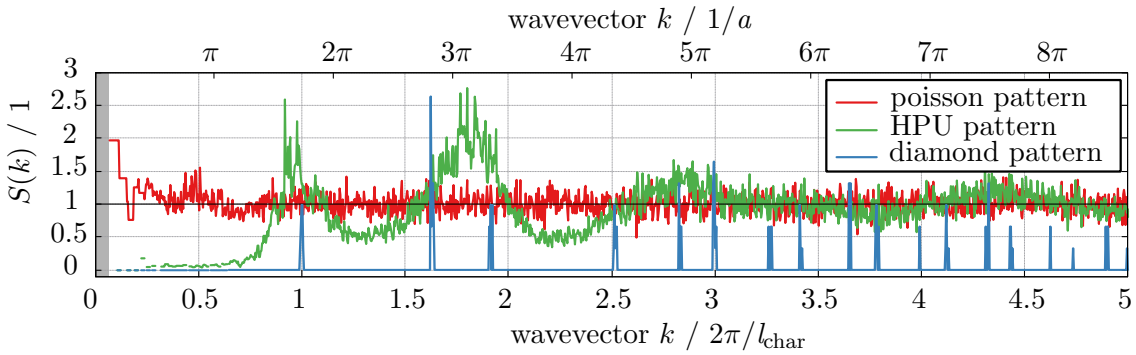

Figure 3.4.: The structure factor for three different patterns, calculated with code from [74]. $S(k)$ for a Poisson pattern is shown in red, the one of a diamond pattern in blue, normalised to its first peak, and shown in green is the structure factor of the hyperuniform data set. The area for low k shaded in grey are 13 % of the BZ of the hyperuniform data, corresponding to the stealthiness $\chi = 0.13$ of the pattern. For all patterns strong noise is present, which shows that large numbers of points are necessary to calculate a smooth structure factor.

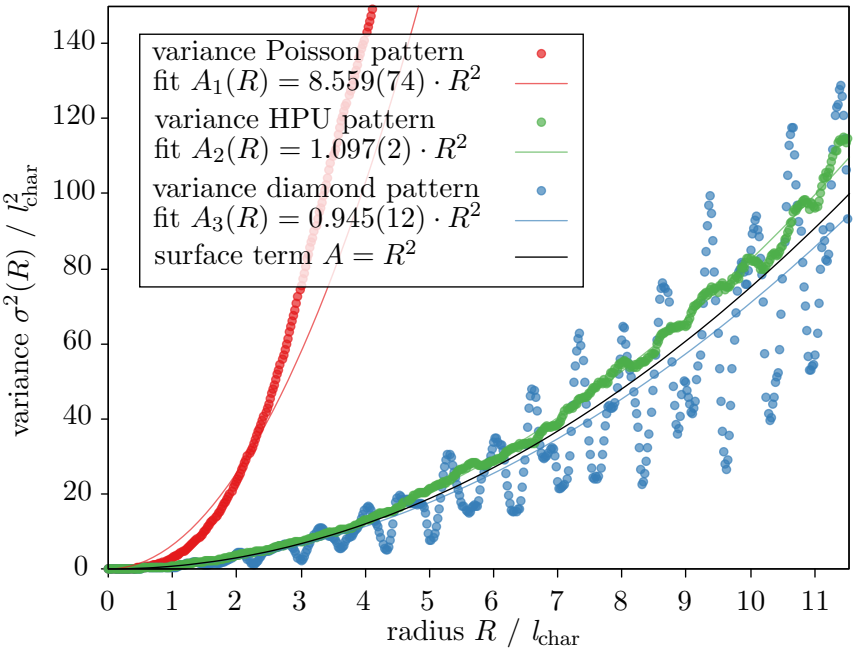

Figure 3.5.: The calculated number variance and hyperuniformity of all three patterns. To ensure better statistical quality, the patterns where expanded periodically in every direction, totalling in 27 000 points. For each of the 500 radii, 10 000 spheres where randomly positioned in the expanded cubicle and the number of points within the spheres where counted. Then, the expectancy value and the variance was calculated for each radius. The data were fitted with a quadratic term to give the prefactor determining the degree of hyperuniformity. The error from the fit of the last decimal is given in brackets. Statistical fluctuations lead to the implausible value $A_3 < 1$ for the diamond pattern.

3.3. Filling Fraction

The filling fraction Φ of a decorated point pattern is defined by the ratio of volume occupied by a high refractive index material in a given total volume as $\Phi = {}^{V_{\text{high}}}/_{V_{\text{total}}}$. It is the characteristic property of a two phase structure and largely influences the propagation of electromagnetic waves in that structure. Depending on the decoration of a point pattern, the filling fraction can be nontrivial to calculate. This is the case for network topologies, where the caps of the linking structures tend to overlap at the patterns nodes. Thus, the filling fraction for the present hyperuniform pattern decorated with elliptical and cylindrical rods has been estimated using a Monte-Carlo simulation, adapted from [29]. Randomly chosen points were therefore tested if they reside within the high refractive index material or in air. If the number of random testing points is very large, the fraction of points within the material to the total number of points is a good approximation for the filling fraction. Therefore, the linking line between neighbouring nodes is densely sampled with interpolation points. The distance between each interpolated point and the current testing point is compared to the radius of the decoration of the link: if this distance is smaller than the radius, the point is said to lie within the high refractive index material.

Figure 3.6 shows the filling fraction for 1×10^6 testing points in the hyperuniform point pattern for two cylindrical and one elliptical decoration. The original pattern as given from our collaborators is intended to have a simple cylindrical decoration. On the one hand, due to the aforementioned issue with the direct laser writing (DLW) fabrication technique, only an elliptical decoration is realisable. On the other hand, however, transmittance simulations are currently only possible for a cylindrical decoration, as described in section 3.5. Therefore, the filling fraction of an effective cylindrical decoration with equal cross section area (of an individual rod) as the elliptical decoration has been calculated. With this, the filling fractions of simulated and fabricated structures become better comparable. The effective cylindrical decoration is found empirically and justified as it fits well enough. The fact that for the elliptical decoration the cross section varies with the angle of each rod respective to z is not taken into account. Instead, the largest possible cross section is assumed, when the rod is perpendicular to z. The actual filling fraction with the elliptical decoration as compared to the effective cylindrical decoration is thus slightly reduced. However, the error in fabrication is thought to be higher than the discrepancy in filling fractions, thus making simulated and fabricated structures comparable. If quantitatively more exact comparisons are in need, more sophisticated effective radii have to be thought of. Until then, radii can be translated with the factor $\sqrt{3}$ from simulation to fabrication. It would be interesting to find an analytical relation between filling fraction and cross section radius, as then the overlapping volume can be estimated. In the fabrication process with DLW, this volume is exposed twice with the laser beam, possibly leading to enlarged areas. The amount of overlap can be estimated by comparing the actual data of the cylindrical decoration with A_3 cross section area to the parabola. The parabola resembles the filling fraction growth without overlap. This may be subject of further investigation if fine tuning of the presented methods needs to be done.

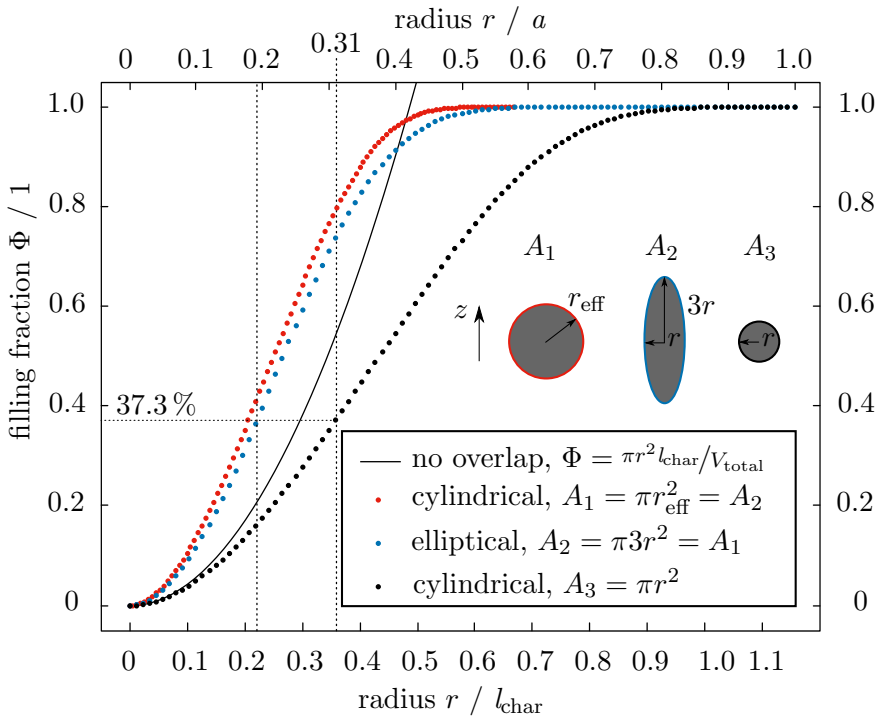

Figure 3.6.: The filling fraction Φ for three different decorations of the hyperuniform point pattern with respect to the radius r of the cross section of the decoration. The vertical dashed lines mark the optimal parameter as suggested by our collaborators and the black parabola the expected growth of Φ if no overlap was present for the cylindrical decoration with A_3. Depicted red and black are cylindrical decorations with two different cylinder radii. The larger cross section has a radius of $r_{\text{eff}} = \sqrt{3}r$, so that its area equals the cross section of the elliptical decoration, whose filling fraction is shown in blue. The cross sections and their areas in grey are shown in the inset, whereby a rod perpendicular to z was taken assumed for the elliptical decoration.

Light of wavelengths much larger than the length scales of the structural variation of $n(\boldsymbol{r})$ is not influenced much by the variation and the effective refractive index n_{eff} can be introduced. This is a strong simplification of the complex propagation of electromagnetic waves in such media, but works quite well as can be seen below in subsection 6.3.1. With the filling fraction, the effective refractive index can be calculated as the weighted average refractive index

$$n_{\text{eff}} = n_{\text{high}} \cdot \Phi + n_{\text{low}} \cdot (1 - \Phi) \tag{3.1}$$

with the refractive indices n_{high} and n_{low} of the high and low refractive index material, respectively, and the filling fraction Φ. Much more sophisticated methods exist for the approximation of n_{eff} for a complex structure, such as the Maxwell Garnett approximation or the energy coherent potential approximation (ECPA), described e.g. in [75]. Those are methods which are again subject of further investigation in terms of applicability to the problem at hand.

3.4. Plane Wave Expansion Method

To study the woodpile structure, the eigenmodes of Maxwell's equations within the periodic structure were computed, using the freely available software package *MIT Photonic-Bands* (MPB) [76]. The method and its specific application are described in the following, summarising [77] and the website of the software shortly. This method is quite widely used in the photonic crystal community to calculate the dispersion relation and a corresponding amount of literature exists on this topic.

3.4.1. Method

Given a wave vector $\boldsymbol{k}$ and a dielectric medium distributed arbitrarily but periodically in space, the homogeneous Maxwell's equations are solved for the allowed frequencies. The constitutive equations are put in Equation 2.6 - 2.9, which are then decoupled. Four equations arise that are similar to Equation 2.10, one for each field $\boldsymbol{E}$, $\boldsymbol{D}$, $\boldsymbol{B}$ and $\boldsymbol{H}$, of which the numerically easiest to solve is chosen. Which one depends strongly on the geometry of the problem, e.g. solving an inverse opal structure yields best numerical convergence by solving for $\boldsymbol{E}$ [77]. The respective other fields can be obtained afterwards by solving Maxwell's equation using the field obtained first. The differential equation to be solved can then be put in form of an eigenvalue problem, with the frequencies as the eigenvalues, one example being Equation 2.10.

The code to calculate the band structure is straight forward and explained in great detail on the website of MPB. Basically, one defines the dielectric mediums geometry of one unit cell and points in k-space in a `ctl`-file and MPB computes the desired number of bands at the given k-points.

With this kind of simulation it is possible to consider the elliptical decoration as obtained by fabrication with the DLW approach. The elongation in z-direction is described in section 4.1 in greater detail. Thus, it is desirable to approximate the rough shape of the focus with an ellipsoid. This is done by using many parallelepiped-objects provided by MPB, as illustrated in Figure 3.7. The idea is to sample a circular cross section with equidistant Θ and than scale the non-z-axes down until the desired ellipse aspect ratio h/w is reached. The new angle is then calculated with $\Theta' = \arctan(\tan(h/w \cdot \Theta))$. The number N of approximating blocks should scale with the chosen resolution res $= 1/r$, with the smallest resolvable distance r such that $N \approx w/r$. Remaining edges will be then smoothed by the MPB algorithm. The parallelepipeds used for approximation have orthogonal x and y axes and a generally non-orthogonal z axis to account for the changing cross section with the angle of the rod respective to z.

As the theoretical hyperuniform pattern described in section 3.2 can be periodically continued, a supercell with the pattern can be formed and theoretically calculated with this method. However, the number of relevant bands increases proportionally with the number of scattering elements in their supercell, similar to the two dimensional case described in [18]. Usually, a band gap can be found between the Nth and $N+1$th band, with N being the number of scatterers in the unit cell [53]. As the number of scattering rods is $N = 2000$ from the 1000 points in the pattern at hand, computation is quite

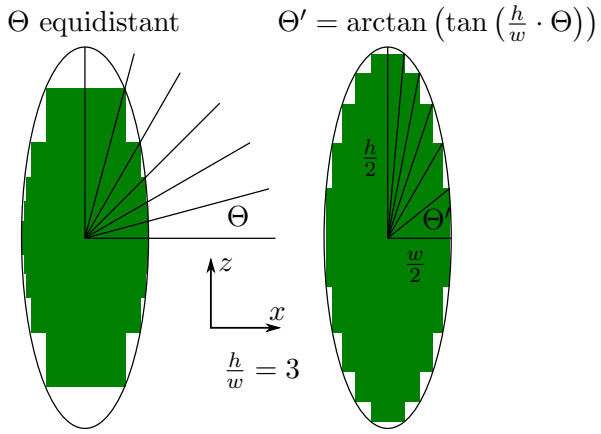

Figure 3.7.: Illustration of the approximation of an elliptical decoration cross section (black outline) for a rod perpendicular to z with five rectangles (green). Choosing Θ non-equidistant clearly gives an approximation that converges with less rectangles to an ellipse. Here, the ratio between both axes of the ellipse is chosen to be $\frac{h}{w} = 3$, as expected from the DLW device.

tedious and time consuming. Results could not yet be obtained, but this method is a promising issue for further investigation.

Complete band structure In order to calculate the complete band structure, the three dimensional k-space needs to be sampled. Fortunately, the symmetry of the geometry can be used and only one octant of the Brillouin zone needs to be sampled. Note, however, that the symmetry of a woodpile is different to that of a diamond pattern decorated with cylinders or spheres. The diamond structure possesses higher symmetry, thus the calculation of a smaller fraction of the Brillouin zone is sufficient. For low refractive index contrasts this can be neglected, as done in [78], where higher symmetry is assumed. As described in subsection 2.2.1, the complete band structure is a three dimensional scalar field and it is thus reasonable to calculate the areas of equal frequency, or iso-frequency surfaces. This surfaces are approximated by triangulation using a *Matlab*-routine. This also allows to calculate the gradient of the dispersion relation along the surface normal at each triangle. Together with the area of the triangle, the density of states is deduced, as defined in Equation 2.13. Results are presented in section 6.2.

3.5. Finite Difference Time Domain

As already mentioned, obtaining the dispersion relation for amorphous structures is quite a difficult task and other means of simulating the structure were consulted. With the finite-difference time-domain (FDTD) method [79], implemented in the freely available software package *MIT Electromagnetic Equation Propagation* (Meep) [80], the electromagnetic field can be calculated directly by solving Maxwell's equations in the time domain step by step. Due to its robustness and accuracy, this method became a standard tool in computational electrodynamics and is widely discussed in textbooks, e.g.

in [81]. Note that with this method the fields are directly retrieved, and from them the transmittance through the sample. A reduced transmittance is in general not enough to conclude to a band gap free of doubt, but further examination is necessary. This can be done e.g. by comparing the transmittance with results from structures with a known dispersion relation.

3.5.1. Method

The algorithm starts by dissecting the computational cell into small voxels, whose size determines the accuracy of the calculation. Due to the finiteness of the cell, boundaries have to be treated specially by cladding them with perfectly matched layers (PML), which completely absorb any electromagnetic field. In the first time step, electric and magnetic fields are initialised to $\boldsymbol{E} = \mathbf{0}$ and $\boldsymbol{H} = \mathbf{0}$. Note that units are chosen such that electric and magnetic fields are expressed in the same units. Then the actual workflow starts by updating the electric field $\boldsymbol{E}$ and magnetic field $\boldsymbol{H}$ using Maxwell's curl equations and the constitutional equations for the electric displacement field $\boldsymbol{D}$ and the magnetic flux density $\boldsymbol{B}$. After updating the respective field, any sources in the computational cell add magnitude to the respective field. A leapfrog integration is used for the updating, meaning the electric field and magnetic fields are calculated on alternating timesteps. This way the mutual inductance of the fields is handled. The question arises at which position in a grid cell the fields should be calculated. In [79] this is solved in a similar manner as the leapfrog integration, and each component of each field is placed at different coordinates. With this so-called Yee-cell, Maxwell's divergence equations are satisfied automatically, making it a very elegant method. The equations are updated until a user defined terminating time step is reached.

With this method the fields can directly be calculated and their visualising gives a perception of how the wave is behaving within the computational cell. In order to obtain concrete quantities from the time dependant fields, postprocessing of the data is necessary. Only by reducing the full wave information, dimensions can be extracted that can be used for comparison with other methods. In this work the transmitted and reflected spectra are of interest as a structure with suppressed transmittance for a range of frequencies is desired. Those spectra can be obtained quite efficiently with the FDTD method, by sending a Gaussian pulse through the cell. By Fourier transforming it, a broad spectrum of frequencies is tested at once. The narrower the pulse is in time, the wider it is in frequency domain, and thus the more frequencies are tested. To obtain the final normalised transmittance, a reference run without a structure in the cell has to be done. The following test case explains the applied method at an example, see subsection 3.5.2.

The geometry in Meep is defined in a similar manner as in MPB and the approximation of the elliptical decoration is the same as above. However, the hyperuniform structure consists of 2000 rods and each rod would be built with at least 20 parallelepipeds. Meep currently can not cope with this amount of objects efficiently to build the matrix representing the dielectric medium and thus further programming needs to be done.

3.5.2. Test case

As a starting point, a theoretically well understood apparatus is simulated: the *Fabry-Pérot interferometer*, also known as an *etalon*. It is depicted schematically in Figure 3.8. The etalon consists of two plane parallel surfaces at distance L, each reflecting light with a certain reflectance R such that multibeam interference occurs. The whole problem could be broken down to one dimension, but as the aim is to prepare simulations for the three dimensional case, the wearisome way is gone here. In the present case, the surfaces are provided by a bulk dielectric medium with lossless refractive index $n_{\text{high}} = \sqrt{2.3}$ surrounded by air with $n_{\text{low}} = 1$ and thickness $L = 10\,a$.

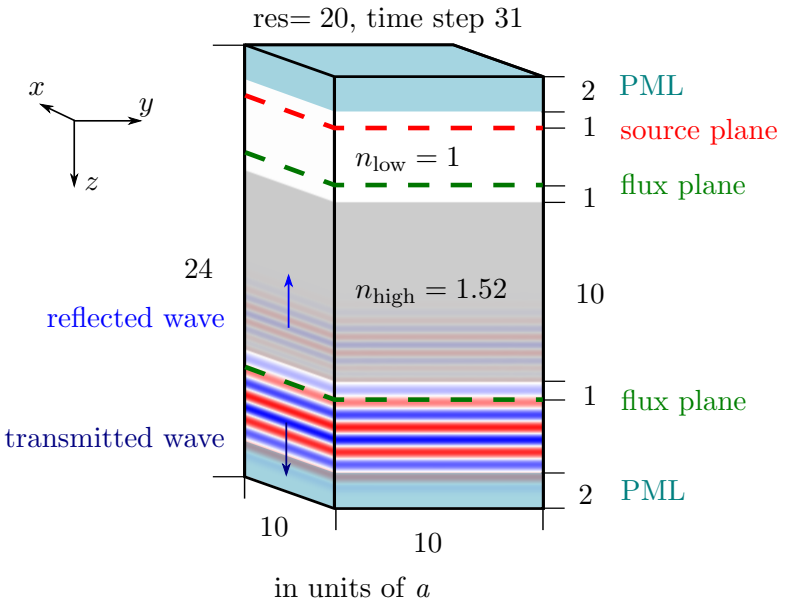

Figure 3.8.: The setup of an etalon. The $10a \times 10a \times 24a$ computational cell is periodic in every spatial direction with absorbing perfectly matched layers (PML) at both ends in z-direction. In this scheme, the magnitude of the electric field component E_x is depicted, negative values in blue and positive values in red. At the shown timestep, the wave packet was reflected at the interface and propagates in $-z$-direction, whereas the stronger, transmitted wave propagates in $+z$ direction.

The transmittance and reflectance spectra shown in Figure 3.9 posses distinct features, determined by the optical path length $n_{\text{high}} \cdot L$ between the two surfaces and their reflectance. In order to be fully transmitted, the wave needs to have a wavelength such that constructive interference of the transmitted parts of the wave can occur. This happens if the transmitted beams are in phase, more precisely when the optical path difference $\Delta L = 2n_{\text{high}} \cdot L$ of two transmitted beams equals an integer multiple of a wavelength $m\lambda$. The factor 2 stems from the condition, that a reflected beam has to pass the box two times more than a directly transmitted one. Further calculation and employing $f = c/\lambda$ leads to the *free spectral range* or separation of two transmittance

peaks in frequency space

$$\Delta f = \frac{c}{2n_{\text{high}} \cdot L} \tag{3.2}$$

of an etalon. Note that the free spectral range corresponds to the inverse round-trip-time of a photon. The quality of the etalon, also called finesse, is measured as the ratio between peak separation Δf and full width half maximum (FWHM) δf of a peak in transmission. In the present case this number is rather low, as the reflection coefficient is quite low. The reflectance can be obtained from the refractive index step using the Fresnell equations for perpendicular incidence as found in standard literature [82]

$$R = \left(\frac{n_{\text{low}} - n_{\text{high}}}{n_{\text{low}} + n_{\text{high}}}\right)^2 \approx 0.04 \tag{3.3}$$

with the refractive index $n_{\text{low}} = 1$ of air (shown white in the inset of Figure 3.9) and $n_{\text{high}} = \sqrt{2.3}$ as the one of the dielectric medium (shown grey in the inset of Figure 3.9). The normalised transmitted intensity I/I_0 as a function of the frequency f of a Fabry-Pérot interferometer can then be calculated with Airy's formula[3]

$$\frac{I(f)}{I_0} = \frac{(1-R)^2}{(1-R)^2 + 4R \cdot \sin\left(2\pi n_{\text{high}} L f\right)^2} \tag{3.4}$$

which can be derived from multi-beam interference, but shall be omitted here. The peak transmittance as well as the airy formula are plotted in Figure 3.9 and are to be compared to the simulation for different resolutions, shown in the same figure. The $10\,a \times 10\,a \times 24\,a$ computational cell as depicted in Figure 3.8 is discretised by the software dependant on the chosen resolution: the higher the resolution, the more discrete voxels are taken into account, the more accurate are the results, but the longer the computation takes. The resolution n discretises the length a into n parts.

The spectra are calculated by sending a Gaussian beam from the source plane in $\pm z$-direction, where the part propagating away from the material is absorbed by the PML. Then, the Fourier transform of electric and magnetic field are accumulated in each flux plane, and by integrating over the plane the total Poynting vector is calculated. Finally, the relative transmittance is derived from division of the flux by that of a reference measurement which took place beforehand, with no material in the box. A detailed description is given on the website of the software package [80]. The input given by the user is the centre frequency of the Gaussian $f_0 = 0.6c/a$ and its width $\Delta f = 1c/a$. The disturbance in the reflection spectrum for the first few low frequency peaks is due to numerical errors, as the amplitude of the Gaussian distributed frequencies is already rather low.

As expected, the simulated peak transmission values deviate more with lower resolution of the simulation. This happens especially for high frequencies, respectively short wavelengths, because each wave period is sampled at less points. Also the dielectric step right at the surface is smoothed out, altering the optical path inside the dielectric

[3] not to be confused with the Airy function as the solution to the differential equation $\mathrm{d}^2y/\mathrm{d}x^2 - xy = 0$

medium. This smearing is done to reduce numerical error, as the spatial derivative of the dielectric medium would theoretically diverge exactly at the dielectric step. The smoothing is reduced for greater resolution, thus the simulation converges to the analytical calculation.

From this test it can be seen, that the calculation can be trusted quantitatively for resolutions above 25 and frequencies below $0.75c/a$. For qualitative results, these limits are more loose, allowing for quick test runs cheap in computational time.

An interesting point to mention here is that a Gaussian wave with a finite FWHM, much smaller than the distance of the reflecting interfaces, is sent through the bulk, but still interference occurs. This can be explained as a Fourier transformed Gaussian consists of an infinite set of wavelengths with each being extended infinitely in space.

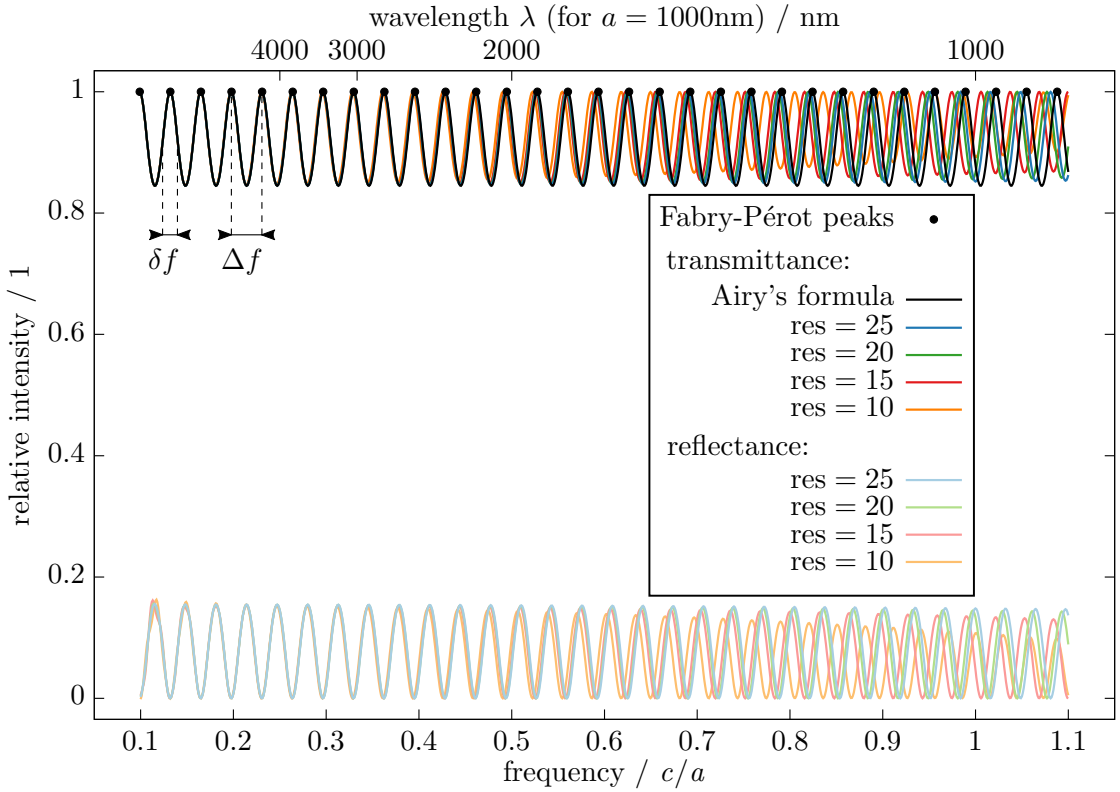

Figure 3.9.: Fabry-Pérot reflectance and transmittance spectra for a bulk dielectric medium with $n_{\text{high}} = \sqrt{2.3} \approx 1.5$ calculated with Meep. The setup is shown in Figure 3.8. The spectra are calculated by sending a Gaussian pulse with centre frequency $f_{\text{centre}} = 0.6c/a$ and width $\Delta f_{\text{G}} = 1c/a$ along $\pm z$ from the source plane, accumulating the Fourier transform of electric and magnetic field of every point in the respective flux plane and calculate the integral of the Poynting vector over the flux plane. The flux is then divided by a reference simulation with no dielectric medium present to finally obtain the relative spectra.

4. Fabrication Methods

Many different approaches exist to fabricate photonic structures. For photonic crystals, the majority relies on the inherent periodicity to speed up the process. The earliest attempt was done by Eli Yablonovitch who drilled holes into bulk material, yielding the so called *Yablonovite*, a structure with cylindrical holes arranged in a diamond lattice [43]. The woodpile structure, developed by two groups simultaneously [70, 71] is another crystal easily assembled by stacking two dimensional layers patterned with lithography, as done e.g. in [72]. Due to its relative simplicity this structure has become widely investigated. It is schematically depicted in Figure 2.11.

Self assembly processes are a completely different and very promising approach [83]. The challenge is to create an environment in which refractive index material can arrange in a defined way. This can work for crystals as well as for amorphous structures. These methods are classified as bottom up methods, as the basic building blocks are predetermined and the wanted structure is grown from these. The problem with this approach is that the results are only vaguely predictable, at least for amorphous structures. Those methods are of interest if large quantities are desired. For this thesis scatterers are to be placed in well defined positions, thus those self organising methods are not further pursued. Nevertheless, spinodal decomposition as one possible self assembly approach is briefly discussed for applicability in section 4.2. It is assumed to be the mechanism behind the formation of the non-iridescent colour for some birds [27].

Amorphous structures are very complicated to produce in a defined way as no periodicity can be exploited. The recent trend to 3D-printing technologies opens up new possibilities, as arbitrarily shaped structures are readily fabricated. The only restriction is that enclosed volumes are sometimes hard to print since remaining raw material needs to be extracted after printing. Also, the motives have to be mechanically stable. This should not be a problem here as the designated structures are bi-continuous. As mentioned above, the interconnected topology can also be exploited for material conversion. 3D-Printers mostly use some sort of plastic polymer material with a rather low refractive index, mostly lower than 2 [84]. Thus, inversion or double inversion processes can be considered. The choice of material of course depends on the frequency regime, absorption is ideally low at the band gap frequency, simultaneously with a large refractive index. In [56] e.g. silicon double inversion was performed on a similar structure, utilising chemical vapour deposition (CVD). The resultant silicon structure has a band gap at around 1550 nm.

Lastly, the question of scaling of the structure arises. Theoretically the scaling only influences the position of the gap in the electromagnetic spectrum, not its general occurrence. For the sake of sample quality, a macroscopic sample is most convenient to fabricate as quite a good knowledge for the governing interaction forces exists. This,

however, leads to a gap in the microwave regime, leading more to a proof of principle rather than a useful application. This was done for two [85] and three dimensions [19]. The really interesting regime is the visible to infrared range where modern telecommunication devices operate. Many components and devices are currently explored for optical circuitry, not only in pursue of the quantum computer. This is also the regime where a combination of photonic and electronic band gaps would be possible to inhibit stimulated emission, as initially suggested by the ground breaking work of Yablonovitch [7]. However, this regime is much more delicate to handle as the governing capillary and Van der Waals forces need to be dealt with. The attempts to deal with these issues are presented in the next section, by explaining the sample fabrication with the direct laser writing method that is capable of nanostructuring a photoresist.

4.1. Direct Laser Writing

***D**irect **l**aser **w**riting* (DLW) is also called two-photon lithography or 3D lithography. It can be regarded as a 3D printing method that is capable of printing features in a photo resist at sizes of 100 nm. With effects like the stimulated emission deletion (STED) even smaller feature sizes are possible [86, 87]. No mask as in standard lithography is involved as the photo resist is exposed directly by the focus of a laser spot. With moving the focus relative to the resist, three dimensional paths can be traced, leading to full three dimensional structures.

The process is described with a negative tone photo resist, meaning the material is cured in the exposed area and excess resin is washed away in the development step. The key process here is the polymerisation of the photo resist due to two photon absorption within the focus spot of a femto-second laser. This nonlinear effect of electromagnetic radiation occurs if the energy density of the photons is high enough so that two photons can be absorbed simultaneously. Only then line widths below the wavelength of the used radiation can be achieved. The absorption leads to a free radical that is capable of starting the polymerisation. A more detailed description of the general chemical process is given in [29], and a review of different materials is found in [88].

In this work, the commercially available table top setup of *Nanoscribe* [89, 90] is used, depicted schematically in Figure 4.1. Much tuning of the optimal parameters was done in [29] and a summary of the usage is given. The liquid negative tone photo resist *IP-Dip*[1] [92] is drop cast onto a glass substrate which in turn is fixed onto the piezoelectric 3D scanning stage. The $100\times, NA = 1.4$ immersion objective focuses the light directly into the resist without passing through the glass substrate. The laser power is set in percent of 20 mW and will be specified in percent in the following. With an autofocus mechanism, the stage searches for the interface between resin and glass substrate. In order to ensure that the printed sample is attached to the glass substrate, the laser is focused $\sim$1 µm in the glass substrate. The maximum possible printing volume reached by the piezoelectric stage is a $300^3 \mu m^3$ cube with a lateral and axial feature size of 120 nm and 360 nm minimum, respectively. A larger volume can be accessed by a motor stage,

[1] In the reference referred to as *IP-L*.

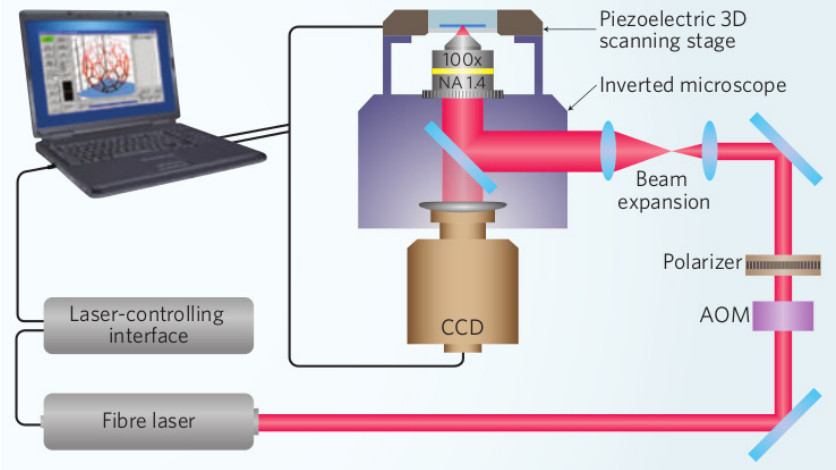

Figure 4.1.: The schematical setup of the Nanoscribe device. The fibre laser works at 780 nm wavelength with 100 MHz pulse repetition rate and 100 mW maximum power [89]. Through an acousto-optic modulator (AOM) the intensity propagated into the resin is controlled in percent of 20 mW. Negligible single photon absorption happens in the resin but mainly two photon absorption in the focus area where the intensity is high enough (laser powers (LP) approximately >21 %). Figure from [91].

however with less accuracy. The optical resolution with 300 nm lateral and 1000 nm axial is interestingly different from the feature size, which can be explained as close by lines fuse to a single one [89]. The writing process can be monitored live via a CCD camera, as depicted in Figure 4.1.

4.1.1. Test of Accuracy

The tracing accuracy and the power distribution along the trace was tested, continuing the work of [29]. Three hexagons, oriented mutually orthogonal in space where printed and, with an option provided by the system, the actual position of the stage and laser power was recorded. There exist several options on how positioning data is fed to the stage. This way printing speed and power distribution can be defined. The most user friendly is the "PerfectShapeQuality" (PSQ) algorithm that interpolates the trace but also smooths sharp edges and adapts the supplied laser power to ensure a uniform distribution along the path. The exact procedure is unfortunately not documented by the company. A more controlled way is possible by providing the number of interpolated points per distance and the number of points actuated per second. With both options, the writing speed can be set. However, there exists no suitable way to efficiently define the distributed power manually. A comparison between programmed and actual trace can be found in Figure 4.2. The influence of the momentum of the stage for every orientation is clearly evident, especially for high velocities. Notably, the influence of the momentum on the actually written path is worse in axial direction. This could stem from the anisotropic moment of inertia of the sample holder for the different rotations. The

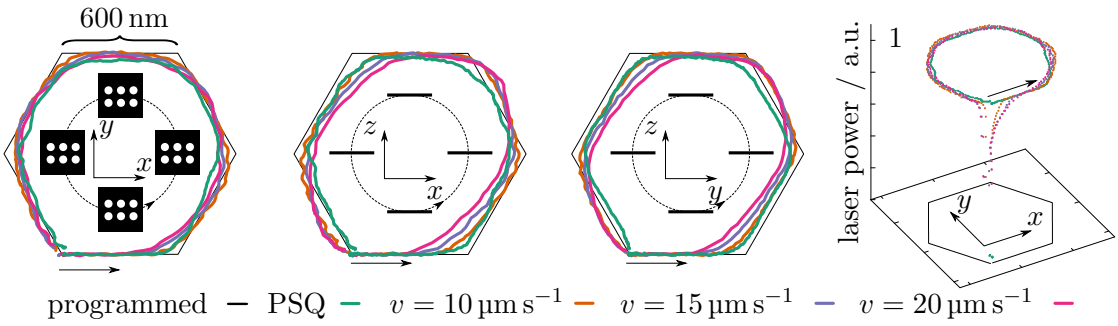

Figure 4.2.: Comparison of specified and actual path of the focus. The arrows indicate the starting point and direction of printing. Clear deviations can be seen for larger velocities. These could stem from a moment of inertia of the sample holder that depends on the angle. Projections of the holder on the according planes are shown as black squares or lines in the insets, respectively. The laser power distribution is rather non-uniform, except for the provided PerfectShapeQuality (PSQ) algorithm.

sample holder has the shape of a flat square in x-y-plane. When moved along a circle respectively hexagon, a rotation with fixed orientation is performed. This is illustrated in the insets of Figure 4.2. In x-y-plane, the moment of inertia is approximately equal at every point, resulting in uniform deviations. As the position of mass contributes quadratic to the moment of inertia, for rotations in x-z-plane respectively y-z-plane, the moment of inertia is different if the sample holder is in top or bottom position to the horizontal ones. This could cause the non-uniform deviations. As seen, the PSQ algorithm performed best overall and is thus used for fabrication in the following. Note that it has the tendency to produce a smaller loop than anticipated. This could lead to smaller l_{char}. As an outlook, there already exists a much faster tabletop system of the same company, the *Nanoscribe GT* which only moves small mirrors to guide the focus in the resin. Due to their small mass, much larger velocities can be driven with more accuracy in position. Also, new software updates improved the performance of the present system and have to be investigated further.

4.1.2. Supporting Structures

For the smallest scaled structure, the question arises how to fix the specimen to the glass substrate. Figure 4.3 shows two samples plainly attached to the glass surface. Due to the shrinkage of the resist during curing and developing the structure is inhomogeneously distorted. However, this occurs only for structures of small scaling, where a small laser power was used to get a smaller structure size.

It has been experimented with several designs to overcome inhomogeneous shrinkage. The optimal supporting structure would reduce shrinkage distortion, be fast to print and had no influence on the printing beam nor on the characterising experiments. Furthermore, it should allow further processing, like inversion methods. Several different designs where tested, and typical results are shown as SEM micrographs in Figure 4.4.

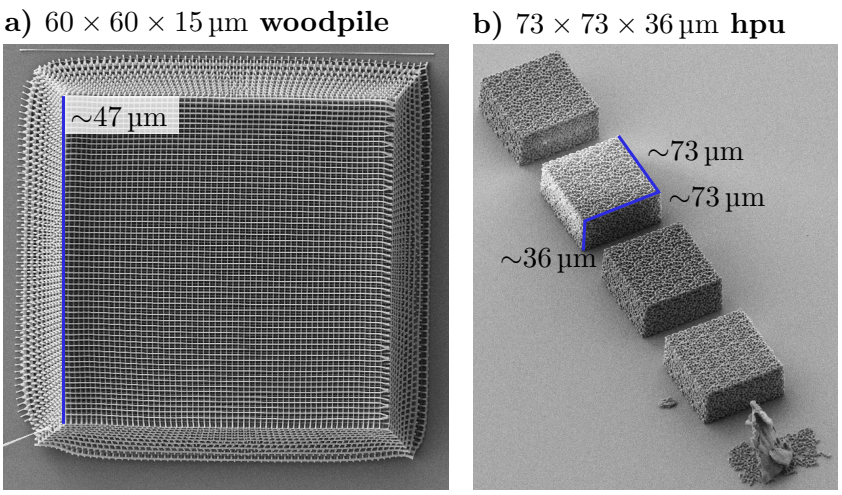

Figure 4.3.: Two kinds of printed structures: a) woodpile specimen with 1 µm programmed rod spacing, b) hyperuniform specimen, with $l_{\text{char}} = 1576\,\text{nm}$ so that a bandgap would be expected at around 3000 nm wavelength, suggested and described in detail in [29]. The former specimen is far more affected by shrinkage (actual rod spacing ~780 nm) of the photo resist whereas the latter one is quite unaffected. If this figures are viewed on a computer monitor, the Moiré pattern in a) due to the limited resolution helps to visualise small distortions near the edge. The Moiré pattern changes with magnification of the image.

To begin with, a trampoline supporting structure was tested, as shown in Figure 4.4, a). A circular wall of thickness 15 µm and diameter d was fabricated. That allows to attach the structure concentrically with different holders, two of which are depicted schematically in Figure 4.4, a). The structure is then printed starting from an outer ring and subsequently reach into the middle. The structure does not touch the glass surface but is held above it, to avoid distortions from the substrate. The effect of distortion for the trampoline is tested on a diamond structure with programmed $l_{\text{char}} = 1\,\mu\text{m}$. Especially at the edges distortions occur, and the pull of a single holder (design 1) is clearly visible. These distortions are long ranged and reach the midpoint of the structure. Therefore, other holders (similar to design 2) were tried. These should give room to compensate shrinkage. However, they were found to be too weak and the holders snapped, leading to largely distorted boundary regions which also extend to the midpoint of the structure. Also, weak concentric distortions arise, when disruptions during the printing process occur. However, the programmed l_{char} is well met.

Another approach was to exploit the shrinkage. Results are shown in Figure 4.4, b). In the beginning of the printing process, a thin scaffold is printed with a comparably high laser power. The structure, printed with lower laser power, is printed attached to it, similar to the trampoline case. Shrinkage of the structure should then leash it to the glass substrate, giving better footing. This approach is partially successive, as the middle section of the large structure turned out to be quite well. This is well seen in SEM imaging, but in other experiments one can not be sure whether high quality regions

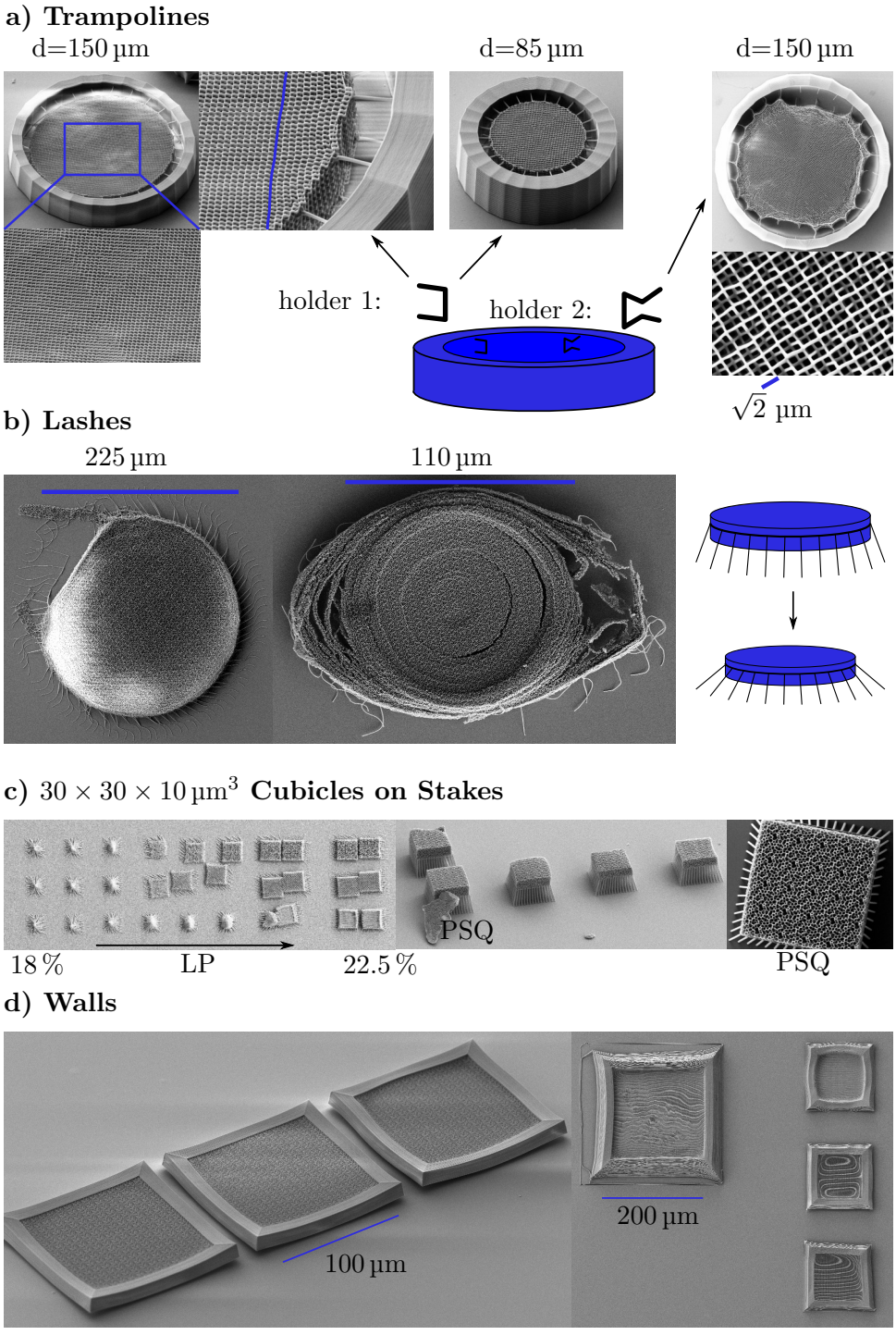

Figure 4.4.: Different supportin structures that have been tried. The structures on stakes depicted in c) and the walls proved to be the most useful ones. A detailed discussion of each structure is given in the text.

are examined or distorted ones. Another result often found is a completely destroyed structure. The circular manner of distortion stems from the concentric writing process.

To better understand the shrinkage process, the structures were printed on stakes ordered in a simple square lattice. These are elastic enough to not disturb the structures shrinkage process. Here, the stakes are 1 µm apart as depicted in Figure 4.4, c). On the first image, the influence of writing speed, power distribution and polymerisation threshold is evident. The laser power (LP) is increased in half percent steps from left to right, as indicated by the arrow. In the top row hyperuniform structures are printed, in the middle row diamond structures and the bottom row woodpile structures. The latter ones allow for larger writing speeds (all printed with the PerfectShapeQuality algorithm), which results in less power distributed per length. Thus, the polymerisation threshold is exceeded only for larger laser powers. As strong capillary forces arise when the developer dries, critical point drying has to be performed, briefly described in the next section. Results are shown in the second and third image. These are printed with a laser power close to the polymerisation threshold. As half of the samples were destroyed the exact parameters are unknown. Different writing velocities were tested against the PSQ algorithm. The latter performed best, yielding least distortion, as shown in the last micrograph. The shrinkage can well be seen as from the programmed 30 µm sidelength only ∼25 µm are left. It has to be kept in mind that with the PerfectShapeQuality algorithm lower laser powers are needed for the hyperuniform or diamond structure. These stake supporting structures are good to ensure relative homogeneous shrinkage. However, it is of little use in optical transmission experiments due to the stakes optical influence.

Finally, it is settled with simple walls as the supporting structure of choice, shown in Figure 4.4, d). They can be widened at the bottom to ensure good footing on the glass substrate, as shown in the second micrograph. Frequently, the strain induced by the shrinkage is large enough to peel edges of, leading to a bent structure. Small footprints of $< 100 \times 100\,\mu m^2$ are found to minimise this sufficiently. The smaller size, however, reduces positioning tolerance in characterisation experiments. Also the influence of the walls will be visible.

4.1.3. Sample Development

Non-exposed resin needs to be rinsed off after the printing process. The sample is placed about 15 min in MR-Dev-600 developer or ethanol and again 1 min in fresh isopropanol. The exact timing and handling has been found not to be critical, proving the stability of the operation. The main forces acting on the structure at these length scales are capillary and Van-der-Waals forces as well as strain due to shrinkage of the resin and drifts in liquid resin. The capillary forces during drying of the developer can be overcome by using a critical point drier. The liquid ethanol is hereby removed by using CO_2 as a replacement medium. Pressure and temperature are controlled in a way that the carbon dioxide is brought from the liquid phase to the gaseous phase over the critical point, omitting the direct phase transition. This way, the capillary forces that occur during drying are eliminated and it is possible to fabricate hair-like structures.

4.1.4. Sample Quality

As already indicated, the lines that can be printed with the DLW technique have an elliptical cross section. This leads to the mentioned elliptical decoration of a point pattern. This inherent feature stems from the energy distribution in the focus of the laser beam. Imagining an iso-energy surface at the polymerisation threshold, the enclosed volume is shaped approximately like a prolate spheroid, i.e. rugby ball. It is this volume in that the monomer polymerises. By dragging the focus in the resist, the cross section of a line printed this way is the projection of the spheroid on the plane perpendicular to the dragging direction. This is an elliptical shape in general and only circular if the focus is dragged along the optical axis. Originally, the elongation, which is along the optical axis z, arises due to the finite aperture of the objective that focuses the light into the resin. The fundamental minimum limit in ratio between short axis w and long axis l of the spheroid thus is 2. In the present case a 100× objective with numerical aperture $NA = 1.4$ leads to a ratio of about $l/w \approx 3$, as found empirically for laser powers near the polymerisation threshold. By increasing the laser power, the size of the polymerising volume can be altered, but the aspect ratio generally changes as well. The lower limit is set by the polymerisation threshold under which the polymerisation would not take place properly. The upper limit was found experimentally to be the power above which the resin starts to boil in the focus and no defined line can be printed anymore.

Another parameter which has to be optimised is the scaling of the printed data set. It determines the characteristic length and together with the laser power the filling fraction is determined, ultimately affecting the band gap position. However, the writing speed apparently decreases with smaller scaling, leading to a higher power distribution at the rods, which thickens the linewidth again. For a rough estimation of the relation between linewidth and laser power see Table 4.1.

SEM micrographs of hyperuniform samples of several characteristic lengths and laser powers can be found in Figure 4.5. The data set is repeated periodically for each sample, such that a volume of $30 \times 30 \times 10$ µm is filled with hyperuniform structure. Samples with $l_{\mathrm{char}} = 346\,\mathrm{nm}$, 433 nm, 519 nm, 606 nm, 692 nm, 779 nm and 866 nm have been fabricated. The writing speed varies as the focus traces the connection between two nodes: the stage needs time to accelerate and decelerate, thus the energy distribution is not homogeneous. Node points are printed larger as they are exposed multiple times. Thus, lateral and axial linewidths are rather difficult to diagnose. The line width measured approximately between two nodes can be found in Table 4.1 for three hyperuniform samples with various characteristic lengths. For the stakes themselves, printed with 40 % laser power, a line width of $(430 \pm 25)\,\mathrm{nm}$ was found. The increase of linewidth for smaller l_{char} is apparent. These numbers suggest that slightly less than 606 nm is a good characteristic length in terms of optimal filling fraction of about 40 %, as read from Figure 3.6.

The findings suggest, that l_{char} and the laser power as controllable parameters are not independent. The characteristic length determines the filling fraction directly by geometry but also indirectly due to changing writing speed, thus power distribution and thereby linewidth. This way the laser power directly influences aspect ratio and

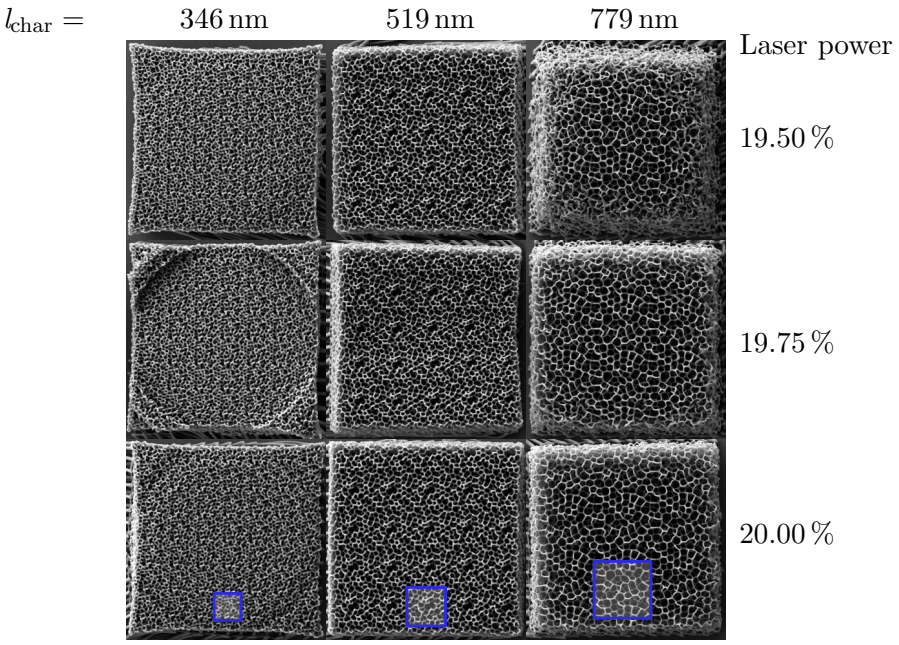

Figure 4.5.: Micrographs of fabricated structures from the hyperuniform data set, printed with different scaling and laser power. All printing is done with the PerfectShapeQuality algorithm. The circular distortion arises as the writing process starts from the middle and due to apparent shrinkage during exposure. Note the concave outline of the structure with the shortest l_{char} that indicates a high filling fraction. The highlighted squares indicates the periodicity of the data set.

linewidth, and by that the filling fraction. The crux is, that due to shrinkage the characteristic length is influenced again. This makes finding appropriate parameters quite tedious.

Conspicuous is the repetition of the pattern due to the periodical continuation. This is expected to lead to a periodic reciprocal lattice, with the lattice spacing corresponding to the reciprocal period length overlaid by a ring indicating the isotropy of the data set. As described in section 2.3 as clustering, larger characteristic lengths occur, resulting in peaks of the structure factor for low $\boldsymbol{k}$. The pattern in reciprocal space can easily be calculated from an SEM micrograph, as shown in Figure 4.6. It represents the structure factor as the absolute value of each Fourier component is shown. Clearly visible in Figure 4.6 is the periodic repetition of the pattern, in both direct and reciprocal space. The dataset was scaled to a cube of 1 µm side length, which resulted in a structure with about 9.3 µm periodicity. The discrepancy is attributed to shrinkage of the photo resist. The characteristic length was programmed to 866 nm. A reliable resultant value can not be read from the images as the circle is smeared out too much. This could indicate non-uniform distortions, weakly visible in the lower right portion of the direct space image. Isotropy in x, y plane seems present nevertheless.

Due to the elongation in axial direction, the structure can never be truly isotropic. The SEM micrographs shown above only show the outside of the structures. The question

Characteristic length $l_{\mathbf{char}} = 779\,\mathrm{nm}$

laser power / %	line width w / nm	$r = w/2$ / $l_{\mathrm{char}} = 779\,\mathrm{nm}$	$\Phi \pm 2\,\%$ / %
19.5	160 ± 10	0.10 ± 0.01	12
19.75	170 ± 10	0.11 ± 0.01	14
20	180 ± 10	0.12 ± 0.01	16

Characteristic length $l_{\mathbf{char}} = 606\,\mathrm{nm}$

laser power / %	line width w / nm	$r = w/2$ / $l_{\mathrm{char}} = 779\,\mathrm{nm}$	$\Phi \pm 3\,\%$ / %
19.5	192 ± 10	0.16 ± 0.01	24
19.75	182 ± 10	0.15 ± 0.01	24
20	191 ± 10	0.15 ± 0.01	27

Characteristic length $l_{\mathbf{char}} = 433\,\mathrm{nm}$

laser power / %	line width w / nm	$r = w/2$ / $l_{\mathrm{char}} = 433\,\mathrm{nm}$	$\Phi \pm 4\,\%$ / %
19.5	192 ± 10	0.22 ± 0.01	46
19.75	202 ± 10	0.23 ± 0.01	50
20	217 ± 10	0.25 ± 0.01	56

Table 4.1.: The linewidth with respect to the laser power for the hyperuniform dataset, scaled to various characteristic lengths. To make the data comparable, the half line width r is given in units of l_{char}. The numbers are read from the SEM micrographs, the errors are approximated.The corresponding filling fraction Φ is calculated from the data of the elliptical decoration in Figure 3.6.

arises how distortions influence the inside of a sample and how well the desired filling fraction is met. The focused ion beam (FIB) is utilised to cut through samples, described in section 5.3 in detail. Resultant SEM micrographs are shown in Figure 4.7. The FIB current tends to melt and distort the resin, so a clear cutting edge can not be obtained. Conclusions on quantitative numbers for the lines axial elongation are thus not possible. The fabrication results for the samples with short characteristic lengths can be expected from the resolution of the Nanoscribe. It is given with 300 nm lateral and 1000 nm axial [89]. For short characteristic lengths <433 nm a bulk material can thus be anticipated. Surprisingly, samples with $l_{\mathrm{char}} = 433\,\mathrm{nm}$ turn out quite well structured. However it is unclear how well the desired shape is met. This l_{char} is taken as a lower limit.

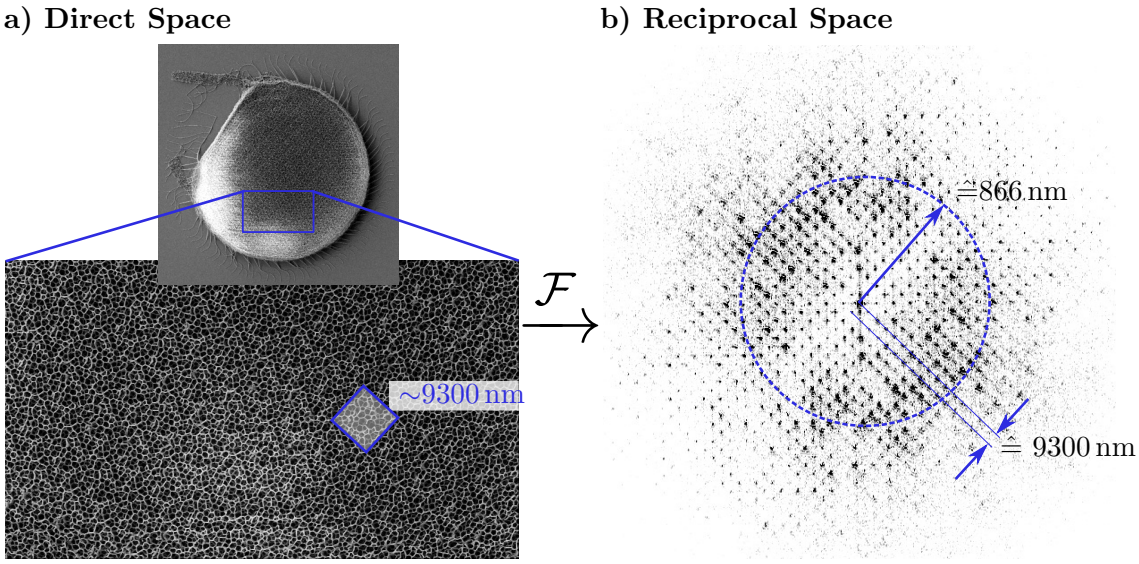

Figure 4.6.: a) Direct image of the hyperuniform structure and b) reciprocal image from Fourier transformation of the SEM micrograph. The highlighted area is the unit cell with about 9300 nm side length. The smeared out circular pattern in the Fourier image indicates the isotropy in x, y direction. The circle is smeared out too much to measure a tenable characteristic length; programmed were 866 nm as indicated by the circle. The quadratic grid results from the periodically continued pattern. Ideally, an inner circle should show zero intensity as infinite wavelength density fluctuations should vanish. Because the transformed area is finite, boundary effects show up in the centre of the Fourier transformed image as a cross.

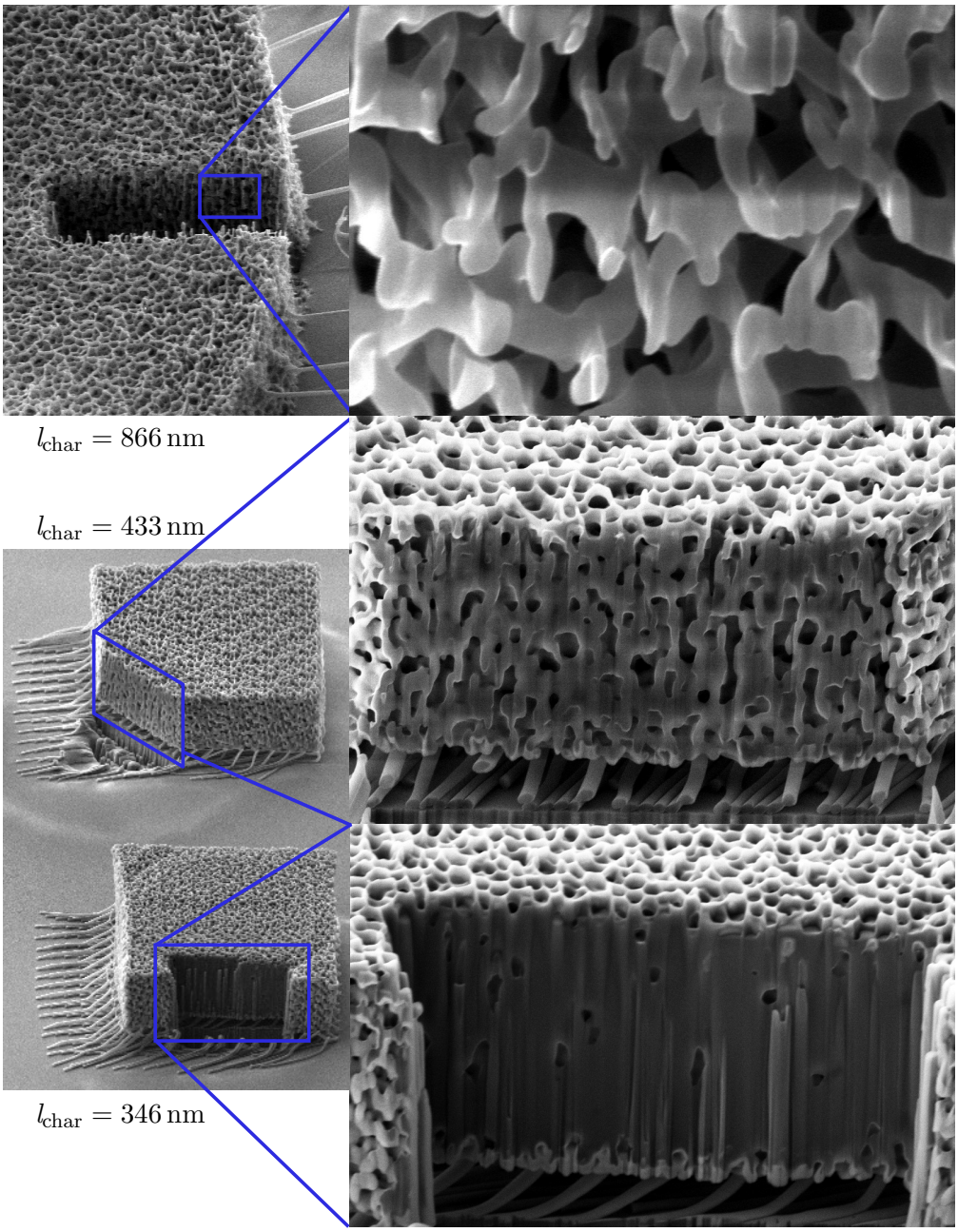

Figure 4.7.: The quality of the inside of the structure is demonstrated using the FIB and SEM micrographs. As can be expected from the resolution limit of the DLW device, the structure with shortest l_{char} is effectively a bulk structure. The elongation in axial direction can well be seen for the largest l_{char}.

4.1.5. DLW Conclusion and Outlook

The characteristic length and the laser power are the two main parameters that can be controlled. However, both influence the filling fraction of the sample separately. This makes it difficult to fabricate samples with well defined properties. The parameter space is shown schematically in Figure 4.8, deduced from the presented findings. Due to the limited resolution of the Nanoscribe device, a filling fraction of the desired 37.3 % is difficult to achieve because the rods tend to agglutinate and a bulk sample is obtained. Regarding the filling fraction, with a characteristic length of $l_{\mathrm{char}} pprox{\sim}600\,\mathrm{nm}$, reasonable samples can be expected. However, further quantifications need to be done. To do so, a sophisticated method to extract the resultant linewidth and characteristic length needs to be developed. Only then the relation of the parameters can be used to fabricate a structure with well defined characteristics. Due to the elongation of the

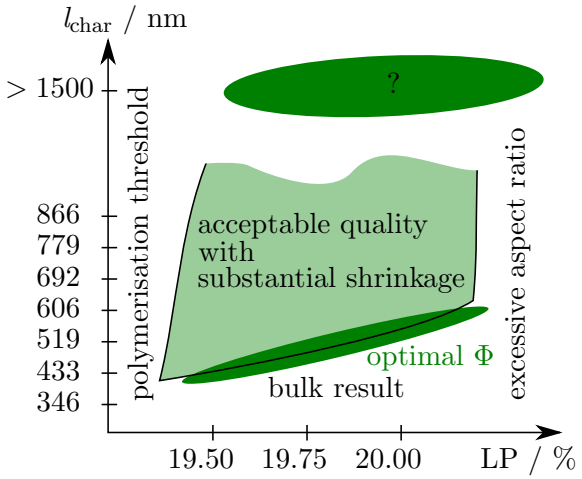

Figure 4.8.: Sketch on the independently controllable parameter space and regions where reasonable results are assumed. A structure with optimal filling fraction is assumed to posses a band gap or band stop. The characteristic length of the data set directly determines the filling fraction Φ as well as the the laser power (LP) distribution due to changing velocities of the stage, and with that the line width. The laser power directly influences the line width and its aspect ratio, which both determines the filling fraction Φ. Also the amount of shrinkage is influenced by the laser power, and with that the characteristic length. Further quantification of the parameter space needs to be done.

focus, isotropy of the sample at these small length scales is impossible to achieve. The presented method is thus not suitable to reproduce structures like those found in biology. Neglecting isotropy, it is still worthwhile to put further effort in exploring the parameter space, particularly with regards to material conversion. Simulation results as shown later (subsection 6.3.2) reveal that a higher refractive index contrast eases the formation of a band gap. Additionally, if the photo resist can be converted to a higher refractive index material, a lower filling fraction is needed in order for a band gap to open. Another approach is to target the fabrication of a larger scale sample. This was

already suggested by Ropers and larger scale structures have been written with the algorithm explained in [29]. A resultant sample is shown in Figure 4.3. The shrinkage is negligible and the rods cross section is close to circular. However, if present at all, any band gap is then shifted to the far infrared, which is a more difficult regime to handle, as less optical devices exist and those who do are expensive. Those experiments that allow for characterisation of those samples are still under construction.

Of large interest would be to measure the filling fraction Φ of a fabricated sample, with a non-destructive experiment. This would quantify the quality of the sample by a single number, assuming structural stability. One could measure $\Phi(\mathrm{LP}, l_{\mathrm{char}})$ for each specific point pattern, which is also of interest if material inversion is done. Together with the results from SEM micrographs for the linewidth, the actual elongation could be quantified. An optical experiment that measures n_{eff} would be elegant, such as an interferometer. With Equation 3.1 one can then conclude to Φ.

The direct laser writing field is currently rapidly evolving, especially with respect to available scale range, writing speed and quality. The used setup is already outdated, as the faster *Nanowrite GT* is available. The fundamental difference is that mirrors are moved instead of the massive sample stage. Much less mass needs to be move, which allows for high writing speed and well accuracy. Also, the stimulated emission depletion (STED) technique reduces the linewidth further and could be a candidate to allow for fabrication of hyperuniform photonic structures with a band gap in the near infrared or even visible.

4.2. Spinodal Decomposition

Naturally, a possible approach to fabricate amorphous bandgap structures would be to copy nature. However, the exact process is utterly complex and not yet well understood. It is debated that *spinodal decomposition* is responsible for the sponge like structure in feather barbs [27]. This is indicated by scattering experiments done with the feather barbs and comparable spinodal decomposed polymers. Described in a few words, the effect can be explained with the phase diagram (temperature versus mixing ratio) of a binary mixture, see Figure 4.9 for a schematic drawing. If the respective chemical preconditions are met, there exists a high temperature region at which the two liquids totally miscible as favoured by the thermodynamic equilibrium. By a rapid cooling process, the mixture can be brought into the miscibility gap, where the two components rapidly decompose, as the thermodynamic equilibrium now favours two separated phases. Depending on where exactly the mixture is brought in the miscibility gap, droplets of the liquid with lower volume fraction develop with a nucleation and growth process, or if supercooled stronger, the mixture decomposes spinodally. This is the region where the peculiar nanostructure evolves. This nanostructure usually coarsens over time. The whole effect can be derived from the Gibbs free energy. A more detailed discussion shall be omitted here but it is referred to literature [93]. The supposed process in the birds feather barbs is that the raw keratin is formed in keratinocytes, where it then decomposes in the cytoplasm. During or after this process, the keratin polymerises, the

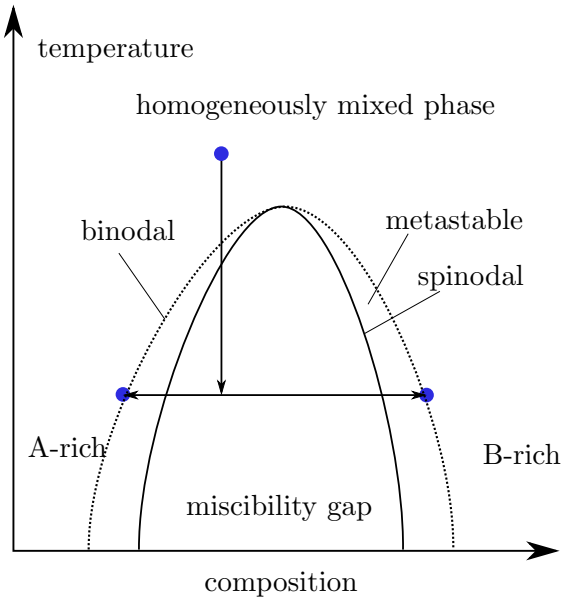

Figure 4.9.: The schematic phase diagram to explain spinodal decomposition. For large temperatures, two liquids A and B mix to form a homogeneous phase. With rapid cooling, they can be brought to the miscibility gap. There, nucleation and growth happens or the spinodal decomposition, respectively, dependant on whether the mixture resides below the binodal or spinodal. The exact positions and quantification depends on the chemical liquids.

cell dies and the final structure emerges.

For the reproduction, one could let a binary mixture of a monomer and a solvent decompose, and then shock freeze the whole system once the desired spatial fluctuation is reached. By then curing the monomer, for example with high energy photons, the structure might be fixed. By unfreezing the whole system and removing the solvent, the structure may be retrieved. The whole process can be monitored with a scattering experiment, as done in [94]. This is a large field of research with a lot of chemistry being involved, beyond the scope of this thesis, but might be addressed in future work.

Kumano *et. al.* [95] tried to fabricate structural colour by spinodal decomposition, but stumbled upon the so-called Christiansen effect [96]. This is another interesting colourgiving mechanism, which origins in different dispersion relations of two media, as depicted in Figure 4.10. At the frequency where the dispersion relations intersect, light propagation is not influenced by any interfaces between both materials. Even if there are a lot of them, as available in a powder of material with $n_1(\omega)$ residing in the respective other material with $n_2(\omega)$. For other frequencies than ω_0, the interfaces scatter the light away, altering the transmission properties of the material mixture. In particular, light with frequency ω_0 will be fully transmitted, whereas light with any other frequency is scattered away resulting in reduced transmittance. As the dispersion relation often depends on the temperature, the point of intersection ω_0 can be tuned. One can build a device that indicates temperature with a distinct transmitted colour [96].

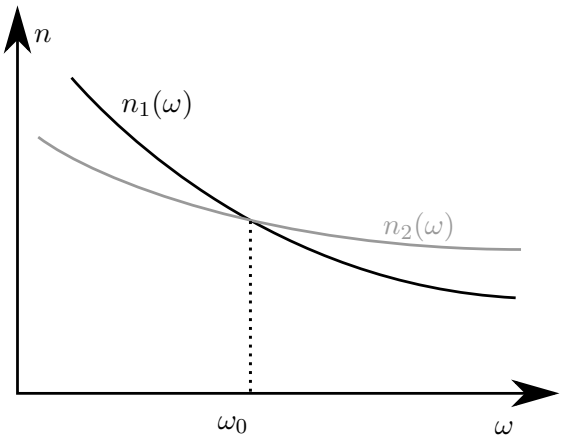

Figure 4.10.: On the Christiansen effect, whose origin lies in intersecting dispersion relations $n_i(\omega)$ of two materials $i = 1, 2$. Light propagating with frequency ω_0 will not be affected by interfaces between materials with $n_1(\omega)$ and $n_2(\omega)$, respectively, but light with any other frequency will be scattered.

5. Methods to Characterise Samples

A precise method to investigate samples in direct space is the scanning electron microscope (SEM). However, this method is destructive in several ways: the sample has to be sputtered with gold to eliminate charge effects, the photo resist is shrunk by the electron beam and the FIB has to be used to examine the inside of a sample. Furthermore, it is quite difficult to read out quantitative data. Advanced image processing has to be done such as Fourier transforming the images to obtain information on any characteristic lengths for example. The results strongly depend on the image quality, altogether give rise to the need of more sophisticated methods. To be able to characterise a sample without destroying it, a scattering experiment was set up. Its characteristics are discussed in the next section. Furthermore, a spectroscopy setup is discussed that should be able to identify a photonic band gap of a sample, if present. Finally, a method to obtain the full volumetric data of a spongy keratin structure is presented and validated.

5.1. Scattering Experiment

The goal of this experiment is to provide a tool to examine properties of fabricated samples in a non-destructive way. A scattering study should be suitable for this task. The relatively simple setup is depicted in Figure 5.1. Unfortunately, the setup was built at the late stage of this thesis, and mainly qualitative data could be generated. Nevertheless, it has the potential to become an important tool to investigate photonic materials. Thus, its physical principle is discussed here and improvements are given in the outlook. Monochromatic, collimated coherent light of wavelength $\lambda = 532\,\mathrm{nm}$ is shaped appropriately with a pinhole of diameter $50\,\mu\mathrm{m}$. If the distance d_{ps} is chosen small, the occurring Airy disk of the pinhole can be neglected as it is at angles close to the zeroth order diffraction peak. In order to minimise effects from the supporting structure, the sample needs to have a footprint at least the size of the pinhole. The light is diffracted and displayed at a screen at distance d_{ss} far away from the sample. For samples with a low refractive index contrast, the Born approximation holds, as explained in the theory chapter, section 2.4. This results in the Fraunhofer pattern on the screen. Fourier optics apply, and the image seen on the screen is essentially the absolute value of the Fourier transform of the sample. More precisely, it is the Fourier transform of the plane perpendicular to the incident wave vector. Through rotation, planes different from the x-y-plane can be probed in order to measure the effect of the elliptical decoration. This could not be tested in detail yet, but is a task for further study.

For samples of height around $20\,\mathrm{m}$, the kinematic scattering approach can be assumed for refractive index contrasts of $\Delta n < 0.05$ [59]. Figure 5.2 shows resultant patterns on the screen for different Δn. This was reached by infiltrating the sample with ethanol,

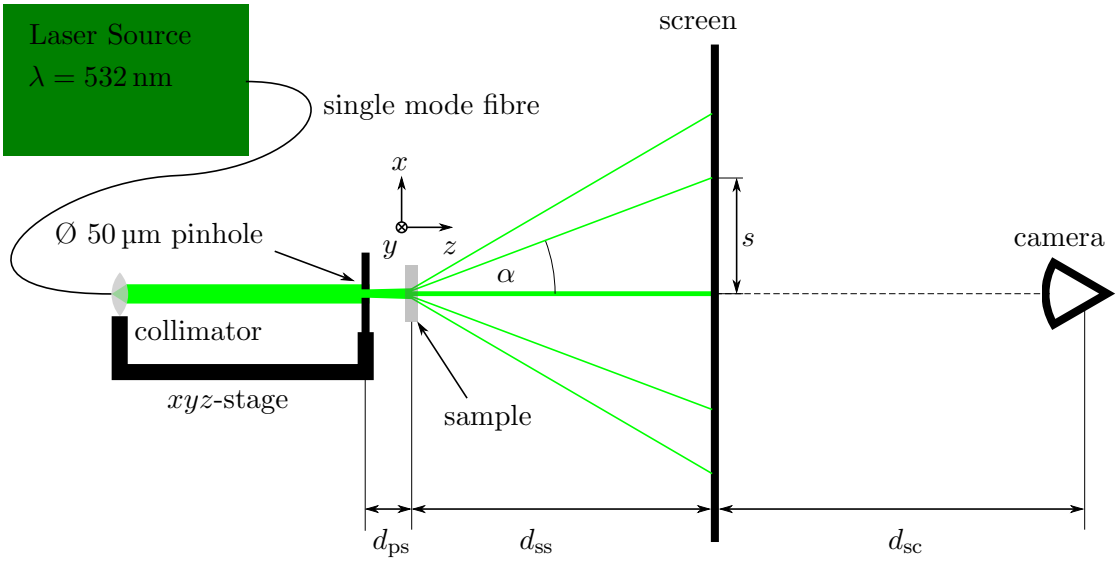

Figure 5.1.: Sketch of the setup of the scattering experiment. Collimator and pinhole sit on a xyz-stage so that they can be shifted relatively to sample and screen. The camera is capable of taking long exposure images so that pictures can be taken in the dark to minimise unwanted influences. A discussion on the scattering angle α is given in the text.

$n_{\mathrm{ethanol}} \approx 1.36$ at $\lambda = 532\,\mathrm{nm}$. The effects of changing Δn can instantly be observed on screen.

In Figure 5.2, the cross shape at the origin stems from the walls that support the structure, which all have a footprint of $100 \times 100\,\mu\mathrm{m}^2$. It was $d_{\mathrm{ps}} \approx 1\,\mathrm{cm}$, $d_{\mathrm{ss}} = 10\,\mathrm{cm}$ and $d_{\mathrm{sc}} \approx 30\,\mathrm{cm}$. Marks on the screen (not shown) enable to measure the distance of diffraction peaks from the zeroth peak. The effects of multiple scattering can strikingly be seen. The information on the structure is completely lost for large refractive index contrasts, Figure 5.2 a). From a pure speckle pattern a rectangular lattice pattern (Fig. 5.2 b)) emerges, and vice versa when the ethanol evaporates. A ring proving isotropy is not seen as the contrast is still too high and multiple scattering occurs. Information on the periodicity of the periodically continued hyperuniform pattern can well be extracted, however. To further reduce the refractive index difference, the diffraction pattern of a non-developed sample was recorded, shown in Figure 5.2 c). The exact contrast has not been quantified here, Brüser *et. al.* [59] suggest $\Delta n \approx 10^{-3}$, whereas the data sheet of the photo resist suggests $\Delta n \approx 0.04$ [92]. The effects of single scattering can be seen, where the form factor multiplies with the reciprocal lattice. Naturally, the signal has much lower intensity. A ring can be seen, indicating isotropy in x, y plane. Unfortunately, possible shrinkage and distortion caused by the development step are not taken into account then. The diffraction pattern is remarkably close to the Fourier image of a similar sample, shown in Figure 4.6.

The Bragg equation deduced from the scattering vector $|q| = {}^{2\pi}/_{d} = |\boldsymbol{k}_{\mathrm{out}} - \boldsymbol{k}_{\mathrm{in}}|$ is used

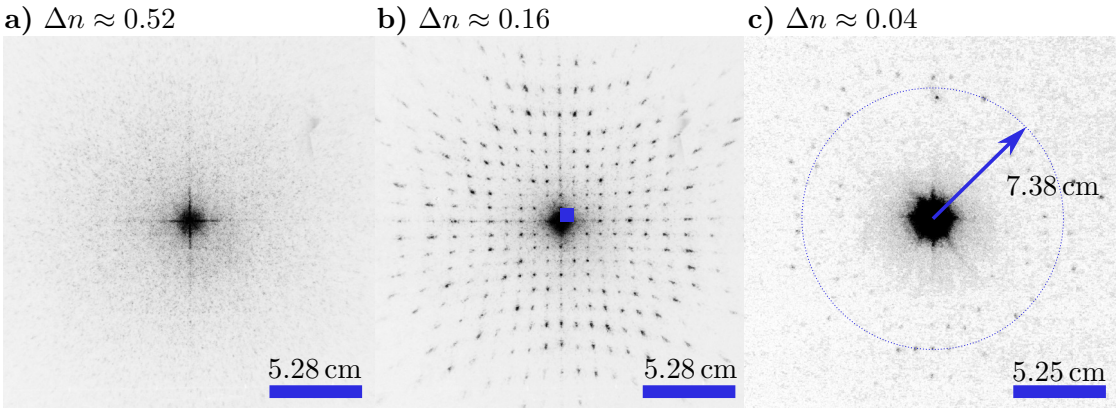

Figure 5.2.: Experimental data of the scattering setup of hyperuniform samples with $l_{\text{char}} = 611\,\text{nm}$ (corresponding to 7.05 µm periodicity) and three different internal refractive index contrasts. Depicted are diffraction patterns of a $\lambda = 532\,\text{nm}$ laser beam, whereby the inverted green channel of the camera image is shown. a) shows the structured photo resist in air fabricated with 20 % laser power, b) the same sample infiltrated with ethanol, $n_{\text{ethanol}} \approx 1.36$. The distance of the first order diffraction peak to the zeroth is 0.75 cm on screen (blue square). The transition from the ethanol infiltrated structures diffraction pattern to the one of a structure in air can be spectated when the ethanol evaporates. c) shows a sample in non-exposed resist, fabricated with 22 % laser power. The hexagonal shape of the zeroth order spot in c) is due to the aperture of the camera.

to determine the lattice plane distance d that is scattered at (compare to section 2.3):

$$d = m \cdot \frac{\lambda_0}{2n_{\text{eff}}} \cdot \frac{1}{\sin(\Theta)} \quad \text{Bragg's law} \tag{5.1}$$

$m \in \mathbb{N}$ is hereby the order of the peak and the Bragg angle Θ half the angle between $\boldsymbol{k}_{\text{in}}$ and $\boldsymbol{k}_{\text{out}}$, see Figure 5.3. λ_0/n_{eff} is the wavelength of the incident wave in the medium. Taking the effective refractive index is justified for small refractive index contrasts, wherefore the band structure closely resembles the one of a homogeneous medium. The relation of the Bragg angle Θ to the scattering angle α is determined by Snell's law.

The diffracted light needs to decouple from the sample, the process is shown in Figure 5.3. Due to this refraction during the decoupling, the pincushion effect emerges. Large Bragg angles are enlarged further, and appear farther away from the zeroth spot on the screen, see Figure 5.2. As the distance from sample to screen is large with respect to the sample size and substrate thickness, any beam displacement by the sample or the glass substrate is neglected here. From Snell's law it holds

$$\Theta = \frac{1}{2} \cdot \arcsin\left(\frac{n_{\text{air}}}{n_{\text{eff}}} \sin(\alpha)\right), \tag{5.2}$$

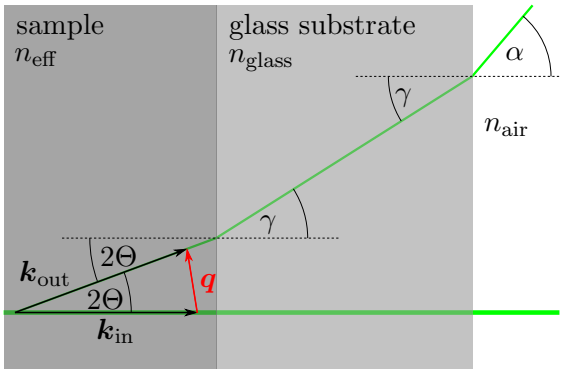

Figure 5.3.: Decoupling of the scattered light from sample and glass substrate. The effective refractive index of the sample is determined by the refractive index of the infiltrated substance, the filling fraction and the refractive index of the polymer with Equation 3.1. The glass substrate does not influence the scattering angle α, but causes a beam displacement.

with the scattering angle $\alpha = \arctan\left({}^{s}/_{d_{\text{ss}}}\right)$, measureable from the screen. For Bragg angles larger than $\Theta_{\text{max}} = {}^{1}/_{2} \cdot \arcsin {}^{n_{\text{air}}}/_{n_{\text{eff}}}$, total internal reflection takes place, as then $\alpha \geq 90°$. This sets a fundamental limit on the observable Bragg angle, and with that on the minimal resolvable sample feature.

One could think of measuring the effective refractive index by examining a shift of the peak with changing effective refractive index for the sample sample. This would allow for deduction of the filling fraction Φ according to Equation 3.1 and make this an even more powerful experiment for characterisation. Unfortunately, however, the effects of changing n_{eff} affect the Bragg scattering and the decoupling after Snell contrarily. This can be seen by substituting α from Equation 5.2 in Equation 5.1, resulting in $\alpha = \arcsin\left({}^{n_{\text{eff}}}/_{n_{\text{air}}} \cdot \sin\left(2 \cdot \arcsin\left({}^{m\lambda}/_{2dn_{\text{eff}}}\right)\right)\right)$. This term changes very little with the physically plausible values $1.0 < n_{\text{eff}} < 1.54$ ($\sim$0.0002 % change for the extreme values, $\lambda = 532\,\text{nm}$, $d = 10\,\mu\text{m}$, $m = 1$), yielding immeasurable change in angle considering the measurement error. A measurement of n_{eff} with this method is thus impossible.

If the filling fraction is estimated to $\Phi \approx 27\,\%$ from a characteristic length of $l_{\text{char}} = 611\,\text{nm}$ (see previous chapter Table 4.1) and the refractive index of ethanol $n_{\text{ethanol}} = 1.36$ is taken, the effective refractive index concludes to $n_{\text{eff}} \approx 1.41$, see Equation 3.1. Then, the 0.75 cm distance of the reciprocal lattice peaks in Figure 5.2 b) deduce to $\sim$7111 nm. This resembles the periodicity of the hyperuniform data set and can also seen from SEM micrographs, proving the reliability of the setup. Originally, a periodicity of 7.1 µm was programmed, showing almost not shrinkage and but a very good sample quality.

For the $s = 7.38\,\text{cm}$ as shown in Figure 5.2 c) and $n_{\text{eff}} \approx 1.54$, a lattice plane distance of $d = \sim 878\,\text{nm}$ results. Surprisingly, this is much larger than the anticipated l_{char} of 611 nm. Note that this sample was fabricated with a larger laser power and additionally was not developed yet. A large filling fraction is thus expected and negligible shrinkage. Moreover, the characteristic length as defined by the distance of neighbouring nodes is not necessarily the effective characteristic length. The effective characteristic length

might better be defined by the average distance of the interfaces between high and low refractive index regions, as this is where the waves are reflected, and eventually causing the interference. The effective characteristic length stands thus in relation to the linewidth.

Future research might clarify the relation between effective characteristic length and linewidth. Then, with the periodicity of the dataset, the shrinkage can be deduced. With that, the characteristic length should be known, and by the discrepancy to the effectively measured characteristic length, the linewidth could be deduced. The "circle of isotropy" is smeared out, however, and its radius is difficult to obtain properly. The pincushion effect needs to be considered. Compared to the Fourier images obtained from SEM micrographs, the diffraction pattern allows for a better conclusion to characteristic lengths, is non-destructive and additionally much more convenient. Also, the inside of the sample is investigated automatically; low quality samples lead to low quality or implausible diffraction patterns, as found experimentally.

5.1.1. Further Development

A quantitative error discussion is omitted here, as the whole experiment needs to be developed further. Especially quantifying the distances on screen needs to be improved. Currently, 5 cm marks at the border of the screen allow for conversion of pixel-distance to real distance. These marks are most likely distorted by the camera. Other errors naturally originate in imperfections of the setup distances. Also, the beam displacement can be substantial, especially for large angles, as the glass substrate is quite thick with $\sim$0.5 mm.

The setup could be improved by replacing the screen with a bare CCD-Chip. Outer influences are then minimised. Utilising a laser pointer, a handheld device can be imagined, for convenient use in the laboratory. A rotatable sample holder would allow investigation of the influence of the elongation in z on isotropy. The rotation, however, is limited by the glass substrate the sample is attached to. Additionally, the decoupling process is more complicated.

5.2. Transmittance Spectroscopy

A key experiment in this thesis is the spectroscopy experiment. The goal is to fabricate a sample that shows reduced or even extinguished transmittance for a certain range of frequencies. The setup as developed by Knappe and Ropers [29, 30] was improved therefore. A main issue was the irreproducibility of the spectra, which had unknown origin. By introducing a CCD camera in reflection direction, a different sample holder and placing the diode on a stage, the spectra are now stable. The sample is now placed on a motorised stage, for convenience and to be able to measure a reference spectrum without touching the setup. Additionally, the controlling software in *phython* was rewritten. Amongst other improvements, it is now possible to monitor the measurement live. However, the main functionality is still the same. A sketch of the new setup can be seen in Figure 5.4. In the following, the key elements and their specifications are listed. Lenses where used

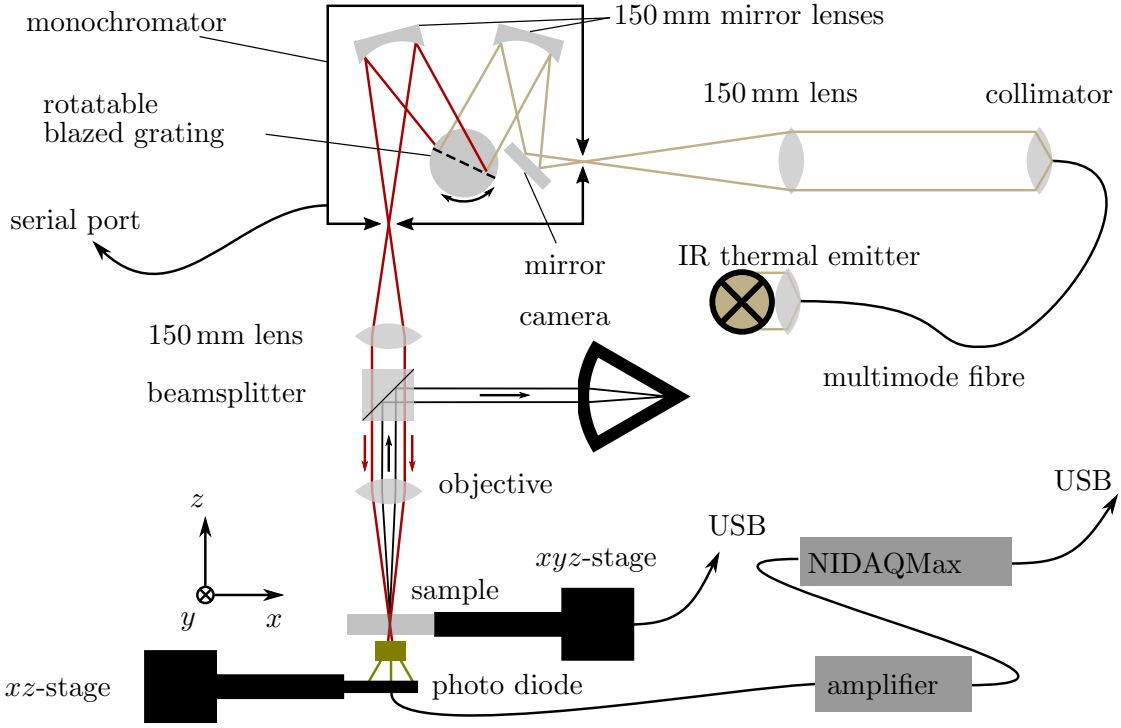

Figure 5.4.: Sketch of the setup of the transmittance measurement. The key elements are the thermal light source, monochromator, objective and photo diode. The camera in reflection direction helps to focus the light onto the sample reliably. A detailed explanation of the elements and the measurement procedure is given in the text.

that have little chromatic aberration in the near infrared, as this is the targeted wavelength of a reduced transmittance. The stabilised infrared thermal light source *Thorlabs SLS202/M* is used, which emits a spectrum of light with wavelength 400 nm to 5500 nm, with peak emittance at 1500 [97]. The light is focused into the commercially available *Princeton Instruments SpectraPro-2150i* monochromator [98]. It essentially consists of a blazed grating that sits on a rotatable stage. By defining the angle of the stage, a wavelength can be selected. For the path of rays, please refer to Figure 5.4. The divergent light is collimated and with a standard 50×, $NA = 0.45$ microscope objective (*Nikon L Plan SLWD*) focused on the sample. For a thorough discussion on focus shape and size of the objective it is referred to Knappe [30]. To capture light reflected from the sample, a beamsplitter is introduced that guides this light on a standard CCD-chip. The intensity of the light transmitted by the sample is transferred to a current with a photo diode. Two diodes where used in this thesis, a *InGaAs G8370* photo diode, sensitive in the spectral region 900 nm to 1700 nm, with a circular photoactive area of diameter 2 mm [99] and a *InGaAs FD10D* photo diode, sensitive in a spectral region from 800 nm to 2600 nm [100] with a circular photoactive area of diameter 1 mm. The diodes signal is amplified, read out with a National Instruments Data acquisition device and the value

is recorded.

To measure a spectrum, the focus of the objective needs to be positioned on the sample. Thus, the monochromator is set to full transmittance. The camera in reflection direction makes it possible to directly monitor the alignment process. Care has to be taken that the focus of the image is at the same position where the light is focused to. This depends on the alignment of the beamsplitter. Next, controlled by the software, the monochromator is set to the desired wavelength. The transmitted intensity is recorded, and another wavelength is approached, until the complete desired spectral range is sampled. This gives the absolute *transmitted intensity*. The motorised stage drives the sample out of the focus, and data of only the glass substrate is taken. This is the *reference intensity*. The actual quantity of interest is the relative *transmittance*[1] T. With that, characteristic spectra of the individual optical elements are divided out. An example spectrum of the glass substrate is given in Figure 5.5. The calibration of the setup was ensured by a 1510 nm band pass, similar as done in [30]. In order to reduce the incident angle, pinholes or slit apertures can be placed in the beam,which will be interesting when examining periodic structures.

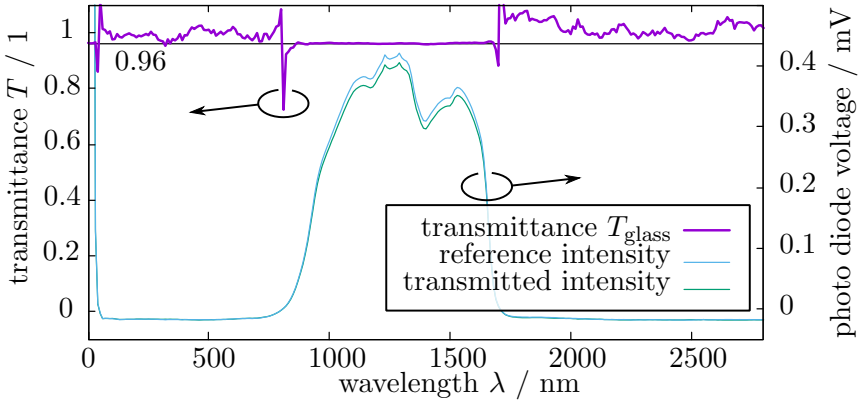

Figure 5.5.: Example measurement of the glass substrate. By dividing the transmitted intensity by the reference intensity, which is measured without the object of interest in the beam, the setup transmittance is compensated. $T_{glass} \approx 96\,\%$ transmittance is typical for quartz glass and can as well be deduced from Fresnell's Equation 3.3. Strong noise is apparent for regions where little intensity measured, as the dicision is sensitive for values fluctuating about 0. The active region of the G8370 photo diode from 900 nm to 1700 nm is clearly seen, in compliance with [99]. The negative voltage recorded for low intensities results from some idling current in the amplifier system and is not distracting.

Measurements taken with the G8370 diode mostly failed to reproduce with the FD10D diode for measurements of the periodic woodpile structure. This may be caused by different geometry due to the smaller photoactive area and a greater distance of the area to the sample, due to the different housing of the diodes. A sketch of the geometry can

[1] The word *transmission* usually refers to the transmitted field amplitude, whereas *transmittance* to the transmitted intensity.

be found in Figure 5.6. The spectrum is not as good to reproduce with the smaller diode, as it greatly seems to depend on the diodes position relative to the focus. Knappe found similar results with the setup [30]. However, the present setup could be improved in the sense that the measurement with the G8370 diode is stable well enough. One notable difference to the old setup is that an accurate positioning of the diode can be done with a second xyz-stage.

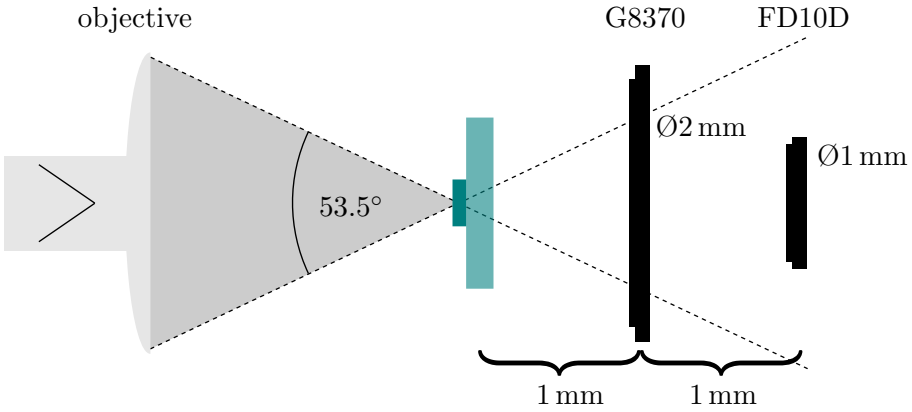

Figure 5.6.: Sketch on the different geometries arising for different photo diodes issue. The large diode tends to capture all light, whereas much light passes the smaller one. A similar issue was discussed in [30].

5.2.1. Outlook

Instead of using a monochromator, the transmitted light could be directly coupled into a spectrometer. The generation of the spectrum would take place much more quickly, which made the process less prone to error. Such a spectrometer in reflectance would allow to deduce for absorbed or light scattered away. For a photonic band gap, the reflectance should increase as the transmission decreases. The occurrence of a photonic band gap could be stated with greater confidence.

Furthermore, the monochromator has been found to leak visible light if set to near infrared wavelengths. This behaviour is attributed to an overlap of higher diffraction orders of the blazed grating used in the monochromator. It is not fatal for photodiodes sensitive in a small spectral ranges, but needs to be kept in mind once larger ranges are probed and could be overcome by introducing high-pass filters.

As has been found, the position of the diode relative to the objective is critical. This, however, is quite difficult to align with the current setup, as the diodes position cannot be monitored easily. Due to the large size of the photoactive area, the read out current is insensitive to displacements of the focused probing light. A camera instead of a single photo diode would thus be favourable, also to measure the spatial distribution of the transmittance. This could reveal further properties.

A tunable laser as a light source combined with this camera, the scattering experiment and the spectrometer setup could be combined. It would be largely interesting to monitor

the transmittance spatially resolved. How does the light propagate near a photonic band gap? How does the single scattering diffraction pattern look in the region of the gap? By infiltrating the sample with a refractive index liquid, the diffraction pattern could also be recorded, wavelength resolved. Single and multiple scattering could directly be compared and reveal insight on the mechanisms of the gap formation, as they are influenced by Bragg- and Mie-resonances, respectively.

5.3. Keratin Pattern Extraction

As pointed out in the theory part, there exists non-iridescent structural colour feather barbs of various birds. They originate from keratin formations that resemble the theoretical hyperuniform point pattern, decorated with cylinders. This indicates that at least a band stop exists and gives motivation for the pursue of creating a photonic band gap with a low refractive index material. The question thus is: How to extract the point pattern from the feather barbs? The full three dimensional information of the keratin structure is needed. Several methods already exist to extract volumetric information from biological tissue. Medical imaging is actually a large and growing field. However, usually it is operated on much larger length scales. The delicate structure of the feather barbs makes the task of extracting the structure quite challenging. Once the data is obtained, well known image processing techniques from medical imaging are adaptable and applicable.

The task described here was done by Shawkey *et. al.* [39] using electron tomography. They successfully predicted the colour of a feather barb from the refractive index and a 3D Fourier analysis of the keratin structure. The structure in a $(1024\,\mathrm{nm})^3$ box was reconstructed and analysed. However, a tomographic error elongates features in the z-direction. In their conclusion they suggested the much more intuitive method of ultra-thin serial section reconstruction with a focused ion beam (FIB) and scanning electron microscopy (SEM). The high resolution needed is not a problem for modern SEM which typically have around 1 nm to 2 nm resolution. Still challenging is the slice thickness, which should lead to a z-distortion as well. With a `Zeiss CrossBeam 1540XB` the facilities are present and this method was tried in this work, described in the following. The description of the functionality of a FIB and SEM shall be omitted here, instead it is referred to the wide range in literature, e.g. [101, 102] and citations.

5.3.1. Imaging

Utilizing the focused ion beam (FIB), layers of feather barbs where repeatedly removed while scanning electron microscope (SEM) images were taken after each removed layer. A sketch of the process and the associated geometry is given in Figure 5.7. This process results in three dimensional data which is then further processed. There are many adjustments possible and needed in order to obtain good image quality and especially slicing quality. Many effects and settings have to be attended to, from simple charging effects tackled by sputtering gold on the sample over how to properly align SEM and

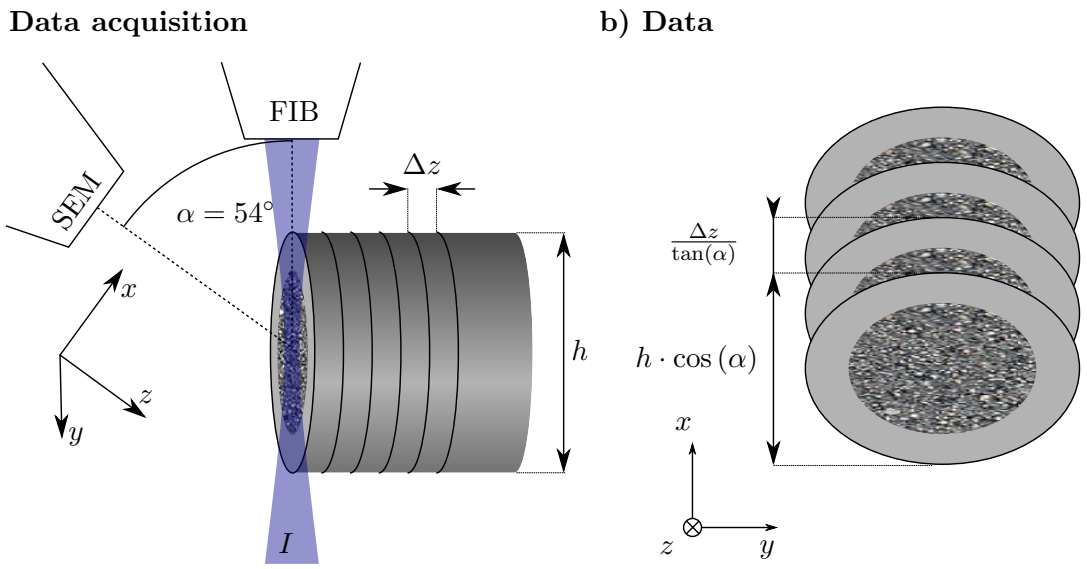

Figure 5.7.: Sketch and geometric definitions of the method to obtain slices of feather barb. a) shows how the sample is arranged within the vacuum chamber of SEM and FIB. The FIB-current I (shown blue) consists of heavy gallium atoms that are focused at the area of the sample were material removal is desired. Due to the momentum and energy of the ions, material is sputtered into the vacuum and removed. By guiding the beam along y, slices are removed. Then SEM pictures are drawn in. The resulting stack of images is shown in b) along with the height compression and shift along x due to the geometric arrangement.

FIB. Crucial parameters are e.g. the imaging and slicing currents. These were optimised with support of Matthias Hagner [103].

As the pure sample consists of keratin and air (respectively vacuum), a SEM image will always contain depth information and a slice will never be truly two dimensional. This makes image processing quite challenging and the idea of filling the voids with a high contrast material arises. The sol-gel process as used in [40] was adapted. In short, the precursor tetraethyl orthosilicate (TEOS, $C_8H_{20}O_4Si$, reagent grade, 98 %) is dissolved in Ethanol (C_2H_6O, 99.8 % purity) together with a weak acidic catalyst (HCl (aq), 0.1 mol l^{-1}) with a ratio of 1 : 50 : 1. As the main solvent is dried, this solution (sol) solidifies to a gel, hence it is called *sol-gel process*. Chemically, a hydrolysis reaction takes place so that silica (SiO_2) is obtained, which then can form a network of siloxane (Si−O−Si) bonds. In non-chemist words, dissolved glass molecules are condensed to form glass. The solution is subsequently dropped on a feather barb and dried, until the vanished structural colour indicates a complete filling of the voids with SiO_2. As silicon has the atom number 14, which is more than twice the atom number of carbon (6) being the main ingredient of the keratin feather barbs, the SiO_2 appears much brighter in the final SEM image. Furthermore, the depth information within a single slice is suppressed as the electrons cannot penetrate through the silicon dioxide. Actual images are shown

in Figure 5.8. In principle, the same process is possible with another precursor to fill the voids with titan dioxide (TiO_2, atom number of Ti: 22), leading to even higher contrast.

Another effect has to be tackled: curtaining is the most influential effect on data quality. Curtaining happens during the slicing with the FIB-current, shown in the infiltrated image, Figure 5.8. Material removal is most effective if the beam hits a surface perpendicularly. In reality, the feather barbs do not have a smooth surface at all. At certain areas material is removed more efficiently than at others. To make matters worse, different materials are also removed with different efficiency, dependant on the internal molecular bonds. As the materials are more or less randomly distributed in and above the barb, more curtaining takes place. The curtaining is thus lower for the pure sample. A lot depends on the actual sample preparation for this matter. Until now, no golden way has been found to eliminate curtaining and further research needs to be done. It has been found that it helps to prepare a slicing plane with FIB-currents from high to low, instead of using a low cutting current right away. This also saves time, as the whole process takes e.g. 12 h for $\sim$ 200 slices, giving $\sim$5 µm depth. The

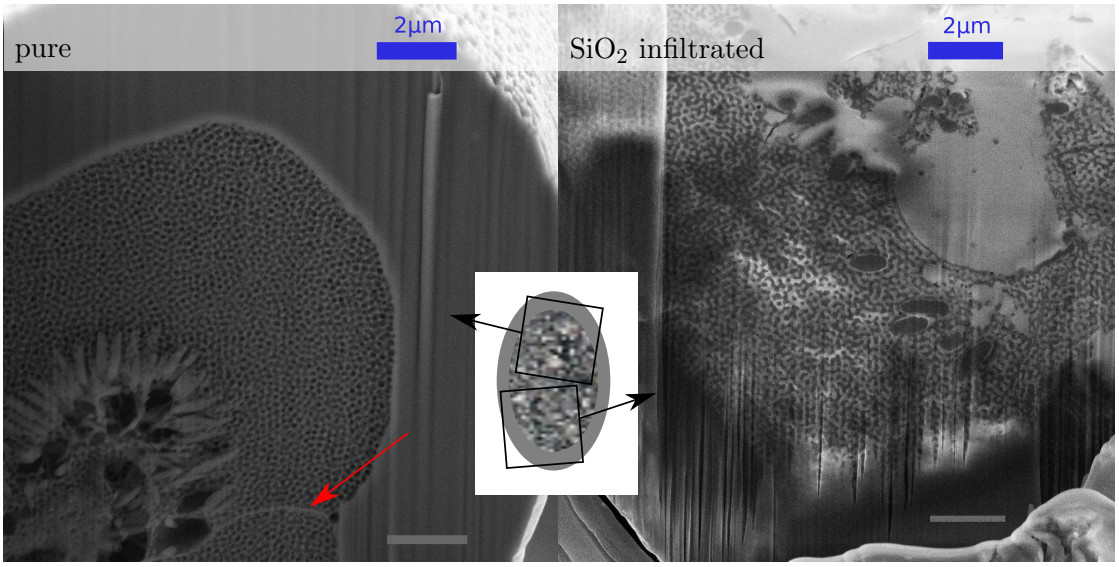

Figure 5.8.: Effects of the SiO_2 infiltration process on image quality. Left is shown the pure feather barb of a *Agapornis roseicollis*, right a barb infiltrated with SiO_2. Depth information is successfully suppressed in the infiltrated sample. The price for better contrast is a more pronounced curtaining effect as well as charging effects. Note that the contrast flipped: in the pure sample, keratin shows bright whereas dark in the infiltrated image. The middle part of feather barb has large voids, which get filled with SiO_2. A keratinocyte boundary can be seen left bottom right, marked with the red arrow.

contrast is greatly enhanced and depth information almost entirely removed. However, the material hardness is more different, leading to more curtaining effects. That is why infiltration of TiO_2 (atom number of Ti: 22) was not done yet.

Alternative structure analysis might be done by X-Ray tomography, possibly in a collaboration with Ullrich Steiner (Adolphe Merkle Institute in Fribourg, Switzerland). The resultant data could then as well be examined with the data processing and point pattern extraction explained in the following.

5.3.2. Image Processing

The image processing is done using the open source software KNIME [104] with the image processing plugin. In Figure 5.9 the procedure [105] is depicted at a two dimensional example that can almost directly be transferred to three dimensions. It follows a further explanation of the filters and why they were used. Here, points of the extracted point pattern shall be dubbed "nodes" to not confuse with points represented by pixels. Connected nodes are called "neighbours".

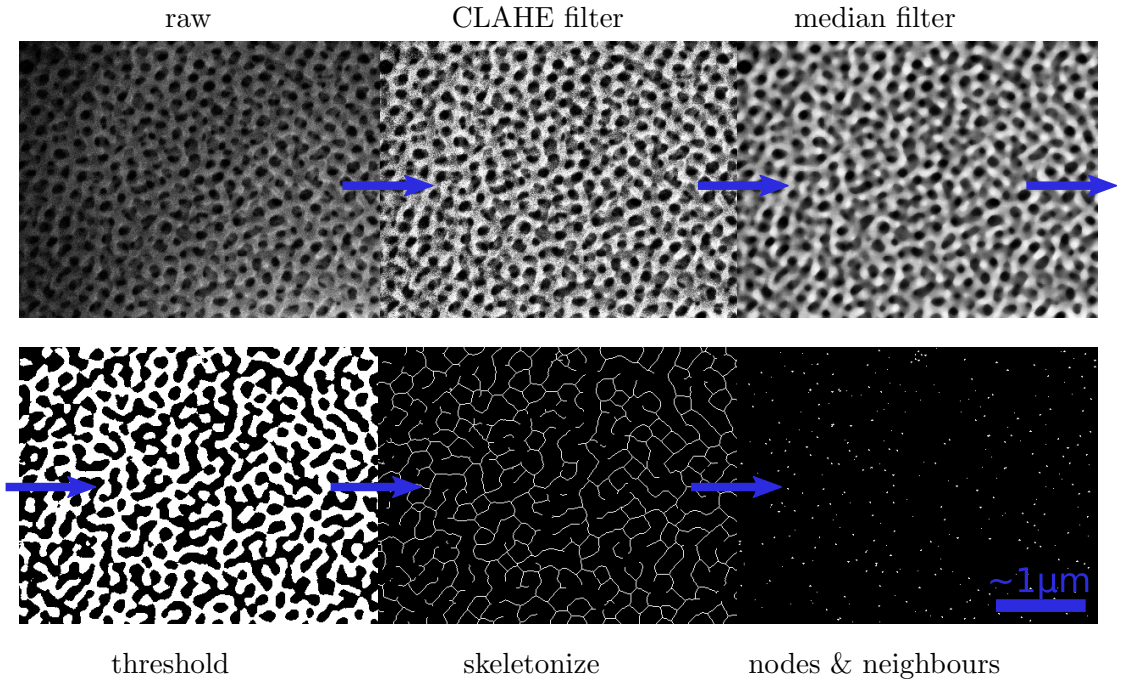

Figure 5.9.: The image processing shown for a two dimensional example. No contrast increasing infiltration was performed on the shown sample. Noise is filtered (top row) to be able to apply a threshold to identify keratin regions. Those regions are then thinned to lines and nodes are identified as the junctions of the thin lines. Below, the steps are described in detail. The procedure is applicable for three dimensions in the same manner, only that an additional smoothing of the thresholded image is done.

Aligning: In the three dimensional case, not shown in Figure 5.9, prior to any filtering the images of the slices taken with the SEM need to be aligned as there is always some

drift in x, y direction having diverse origin. Therefore, a cross-correlation approach is used on a filter prepared from the original images giving the vector with which the slices are shifted relative to each other. The exact shape and procedure of the filter depends strongly on the data. Naturally, parts of the image that remain the same during slicing are used, for example the outer barb structure is a suitable area. The KNIME implementation was used to do the cross-correlation as well as finding a filter.

CLAHE Filter: To begin with, large scale noise is filtered out. To do so, the images intensity histogram is equalised. However, a standard equalisation of the histogram, where the cumulative histogram of the whole image is linearised over the largest intensity range the particular image type allows (Byte Type, thus $2^8 = 256$ distinguishable intensities in Figure 5.9) is not sufficient in this case. Instead, the **C**ontrast **L**imited **A**daptive **H**istogram **E**qualization (CLAHE) technique was applied. CLAHE is a variant of the adaptive histogram equalisation (AHE) technique that does not overamplify noise as much. AHE does the same as standard histogram equalisation, but transforms each pixel based on the histogram of the pixels neighbourhood instead of the histogram of the whole image. This improves results if pixel values are not uniformly distributed in the image, as is the case for a gradient background, e.g. seen in Figure 5.9, first image. For the CLAHE technique, the histogram of the neighbourhood is modified to limit the transformation function, resulting in reduced noise amplification. Details can be found in [106]. The filtered image shows a more uniform background, see Figure 5.9, second image. In other words, long range noise is removed. The ImageJ implementation was used in KNIME.

Median Filter: The next filter tackles small range noise. Around each pixel a 3^d pixel wide rectangular window is laid. The new pixel value is the median pixel value of the window. This filter has the important property to preserve edges [107] in our case, as can be seen in image three of Figure 5.9. The implementation of KNIME was used.

Threshold: Now that noise is removed, the keratin can be identified by applying a threshold, where each pixel with a value above the threshold value is thought to be keratin (shown white in Figure 5.9), while the other pixels are air. The threshold value is empirically chosen around the median value of the image. By counting the keratin pixels and comparing to the total number of pixels, the filling fraction can be deduced. With that, the effective refractive index can be calculated, see Equation 3.1. The KNIME image processing implementation was used.

Morphological Operations: Not shown in Figure 5.9 are morphological image operations such as erosion and dilation or successive iterations of those (called then opening and closing). They are applied to the three dimensional data. Roughly speaking, a ball of radius r is rolled around the surface of a white area, and a new, larger surface is defined by the midpoint of the ball. If the ball rolls on the outside of the white area, the procedure is called dilatation and the white areas grow, the inverse case where the ball

is rolled on the inside is called erosion and the white area shrinks. An erosion followed by a dilatation is called opening, small (how small depends on r) white areas vanish but large enough areas stay same in size, with spikes on the surface being smoothed. The opposite, a dilatation followed by a erosion is called closing as white areas being close to each other are connected and small black spots within white areas vanish.

For each set of data this procedure is adapted until the skeletonised image shows no artificial loops and junctions. The KNIME image processing implementation was used.

Skeletonise: In the next step, the topological skeleton of the keratin structure is calculated. The skeleton of a binary image are all points that are equidistant to the surface of the volume. A sophisticated algorithm [108] implemented in ImageJ [109] was used.

Extract Nodes: In order to extract nodes from the skeletonised image, an algorithm had to be devised. My solution uses a property of the skeleton: each pixel on a line has exactly two neighbours, pixels on a junction always more. Every pixel having more than two neighbours are thus marked as being on a junction. One junction can consist of several pixels. The geometric centre of gravity of these junction pixels is then interpreted as the position of a node. The positions are then in units of pixels and are converted to physical distances with the resolution factor known from the imaging process. As depicted in Figure 5.10 false positives could be detected. In order to prevent this, morphological dilation is applied on the extracted nodes image (shown red). A sphere of diameter being approximately the rod thickness is used in order to combine those close by nodes. Double nodes show a great effect on the hyperuniformity, length-, neighbour-, and angle distribution of a pattern and are to be prevented therefore. Care has to be taken to not chose a too large diameter or actual nodes would merge.

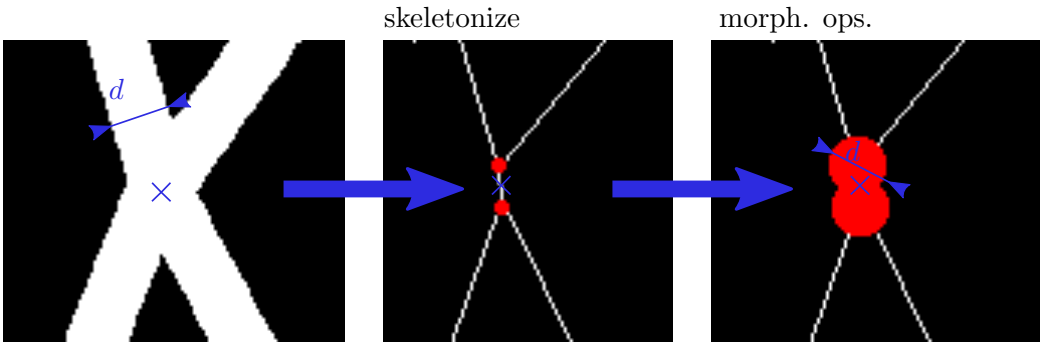

Figure 5.10.: Sketch on the formation of double nodes. Where the thresholded image only shows one node (blue cross), the skeletonized image has two (shown red). To prevent these from disturbing the statistics, morphological dilation with a sphere of diameter d is applied on the nodes image. The centre of gravity of the blown up, merged nodes then matches the original nodes position much better.

Extract Neighbours: To do the (re-)decoration of the pattern correctly, the neighbour information has to be extracted. The algorithm starts at one node and walks along the lines originating from it until another node is hit. This other node is then a neighbour and its position is written out to generate a file of the same format as our collaborators use. This algorithm was developed by myself.

5.3.3. Method Validation

Before this workflow is applied to actual data, its capabilities are validated and tested. The range of application and possible limitations have to be explored. A main feature of interest is how low the resolution can be chosen. In order to extract as many points as possible a large SEM image of the structure needs to be taken. A resolution has to be found, that still allows to distinguish features but also allows for solid statistical evaluation of the extracted pattern.

To do this validation, slices of the theoretical hyperuniform pattern described earlier in section 3.2 and depicted in Figure 3.3 were rendered using the open source software POV-Ray [73] again. The resolution for the rendering given in units of pixels per characteristic length $\mathrm{px}/l_{\mathrm{char}}$ was varied but kept equal for each direction x, y and z. Note that the slices are perpendicular to z and the spacing of the slices gives the z-resolution. Figure 5.11 a) shows sample slices for two different resolutions at $z \approx 0$.

The pattern was then extracted with the above mentioned workflow and results are compared to the original data using the Pointpatterntool described in section 3.1. Scaling and position of the extracted data cuboid was adjusted and the difference vector of each point to the closest original point was taken. These difference vectors are randomly distributed and do not show a distinct direction for all resolutions. The pattern to be compared is then shifted about the centre of gravity of the difference vectors to exclude non-relevant shifting of the pattern. Figure 5.11 a) shows the length distribution of these difference vectors for two tested resolutions. For the lowest resolution a fair amount of difference vectors is half a characteristic length long. This means that some of the extracted points are so far away from the original position that they cannot clearly be associated with the original position but another neighbouring node. This has negative impact on the statistics. The width of the length distribution of neighbouring nodes is affected most by the extraction, whereas hyperuniformity and width of angle distribution are affected the least.

All in all, the method proves to be well applicable, especially to extract the hyperuniformity of a pattern. A resolution around $15\,\mathrm{px}/l_{\mathrm{char}}$ seems a good trade off between large enough image and well enough resolution. The characteristic length can be estimated previously to the extraction, e.g. from a Fourier transform of a SEM image.

a) Difference Vector Distribution

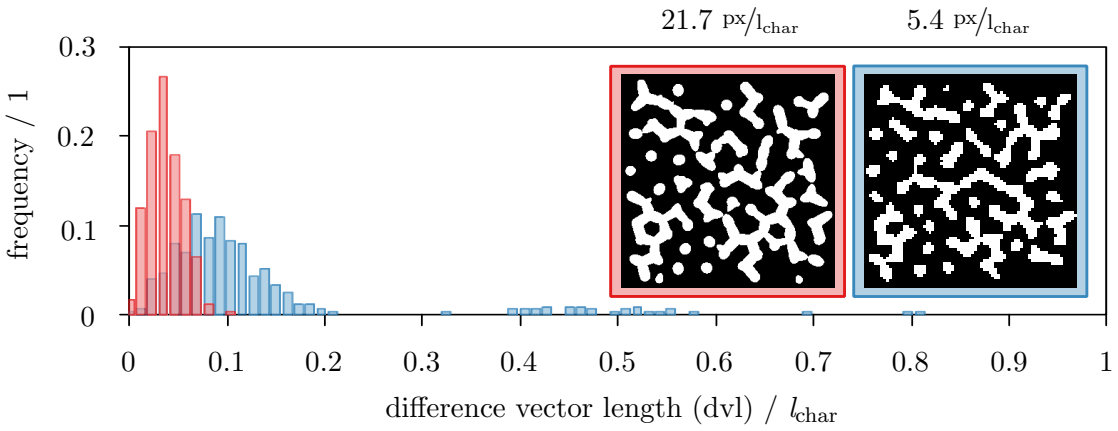

b) Extracted Pattern Statistics

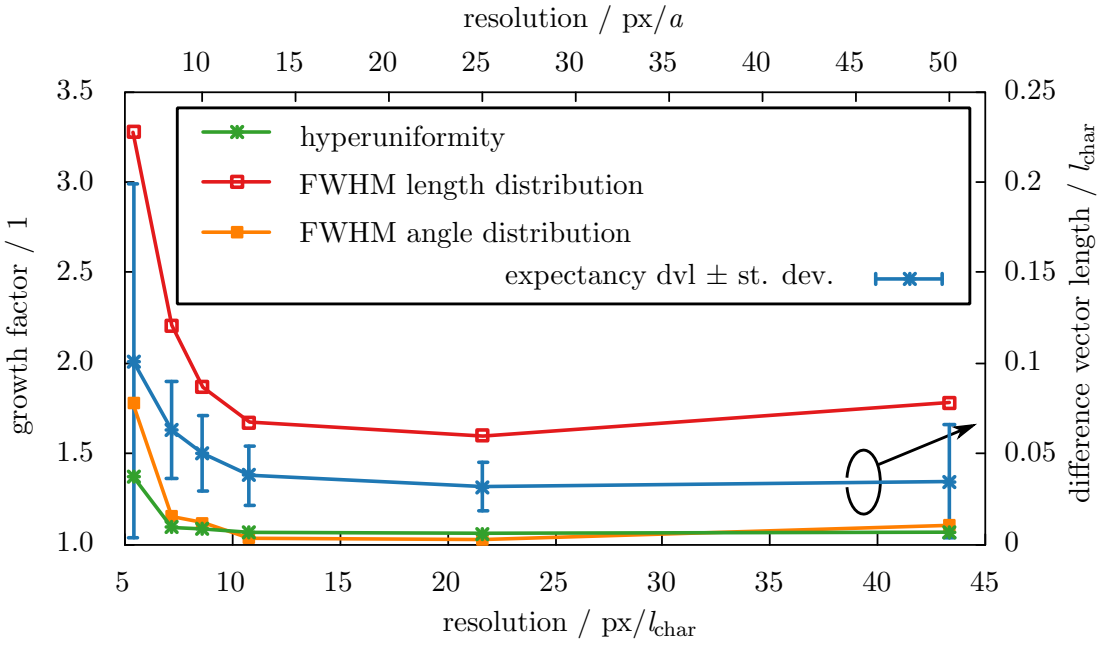

Figure 5.11.: Difference between original and extracted patterns. a) shows the length distribution of the difference vectors for lowest and highest tested resolution along with example slices at $z \approx 0$. Strong "pixelation" can be observed. b) shows the impact of the extraction on the statistics of the patterns as well as the difference vector length (dvl) expectancy and its standard deviation. As expected, the extracted pattern matches the original one for high resolutions. For resolutions lower than $10\,\mathrm{px}/l_{\mathrm{char}}$ the pattern is biased so much that the extraction cannot be trusted anymore. The connecting lines are guides to the eye. The slight increase for the highest resolution is due to artifacts which could be reduced with further fine tuning of the image processing parameters. For the general conclusion this is not relevant, however.

6. Final Results

In this chapter, the methods discussed above are actually utilised. The aim is to fabricate a structure exhibiting a band gap or at least a band stop, meaning reduced transmittance for a selected spectral range. Simulations were performed on different structures. Special emphasis was laid on the investigation of the woodpile structure and structures from the hyperuniform data set. The former is thought to serve as a warrant for the authenticity of the results for the latter. The different simulation methods are compared to each other, and then to actually measured data. Furthermore, the keratin structure of an *Agapornis roseicollis* is examined, and a preliminary glance at results for the extracted pattern is given.

6.1. Pattern Comparison

To begin with, the transmittance through four different structures is calculated with the finite-difference time-domain (FDTD) method. A setup and procedure as explained in section 3.5 is used. Wavelength λ and frequency f of the light are related with $\lambda = {}^{a}/_{f}$. Results are shown in Figure 6.1. Here, high refractive indices of $n = 2.5$ are simulated, as band gaps are found more often in high contrasts materials. The transmittance of a plane wave through a diamond pattern, a hyperuniform pattern and a Poisson pattern is simulated, each decorated with cylindrical rods of radius $r = 0.3\,a$, as well as a woodpile structure with elliptical decoration, with the short half axis being $r = 0.3\,a$. The characteristic length of the hyperuniform structure is $l_{\text{char}} = 0.86\,a$ as for the diamond pattern and similar for the Poisson patter (see section 3.2). The rod distance for the woodpile structure is $g = 1\,a$ and the four-layer distance $c = \sqrt{2} \cdot g$, giving a bcc crystal structure. The structure from the hyperuniform data set and the woodpile structure will be the structures further examined.

The transmittance is relatively noisy for all spectra. This is thought to be an artefact of the simulation. The loss L can be calculated from the transmittance T and reflectance R with $L = 1 - (R + T)$. It emerges, as a finite number of timesteps is calculated and at the terminating time step fields still remain in the structure. Naturally, the loss is higher for higher frequencies, as this light is scattered more frequently. This becomes especially important for high refractive indices and large radii, also because the optical path becomes longer and more time steps need to be calculated. Note however, that refractive index materials free of loss are assumed, excluding absorption as the cause for lost intensity L.

For the periodic woodpile structure, a significantly reduced transmittance can be seen for several spectral ranges, as well as for the diamond structure. The depth of these dips is furthermore large, over four to five orders of magnitude. Bragg scattering together

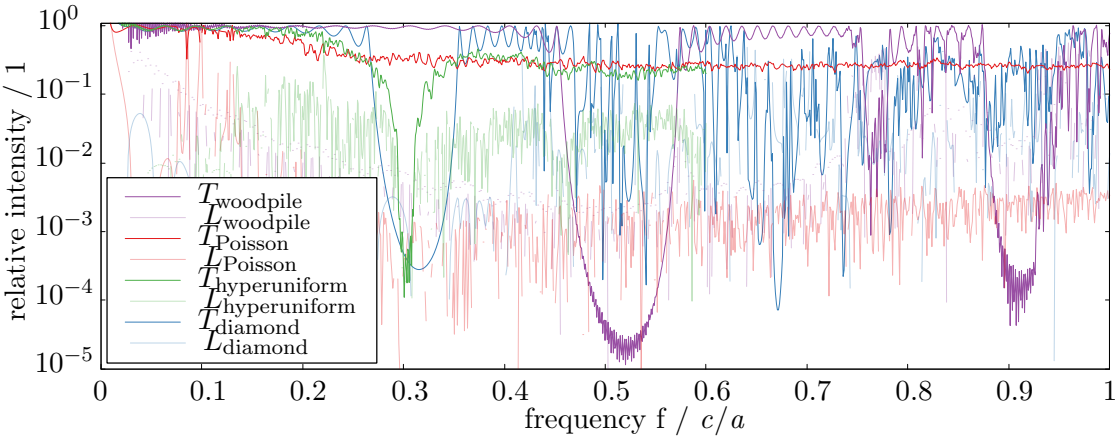

Figure 6.1.: Comparison of the transmittance T of four different structures: the woodpile (purple), the Poisson (red), the hyperuniform (green) and the diamond (blue) structure. Transmittance and loss is plotted over frequency. Note the half logarithmic representation. The rod radius is $r = 0.3\,a$ and its refractive index is $n = 2.5$. For the woodpile structure, an elliptical decoration with r being the short half axis was calculated. Presumably for its lower filling fraction the first dip in transmittance is at larger frequencies than for the other patterns. Substantially reduced transmittance is evident for all patterns expect for the Poisson pattern, stressing the importance of the arrangement of the underlying point pattern.

witch Mie resonances can held responsible for the reduced transmittance. This strongly indicates an origin from band theory. Also, higher order dips emerge, caused by the long range order. For the diamond case, this results in a rather chaotic transmittance behaviour for large frequencies.

For the hyperuniform pattern, a reduced transmittance can be seen as well. The dip is not as deep and wide as for the woodpile structure, which could result from the lack of Bragg scattering. Mie resonances could be held responsible for the reduced transmittance. The different filling fractions could explain the difference in dip position. Still, the short range order is apparently necessary for the Mie-resonances not the be destroyed, as the equally decorated Poisson pattern does not posses any characteristic reduced transmittance.

Also, the different scattering regimes can well be seen from these simulations. An electromagnetic plane wave with low frequencies is influenced only very little by the structure, behaving like in a homogeneous materials. When the wavelength reaches about four times the characteristic length, the Mie-regime is entered and the band gap formed. For shorter wavelengths, this results in complicated scattering and thus seemingly chaotic transmittance patterns. For the large frequency limes, the geometric optics would be reached.

From these findings it can be seen, that a reduced transmittance over more than three orders of magnitude can safely be accounted to a band gap. To identify the origin of the reduced transmittance with greater confidence, the field distribution of frequencies

at the band edge might be concluded to from future simulations, as done in [18] for two dimensions. With respect to building waveguides in such photonic band gap materials, the investigation of the penetration depth is worthwhile. Then, a minimal possible guide separation can be estimated, under which coupling takes place.

6.2. Woodpile Structure

The woodpile structure was both analysed with simulations as well as fabricated with two-photon-absorption direct laser writing (DLW). The resultant structures where then characterised and measured transmittance spectra compared to the simulations. In the theory section, the structures geometry was explained, see Figure 2.11. The woodpile structure is examined, as it is well understood and serves as a test structure to verify simulations and measurements.

6.2.1. Woodpile Dispersion Relation

The complete dispersion relation for the woodpile structure was calculated using the plane wave expansion method described in section 3.4. If a frequency range is found where no wave vector is possible, a band gap is present and propagation of any electromagnetic wave within this frequency regime is prohibited. An elliptical rod cross section was used to mimic the experimental conditions, with the small half axis $r = 0.3\,a$, $g = 1\,a$ being the rod distance and $c = \sqrt{2} \cdot g$ the distance of four layers. The rods are elongated in stacking direction z, as schematically drawn in Figure 2.11. Two different refractive indices of the rods $n_{\text{low}} = 1.54$ and $n_{\text{high}} = 3.00$ were compared, where the former is close to the refractive index of the photo resist for the DLW fabrication technique. The first 20 bands were calculated, leading to different upper frequencies. Results are shown in Figure 6.2 and Figure 6.3, respectively. a) shows the band structure along a path on the Brillouin zone (BZ), as shown in the inset. b) shows the density of states (DOS), calculated from the iso-frequency surfaces. c) to f) show the three dimensional dispersion relations by depicting the iso-frequency surfaces for four different frequencies.

For the woodpile structure with the low refractive index contrast of $\Delta n = 0.54$ no band gap is apparent. The dispersion relation is clearly linear for low frequencies $f < 0.7\,c/a$. Bragg scattering occurs once the iso-frequency surface reaches the Bragg planes that define the BZ. Pockets open from dispersion relation of neighbouring reciprocal lattice points, depicted in Figure 6.2, d). For a small frequency interval, this results in forbidden wave vectors with small angle with respect to z. Propagation along z, however, should still be possible, as surface normals in this direction do exist, in the portion of the pockets close to the k_x-k_y-plane, given the right excitation is provided. Due to the elliptical rod cross section, some symmetry of the diamond is broken and $\boldsymbol{k}$-vectors parallel to x and y are allowed. The fourth band depicted in Figure 6.2, e) was investigated by [78] for negative refraction. The similar shape gives confidence to the present method. For larger frequencies, the dispersion relation becomes increasingly complex. Waves propagating in the medium can scatter at imperfections. In the large frequency range, the iso-frequency

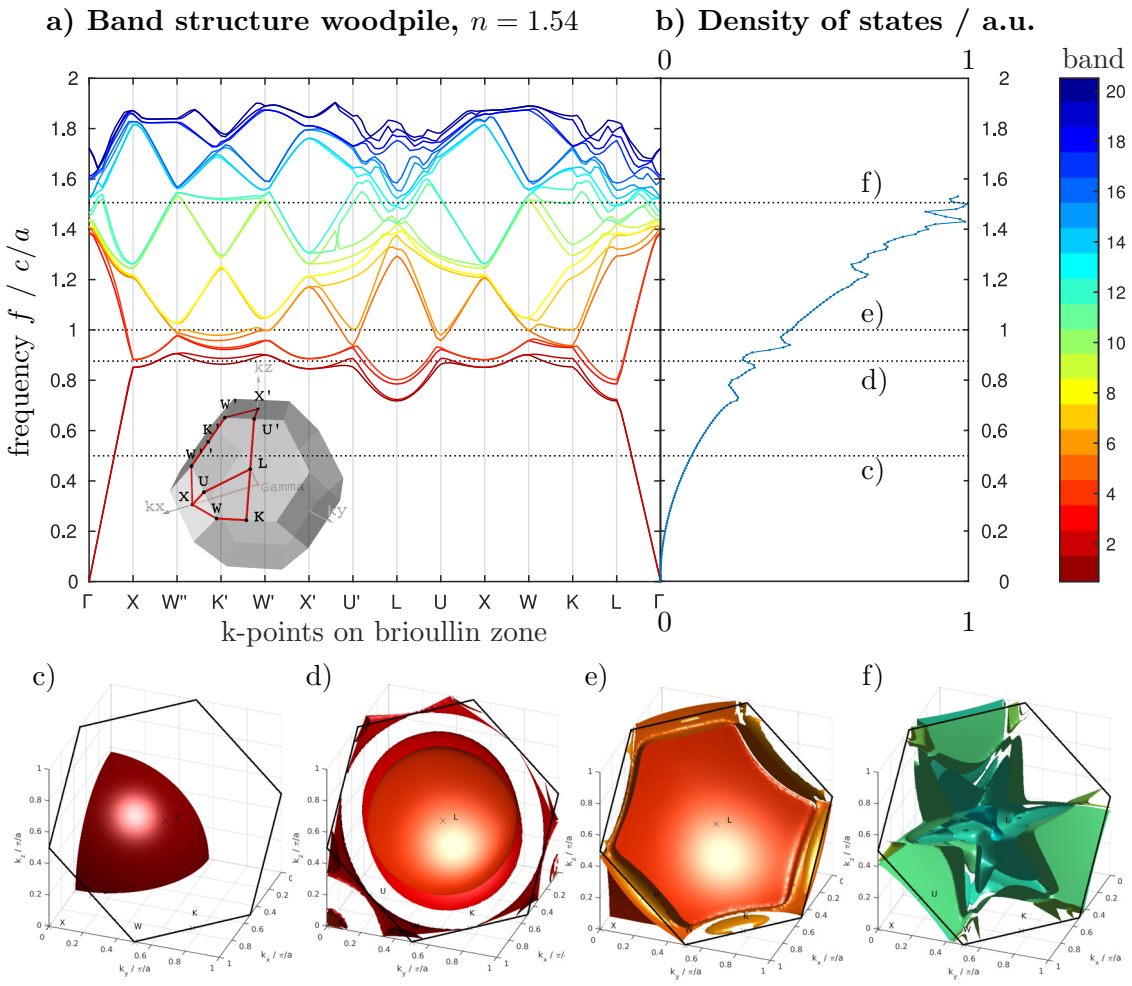

Figure 6.2.: The dispersion relation of a woodpile structure with refractive index of the rods $n_{\text{low}} = 1.54$. a) shows the band structure along the path of high symmetry as shown in the inset. b) shows the DOS, calculated from the iso-frequency surfaces shown in c)-f). A detailed discussion can be found in the text.

surfaces are quite dense, which could support scattering, as little changes in momentum are allowed for the same energy.

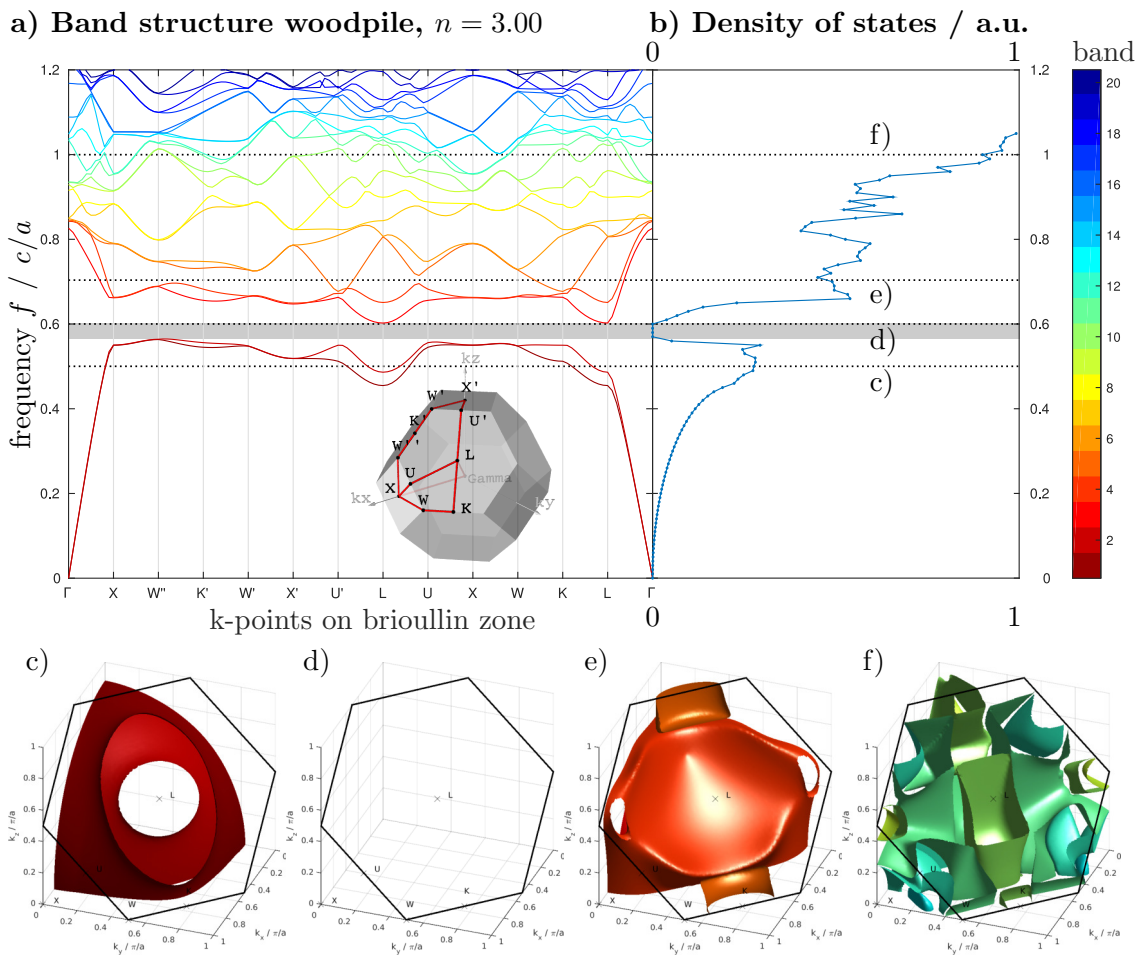

Figure 6.3.: The dispersion relation of a woodpile structure with refractive index of the rods $n_{\text{high}} = 3.00$. a) shows the band structure along the path of high symmetry as shown in the inset. The frequency range where a band gap opens up is shown in grey. b) shows the DOS, calculated from the iso-frequency surfaces shown in c)-f). A detailed discussion can be found in the text.

In principle, the same discussion holds for the higher refractive index contrast of $\Delta n = 2.00$, shown in Figure 6.3. The gradient of the dispersion relation is lower and Bragg scattering occurs thus at lower frequencies. Also, the effects of the elliptical decoration is evident for lower frequencies. This is due to the slower light propagation of light in optically dense media, and the density in this case is higher along z. The band gap is obvious, where no wave vector exists for a range of frequencies. The DOS vanishes for a range of $\Delta f = 0.03$ around a centre frequency of $f_0 = 0.585\, c/a$, giving a width to centre ratio of $^{\Delta}f/f_0 \approx 5\,\%$. From the band structure, the anisotropy of band gap is

apparent, as its width changes dependant on the position on the BZ. The gap is widest around the L-point. The pockets as seen for the low refractive index contrast woodpile can not be seen, because the surfaces are distorted too much for higher frequencies.

In reality, at some stage the wave fronts become so complicated that no unique wave vector $\boldsymbol{k}$ can be associated to a wave. Also, the scattering makes the association of a wave to a wave vector difficult. For lower frequencies, the linear approximation is well possible. Also notable is the occurrence of pairs of bands, which should stem from the two scatterers in the unit cell, see section 3.4. The band gap opens up between the second and third band. The first and second bands can be considered as the dielectric bands, the higher ones as the air bands. This is also indicated by the field distribution (not presented here). One can conclude that the nearly free photon theory is applicable for low frequencies and low refractive indices, whereas the Mie resonances play a greater role for higher frequencies and higher refractive index contrasts.

6.2.2. Simulated Woodpile Transmittance

It would be interesting to find a method to calculate the transmittance from the DOS. With that, experiment and simulation could be compared better. Due to the lack of such a method, the finite-difference time-domain (FDTD) method is applied in the same manner as in section 6.1, for the woodpile structure, with refractive indices $n_{\text{low}} = 1.50$ and $n_{\text{high}} = 3.00$. Resultant transmittance T and loss L are shown in Figure 6.4.

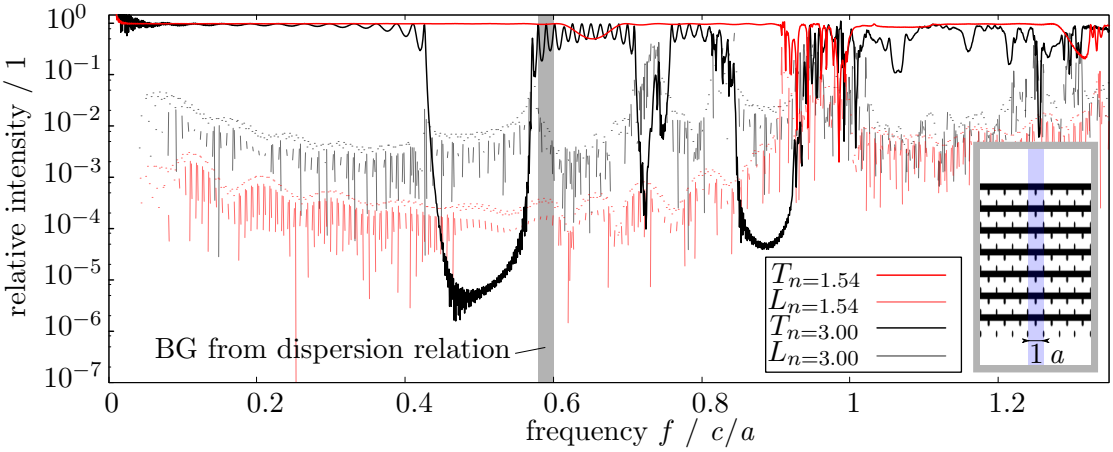

Figure 6.4.: Transmittance through the woodpile structure, simulated with the FDTD method, for two different refractive indices $n_{\text{low}} = 1.50$ and $n_{\text{high}} = 3.00$ of the rods. The insets show a cut at $x = 0$ through the shaded unit cell, periodically continued. Shown black is the higher refractive index area, white corresponds to $n = 1$.

The low refractive index woodpile does not show a significantly reduced transmittance from this simulation. The dip at around $0.65\,c/a$ is not evident from the plane wave expansion method. The reduced transmittance at $0.95\,c/a$ could be explained with the distorted density of states at that frequency, see Figure 6.2, b).

The band gap for the woodpile with large refractive index contrast results in a reduced transmittance at lower frequencies. This could be attributed to the effect of Mie resonances. Florescu *et. al.* [53] pointed out, that the Mie resonances for the 2D case occur at the lower band edge. This would fit to the present simulations, being 3D simulation. The second dip in transmittance does not stem from a real band gap, but could be related to the reduced density of states at $f \approx 0.9\, c/a$, see Figure 6.3, b), being higher order destructive interferences.

Concluding on can say that with the FDTD simulation, reduced transmittance can be detected more easily than by calculating the dispersion relation. Due to the fact that Maxwell's equations are solved in detail, this method takes more effects into account. However, with the plane wave expansion method, a true band gap can be identified. Both simulations together help to understand the interaction of electromagnetic waves with a structured refractive index material. In the following section, a fabricated woodpile structure by means of DLW is examined.

6.2.3. Woodpile Fabrication and Characterisation

As the woodpile structure consists of long straight rods, the effects of the sample holders moment of inertia are almost negligible during writing. Also, the algorithm uses far higher writing speeds, which gives need for higher laser powers to ensure reasonable power distribution. A minimal possible laser power was found to be 23 %, below which the woodpile structure is too weak to compensate any strain or capillary forces. This results in rods that fall over, see Figure A.1. A well fabricated structure can be seen in Figure 6.5, a) imaged with transmission microscopy. Figure 6.5 b)-d) shown SEM micrographs with different magnifications.

The woodpile structure has the convenient property that its filling fraction is determined by the thickness of its rods. Neglecting any overlap, the filling fraction can be deduced with dividing the line thickness by the line distance. For the sample shown in Figure 6.5, d) with a line width of ∼150 nm this results in $\Phi \approx 15\,\%$.

Only little shrinkage is evident, deduced from the micrographs. Diffraction patterns from these structures are taken and shown in Figure 6.6 a), b). The setup is described in section 5.1. The resultant lengths emphasise the small shrinkage. The pincushion distortion can again well be seen for large Bragg angles, resultant from the coupling out of the sample. Spots closer to the zeroth spot are structurally forbidden [59], but emerge due to the finiteness off the crystal and multiple scattering. From the higher laser power a thicker fabricated line should be expected, less prone to shrinkage. The slightly lower lattice plane distance for higher laser powers is thus thought to be within the error. The effective refractive index should not play a role, as argued in section 5.1. A generally more clear pattern is seen for higher laser powers. This may be due to a smoother polymer to air interface for those higher laser powers.

Finally, after ensuring sample quality and defined geometry, transmittance measurements are performed with the setup described in section 5.2. Clearly, a reduced transmittance is evident, see Figure 6.7. The dips position at $\lambda_0 = (1140 \pm 10)\,\mathrm{nm} \mathrel{\hat{=}} f = 0.88\, c/a$ approximately corresponds to the second "dip" in the FDTD simulation of the woodpile

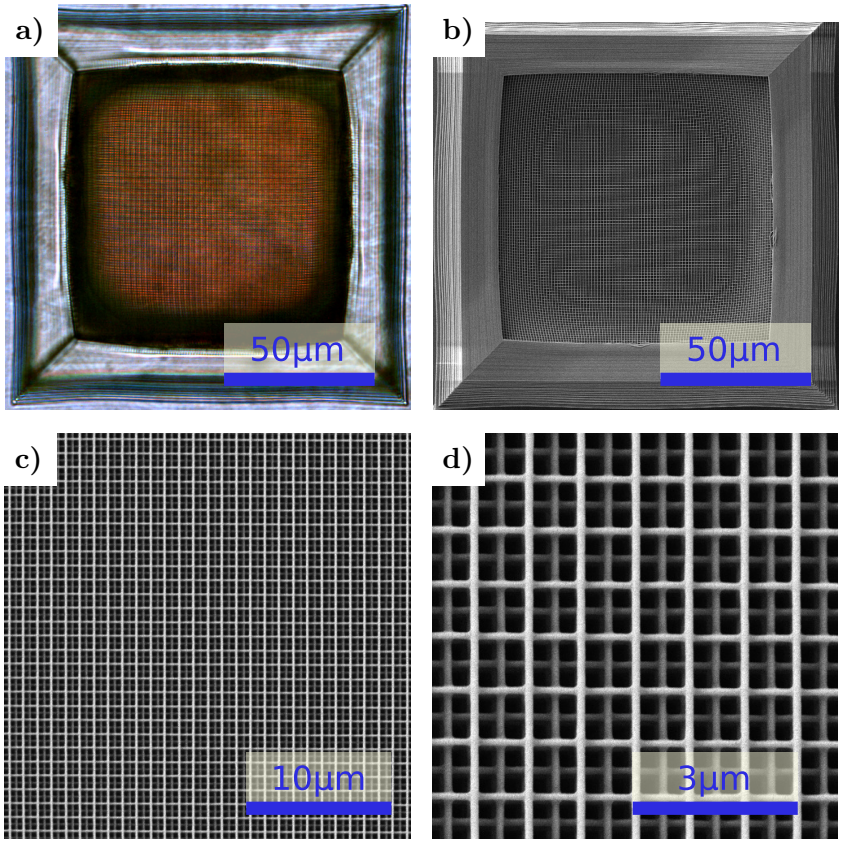

Figure 6.5.: High quality woodpile structure fabricated with 23 % laser power (4.6 mW). It has a programmed footprint of 100^2 µm^2, 15 µm height and line spacing of $g = 1$ µm. a) shows a transmission light micrograph, b) - d) SEM micrographs. The Moiré pattern in b) helps to identify distortions near the supporting walls. As seen from the scale bars, the programmed rod distance of 1 µm is well met. Its height is 15 µm, corresponding to 42 layers of gratings.

with refractive index $n = 1.50$ and approximately similar geometry, Figure 6.4. The error in dip position was approximated from the 10 nm step size the wavelength is tuned with.

From the plane wave expansion method simulations, see Figure 6.2, it became evident that light with a wavevector parallel to z can not couple into the structure. In order to test this hypothesis the incident lights angle where confined with a pinhole. As the resultant dip in transmittance becomes deeper, see Figure 6.7, this hypothesis is affirmed.

Woodpile samples were fabricated with different rod distance but constant layer distance. Varying the layer distance is difficult with the DLW method, as layers do not connect for too large distances. For future research, multiple exposure of a single rod can be tried. Transmittance spectroscopy was done and reduced transmittance dips could be found. Micrographs and transmittance spectra can be found in the appendix Appendix B. For non-fcc structure, the dip in transmittance is largely reduced. In

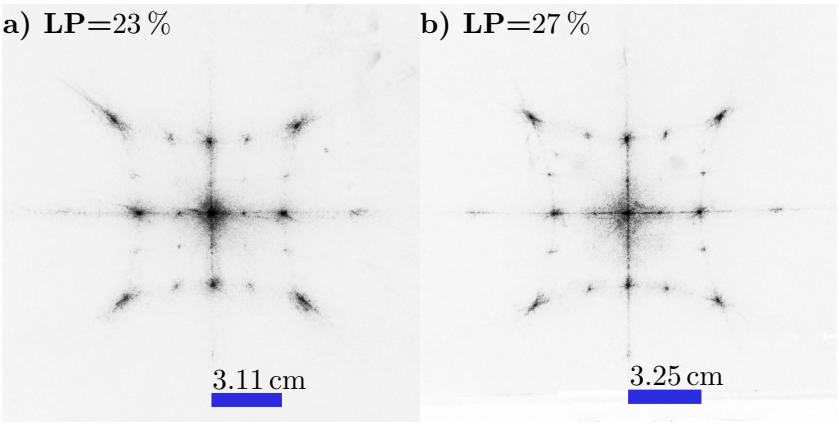

Figure 6.6.: Diffraction pattern of two woodpile structures, fabricated with different laser powers, a) 23 % and b) 27 %. The blue scale bars denote the distance of the first diffraction peak to the zeroth on the screen at $d_{\mathrm{ss}} = 5\,\mathrm{cm}$ from the sample. This results in a lattice plane distance of $d_{\mathrm{LP=23\,\%}} = 975\,\mathrm{nm}$ and $d_{\mathrm{LP=27\,\%}} = 942\,\mathrm{nm}$ for an assumed filling fraction of $\Phi \approx 15\,\%$. It is evident, that a larger laser power results in more clearly defined diffraction patterns, which could be a hint on better surface quality of the rods. The patterns conform with the ones presented in [59].

the following, the samples with fcc structure are examined. The dip shifts with different laser power, indicating different filling fractions, therewith changing Mie-resonances. The dip position is given in dimensionless frequency $f = a/\lambda$ to make results comparable to simulations. The transmittance is shown in Figure 6.8.

In the transmission microscope images, structural colour is well visible. This indicates a dip in transmittance for visible wavelengths, which was found in Figure 6.4 at around $f = 1.3\,c/a$. Furthermore, there is a dip apparent in the near infrared, which changes position with the laser power (LP) used in the fabrication process. The dips position with respect to the LP is plotted in Figure 6.9. Note, that for the very same settings and LP=23 %, the transmittance dips position changes with about 40 nm compared to the sample measured in Figure 6.7. The origin of this error is hard to tell and is most likely due to outer influences. It is for example possible, that the sample was measured with a slight angle. Thus, Figure 6.9 can only indicate the trend that woodpile structures fabricated with higher laser power posses a dip shifted into the infrared. This might be explained by a higher filling fraction, as the rod spacing is invariant with the laser power, indicated by the diffraction patterns.

After all, the position of the dip seems to be related to the filling fraction respectively line width, making this experiment a possible candidate to measure $\Phi(LP)$ for the woodpile structure. For future research, the writing speed could be set to a targeted value, so that the line width as a function of the deposited laser power per length can be deduced. Evident from the measurements is also a decline in transmittance with decreasing wavelength. In [110] a similar structure is fabricated with the DLW technique, with a dip in transmittance not as pronounced as the present, but with $\lambda_0 \approx$1250 nm at around the same position. Serbin *et.al.* suggested, that the decline in transmittance is

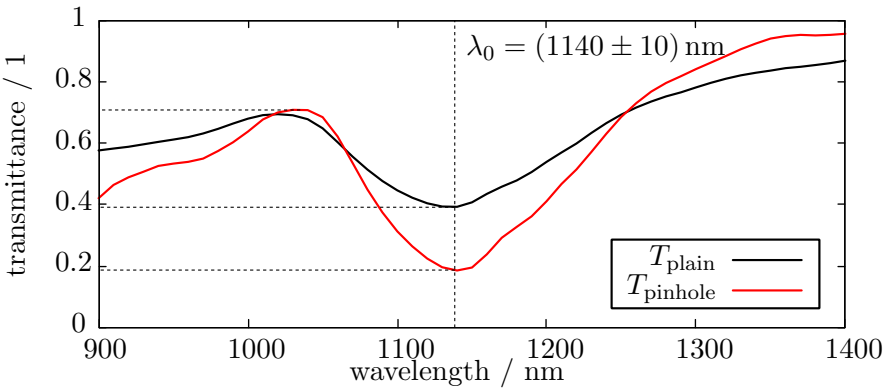

Figure 6.7.: Transmittance spectra through a 15 µm high woodpile structure fabricated with 23 % laser power and $g = 1\,\mu\mathrm{m}$ rod distance. The black curve shows the spectrum measured with the setup as is, the red one with an introduced pinhole. With the pinhole, the incident radiation angle is reduced. With compliance to the dispersion relation, less incident $\boldsymbol{k}$-vectors can couple into the sample, leading to reduced transmittance.

due to Rayleigh scattering caused by imperfections and disorder in the crystal or on the polymer air interface. The wavelength dependency of the scattered light intensity should then be λ^{-4}, see Equation 2.11. Larger scale disorder within the crystal should rather result in wider gaps with reduced depth as the gap conditions are perturbed. The term $I/I_0 = 1 - K\lambda^{-4}$ from Equation 2.11 was fitted to the median spectrum, see Figure B.3. This results in the parameter $K \approx 0.39\,\mu\mathrm{m}^4$, which is close to $K_{\mathrm{Serbin}} = 0.4\,\mu\mathrm{m}^4$ estimated in [110]. However, the assumption that Rayleigh scattering is present is purely hypothetical and needs further investigation. If confirmed, the transmittance could be corrected by the Rayleigh scattering, allowing for a better quantification regarding depth of the dips.

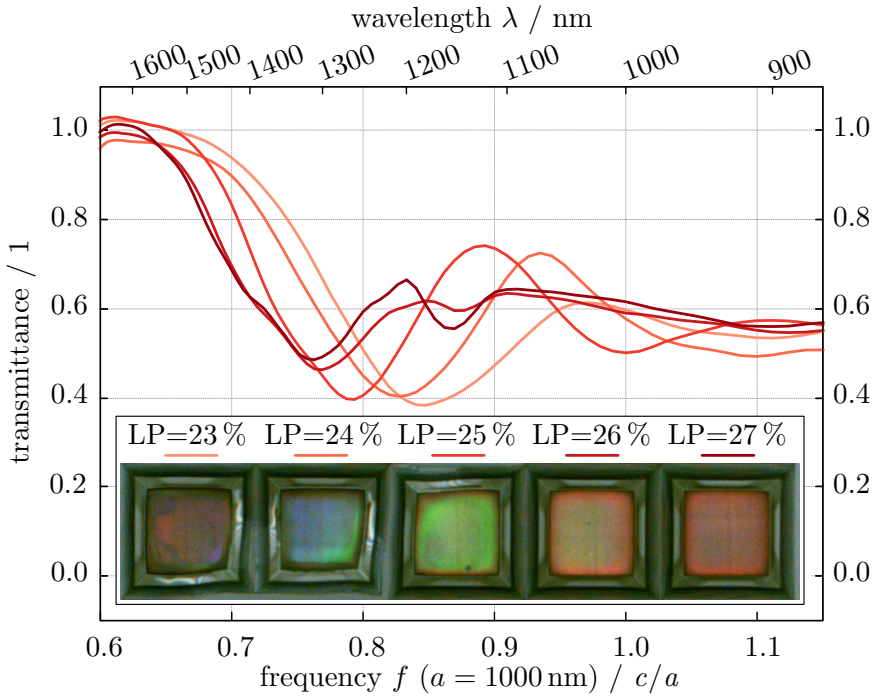

Figure 6.8.: Transmittance spectra of five woodpiles, fabricated with different laser powers. Micrographs are shown in the legend. The spectra are plotted over the frequency to make them comparable to simulations. The dips occur between 0.75 c/a to 0.85 c/a, approximately in range of the FDTD simulation. A double dip occurs for higher laser powers, which is also evident in the simulations. The deviation is attributed to imperfections in the fabrication process.

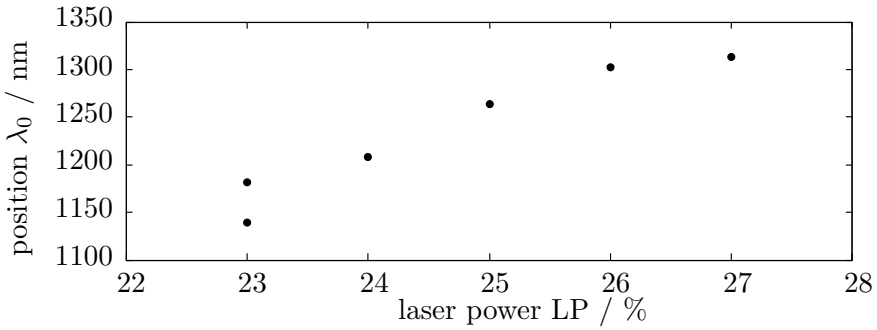

Figure 6.9.: Dip position for woodpile structures fabricated by means of DLW with different LP. The trend is that higher LP yield samples with transmittance dips at larger wave lengths, which could be explained by a larger filling fraction.

6.3. Hyperuniform Structure

The fabrication of the woodpile structure gave confidence that in principle reduced transmittance from band gaps can be simulated as well as measured on a sample fabricated by means of DLW. The next task is to reproduce the pattern found in nature to ultimately investigate the role of hyperuniformity or other characteristics of the decorated point pattern. To begin with, transmittance of a plane wave through the cylindrically decorated hyperuniform point patter is simulated with the FDTD method. As with the woodpile structure in Figure 6.4, transmittance through a structure with a relatively high refractive index $n_{\text{high}} = 3.00$ is compared to the transmittance of a structure with a low refractive index $n_{\text{low}} = 1.50$. The periodicity of the data set is used to eliminate boundary effects, see section 3.5. Results can be found in Figure 6.10.

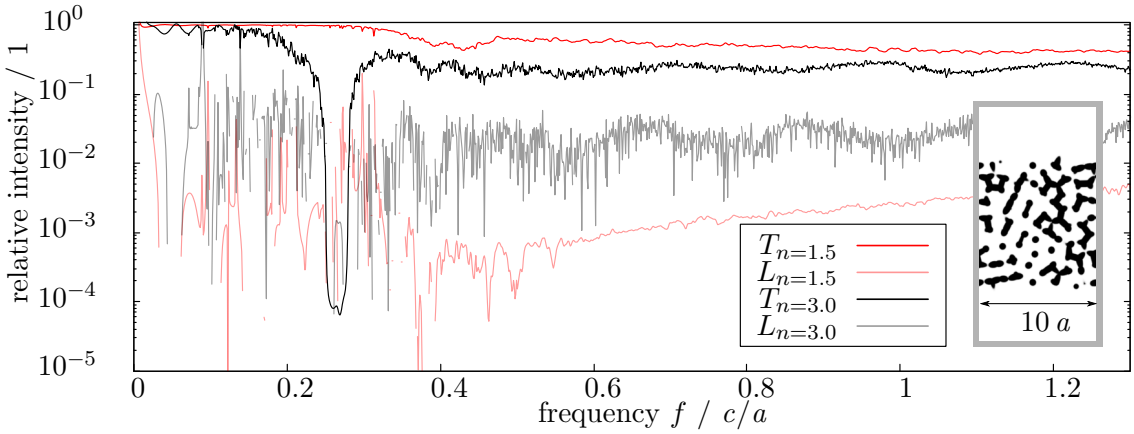

Figure 6.10.: Comparison of the transmittance of two hyperuniform structures with different refractive indices. The red curve is the refractive index of approximately the polymer used in DLW fabrication. Only a slightly reduces transmittance is suggested at $f = 0.4\, c/a$. The transmittance of the higher refractive index structure seems far more promising, the transmittance drops over four orders of magnitude at $f \approx 0.25\, c/a$.

For the low refractive index contrast structure, only very slightly reduced transmittance is found. At a frequency of $\sim 0.4\, c/a$, the transmittance drops to 0.45, before it rises again to 0.75. It is thought that the lack of Mie resonances due to the low refractive index contrast can not fully compensate the lacking Bragg reflections of the amorphous structure.

A drop in transmittance over four orders of magnitude is evident for the high refractive index structure. Given the fact that a structure made by decorating a Poisson patter exhibits no reduced transmittance at all, see Figure 6.1, it can safely be assumed that the dip is of structural origin. This strongly indicates a band gap origin of the reduced transmittance, and the dip will be called a band gap.

6.3.1. Field Visualisation

To get an imagination of what is happening if a wave hits a structure exhibiting a band gap, the electric field is visualised for different frequency regimes, depicted in Figure 6.11. Here, E_x polarisation is shown. E_y polarisation was simulated as well and yielded similar results.

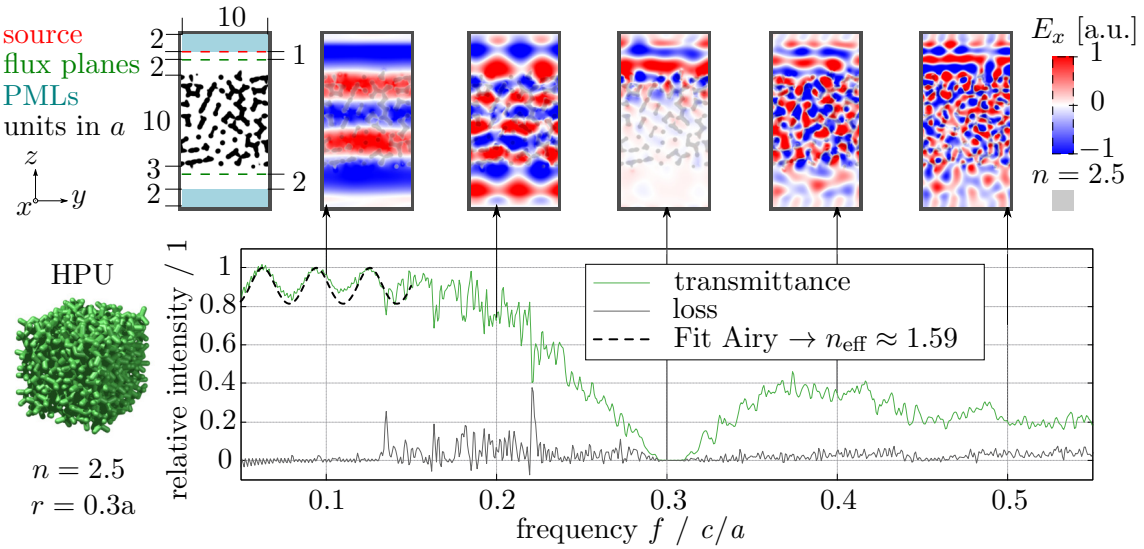

Figure 6.11.: Visualisation of the electric field behaviour in a hyperuniform structure for five different frequencies. In this example the refractive index $n = 2.5$ and the cylinder radius $r = 0.3a$. Negative and positive electric field amplitudes are shown in blue and red, respectively. An animation of the electric field was produced. A recap of the computational cell is given on the top left. The reduced transmittance for frequencies in the band gap region is clearly visible.

It can be seen that for the low frequency regime very little scattering occurs and the wave stays planar, however modified by an effective refractive index n_{eff}. This observation is also stressed by the transmittance spectrum which closely resembles the one of an etalon (see Figure 3.9) in the regime $0.05\,c/a < f < 0.15\,c/a$. Therefore, the Airy formula (Equation 3.4) was fitted to the transmittance in that range, giving an effective refractive index of $n_{\text{eff}} \approx 1.59$. This can be deduced to a filling fraction $\Phi \approx 39\,\%$ according to Equation 3.1. This corresponds well to the Φ calculated with the Monte-Carlo method in section 3.3, showing that the different methods are consistent. The higher the frequency gets, the higher it is influenced by the structure of the refractive index material, stressing the complexity of the Mie scattering regime.

6.3.2. Parameter Sweep

In order to test the influence of filling fraction and refractive index contrast on the band gap, a parameter sweep was done. A band gap was defined for transmittances below 1 %.

The width Δf at this threshold was taken and its midpoint as the gap position f_0. The parameters that were changed are the refractive index n of the rods and the radius r of the cylindrical decoration, respectively filling fraction Φ. A translation between r and Φ can be done with the data from section 3.3. Of interest is the minimal refractive index contrast for a band gap to form and at which filling fraction this occurs. The connection between the parameters and the band gap position and width is as well determinable. The parameter sweep was done by varying the refractive index of the material n from 1.5 to 4 in steps of 0.25 and the radius of the cylindrical decoration r from $0.15a$ to $0.60a$ in steps of $0.05a$. Results can be seen in Figure 6.12, a) for the band gap centre frequency and b) for the band gap width.

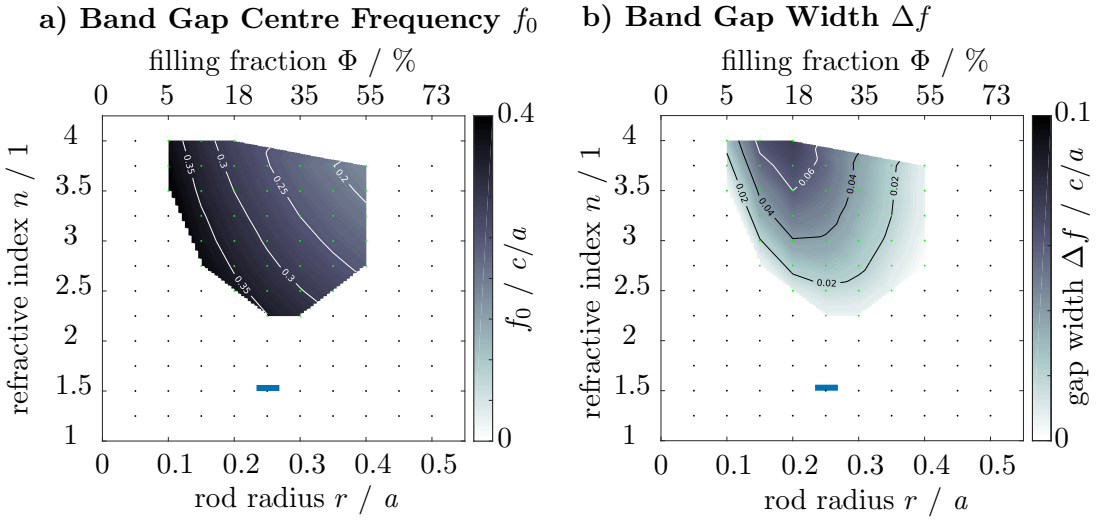

Figure 6.12.: a) band gap centre frequency and a) band gap width, both as a function of refractive index n and radius r or filling fraction Φ, respectively, of the cylindrical decoration on the hyperuniform point pattern. The dots in the parameter plane denote simulated parameters, dots marked in green are parameter pairs at which transmittance below 1 % is present. The contour plot between these points is linearly interpolated. The small blue rectangle area shows the parameters readily available with the DLW method, considering single rod exposure.

Unfortunately, the range covered with the DLW technique is far out of range. The band gap centre frequency is mainly determined by the rod radius and increases with decreasing radius. This parameter could be increased further by multiple, offset exposure of a single rod. The necessary refractive index contrast, however, seems to be the more important parameter, as it can be seen, that the widest gaps occur at the larger refractive index contrasts, as expected. This suggests material conversion of the polymer resin to higher refractive index materials.

The simulation fails to produce results for refractive indices higher than $n_{\max} = 4$. Apparently, the refractive index contrast is too high too be smoothes out correctly by the software. It would be interesting to know, whether there is an upper limit in refractive index contrast above which the band gap ceases to exist. Presumably, at one

point, the reflectance at an interface becomes so high, that regardless of the structure no propagation is possible, simply because the light can not couple in anymore.

The real band gap position can be set by the scaling (defining the length a) of the structure, once a pair of parameters is found for which the structure possesses a band gap, due to the scaling invariance of Maxwell's equations, see section 2.2. Thus, as a measure of quality of a band gap, the ratio of its width to its centre frequency $\Delta f/f_0$ can be taken. For the structure present, this is shown in Figure 6.13

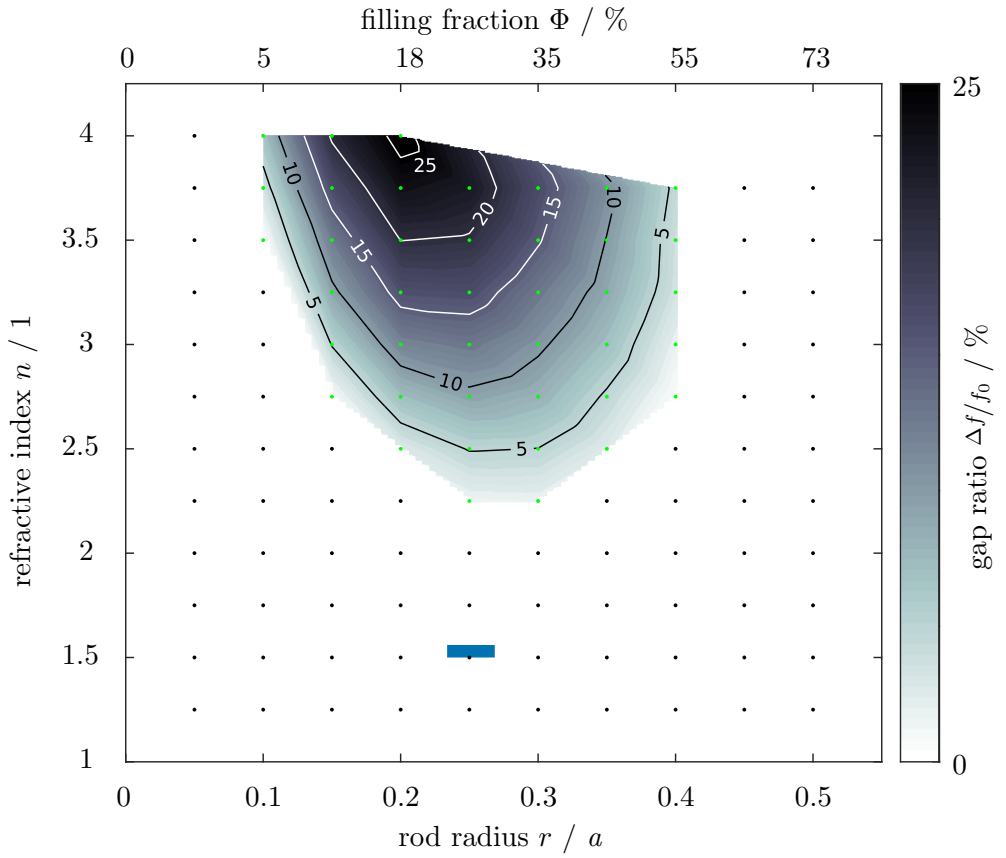

Figure 6.13.: The band gap quality of a cylindrically decorated hyperuniform point pattern as a function of refractive index n and radius r or filling fraction Φ, respectively. The dots in the parameter plane denote simulated parameters, dots marked in green are parameter pairs at which transmittance below 1 % is present. The contour plot between these points is linearly interpolated. The small blue rectangle area shows the parameters readily available with the DLW method, considering single rod exposure.

This map may serve as a guide for which parameters a reasonable band gap is to be expected for the hyperuniform structure. The minimal refractive index contrast necessary is $\Delta n_{\text{min, hpu}} \approx 1.25$, for a filling fraction of around 30 %. Compared to values from literature, this limit was much lower with $\Delta n_{\text{min, crystal}} \geq 0.46$ [8] for perturbed

periodic structures and $\Delta n_{\text{min, wp}} \geq 0.9$ for a woodpile structure [71]. This fact is attributed again to the missing Bragg scattering.

From this parameter sweep it can also be seen, that the aforementioned slight dip in transmittance for the low refractive indices is a foreshadow of a proper band gap for higher refractive index contrasts. By increasing the refractive index contrast, the dip in transmittance does not pop up suddenly, but smoothly becomes deeper until it can be measured trustworthy, as done in this simulation by setting a threshold. This behaviour is illustrated in Figure 6.14.

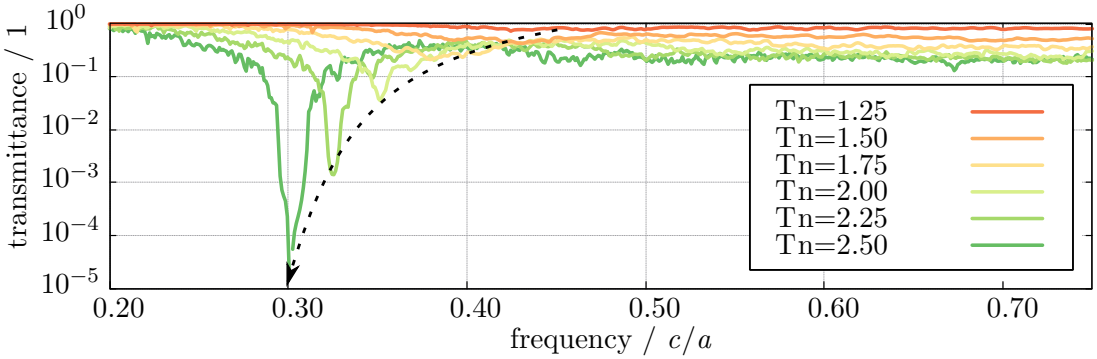

Figure 6.14.: The band gap behaviour for changing refractive index contrast. For larger refractive index contrasts, the band gap shifts to lower frequencies and the reduced transmittance dip becomes deeper faster than exponentially, indicated by the dashed line (free form). Eventually, the minimal transmittance is set by the finite structure size, which in the present case is 1 a, resulting in a minimal transmittance on the order of 10^{-5}. This already gives an estimate for the penetration depth.

6.3.3. Fabrication and Characterisation

Microscope images and SEM micrographs of a fabricated hyperuniform sample can be found in Figure 6.15 a)-c). A sample of 100^2 nm^2 footprint was fabricated, with a characteristic length of 611 nm (the cubic data set was scaled to 7.1 µm sidelength). Diffraction patterns were already shown in section 5.1 and together with the SEM micrographs, good sample quality can be attested.

The transmittance of the sample was measured with the spectroscopy setup (section 5.2) and results are presented in Figure 6.16.

A reduced transmittance is adumbrated. The fact that the measurement process lead to reliable results for the woodpile structure gives confidence that the small dip is not a measurement artefact, but is positively caused by the very structure of the exposed photo resist. The authenticity is further stressed by the change in dip position with changing fabrication laser power. Higher laser powers yields higher filling fractions, which shifts the dip to larger wavelengths. This was already seen on the woodpile structures Figure 6.9.

With this measurement, it is proven that amorphous meta materials that posses a

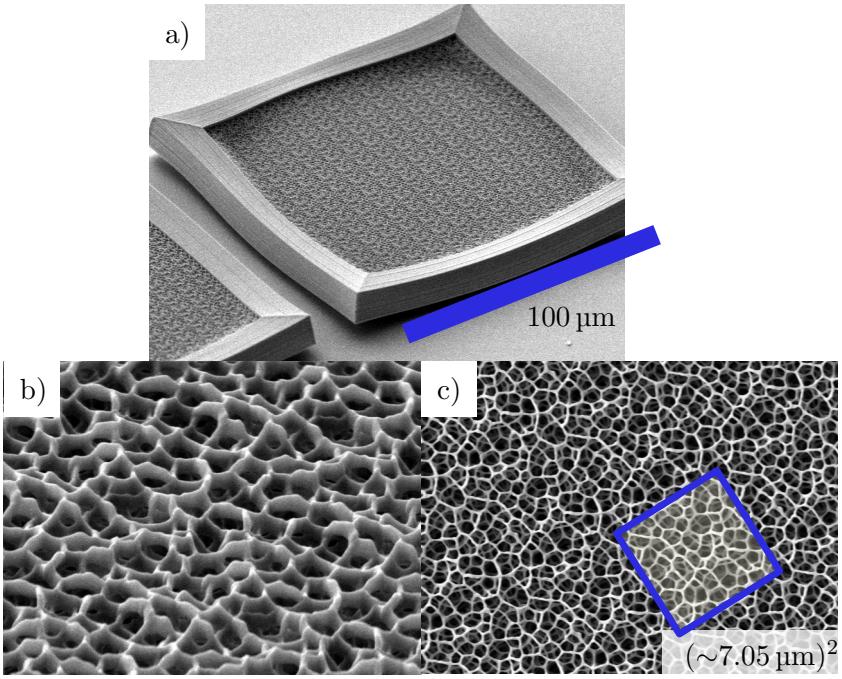

Figure 6.15.: Fabrication results for a hyperuniform structure with characteristic length of 611 nm. SEM micrographs are shown and confirm the little shrinkage measured from the diffraction pattern in section 5.1. The fabricated samples are 12 µm high and have a footpring of 100^2 nm^2.

band stop can be fabricated by means of DLW at a scale that is relevant for telecommunication applications. The 1000 points in the hyperuniform data proved to be enough to produce a measurable dip in transmittance. Considering characterisation of the sample, its periodicity is helpful, as it lets one conveniently measure the shrinkage of the fabricated sample. Considering the parameter of fabrication laser power, it was found that a stable structure is far more important for a dip to form than pushing the line width thickness to its minimum.

A next step is to fabricate a large sample array, similar as done with the woodpile structures, to further delimit the parameter space. An issues with the fabrication software has to be faced, as it allows only for a certain amount of data to be processed at once, hindering the fabrication of more than three such structures at once. Furthermore, material conversion needs to be pursued, in order to verify postulated decrease of transmittance in the band gap with rising refractive index contrast. Of larger interest would also be to understand the influence of the elliptical decoration. It is assumed that the band gap is not isotropic, as the filling fraction depends in the propagation direction. A dip shifted to larger wavelengths is expected for electromagnetic radiation propagating transverse to the z axis of elongation.

Finally, a macroscopic set of samples was manufactured from the hyperuniform data set, together with Dirk Ropers. The aim is to make them subject to a similar measure-

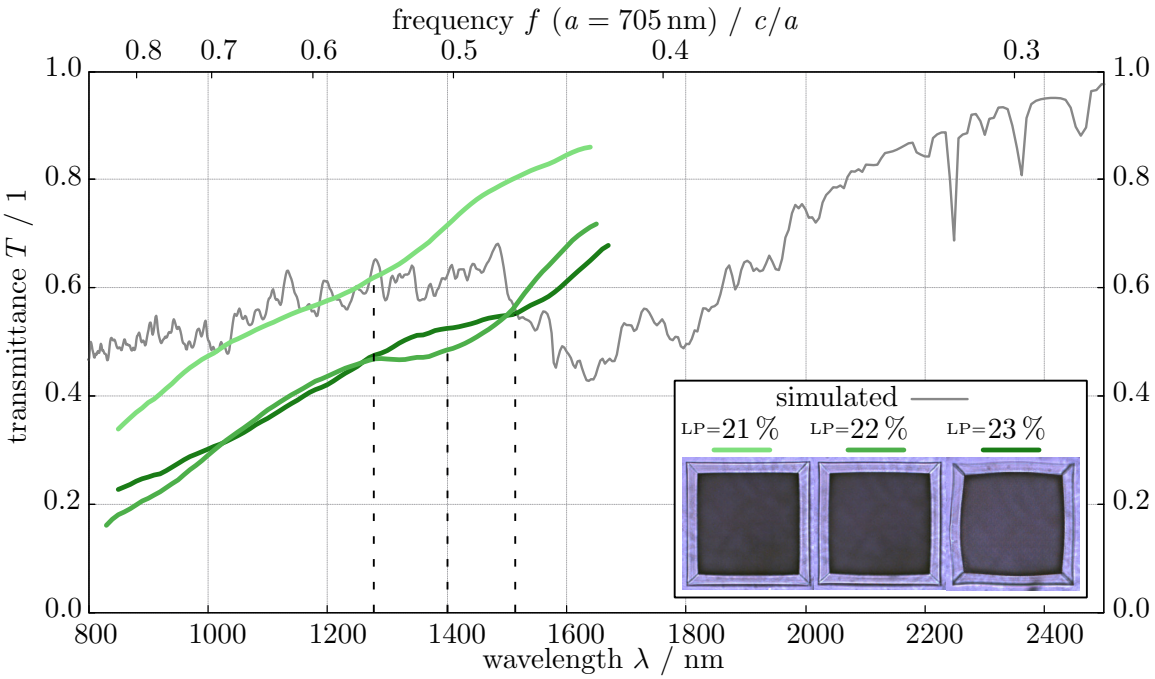

Figure 6.16.: Transmittance through three samples fabricated from the hyperuniform data set, with different laser powers. Reduced transmittance at around the targeted value of 1550 nm is slightly visible. Note the absence of structural colour, indicating that no higher order dip is present, contrary to the woodpile structure, Figure 6.8. The discrepancy of simulation and experiment is credited to different filling fractions and the elliptical versus cylindrical decoration.

ment process as done in [20] for a "photonic amorphous diamond" (PAD) structure.

The cylindrical decoration as well as the its inverse have been printed by the external company *i.materialize* in polyamide (refractive index at microwaves $n \sim 1.6$ [84]) with ∼13 cm sidelength. The samples are depicted in Figure 6.17. A photonic band gap is expected at around 9 GHz frequency corresponding to 33 mm wavelength, which is in the microwave regime. The procedure is to submerge the inverse structure in water whose refractive index is comparably large in the microwave regime, but absorption should still be weak enough. It will be possible to tune the refractive index of water in the range $6.5 \leq n \leq 8$ of water by changing its temperature in the range $0\,^{\circ}\mathrm{C} \leq T \leq 60\,^{\circ}\mathrm{C}$ [111]. The suitable characterisation experiments have to be assembled yet.

6.4. Pattern Extraction

It was possible to generate a data set suitable for preliminary pattern extraction from slicing an *Agapornis roseicollis* feather barb. The imaging was done together with Dirk Ropers. Due to the limited time frame of the thesis, the pattern could not be examined to the full extend, and a full quantification with proper error approximation can not be

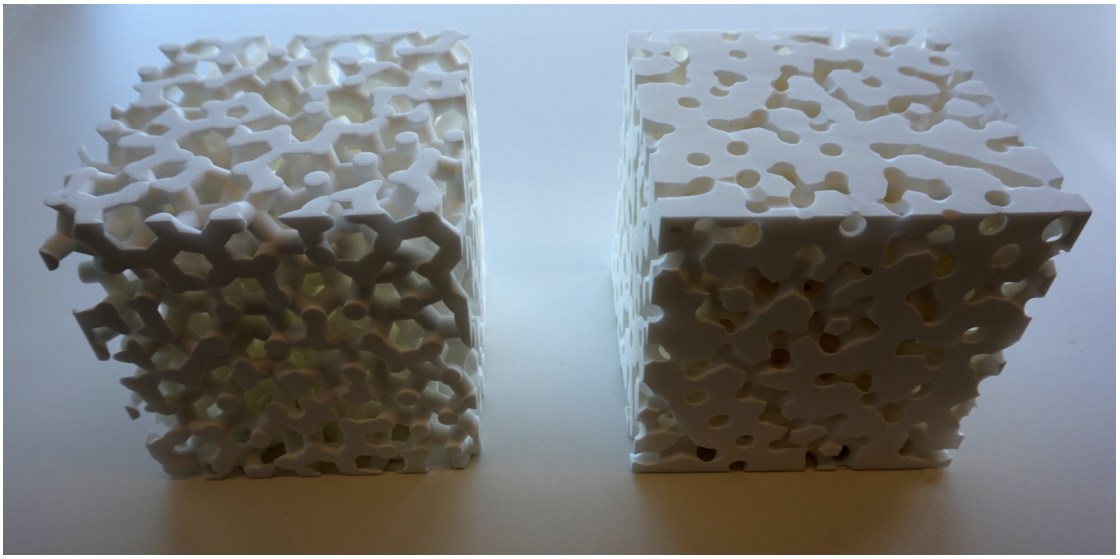

Figure 6.17.: Macroscopic samples created from the hyperuniform data set. Shown left is the the point pattern cylindrically decorated, shown rigth its topological inverse, which will be submerged in water for future research. A large refractive index contrast is created with that.

given.

One example image of the slices is given in Figure 6.18, a), and the resultant volume data in b). No infiltration was done, in order to keep the curtaining effect to a minimum.

The extracted volume is approximately $3.6\,\mu m \times 3.9\,\mu m \times 4.9\,\mu m$ in size. The resolution in x and y is 9.1 nm/px whereas in z direction 25 nm/px. The resolution in z direction is furthermore afflicted with an unknown error that needs to be taken care of in further investigation. The characteristic length can be deduced to $\sim$170 nm from a Fourier transform of the spongy area of the slice shown in Figure 6.18. This would give $19\,\mathrm{px}/l_{\mathrm{char}}$ resolution in x and y direction, well within the limit deduced in subsection 5.3.3. However, only $6\,\mathrm{px}/l_{\mathrm{char}}$ resolution in z direction could be achieved, which is below the value for a pattern to be extracted reliably.

Nevertheless, the image processing method was applied, yielding a filling fraction estimate of $\Phi \approx 33\,\%$ or an effective refractive index of $n_{\mathrm{eff}} \approx 1.18$, respectively. After Equation 2.1, this gives a peak reflectance for light of approximately 400 nm wavelength. This no unrealistic value, but rather low due to the low filling fraction.

The point pattern was extracted furthermore. The extracted pattern consists of roughly 15 000 points. If the total volume is divided by the average volume of a point (the cubed characteristic length), a similar value is obtained. The resultant statistics, however, show a trihedral network topology, contrary to the current belief of a tetrahedral network [28]. The statistic is shown in Figure 6.19, compared to the hyperuniform pattern.

Due to the great uncertainty in z resolution, a further discussion is postponed until reliable data is available. The attempt to extract the point pattern proved, however,

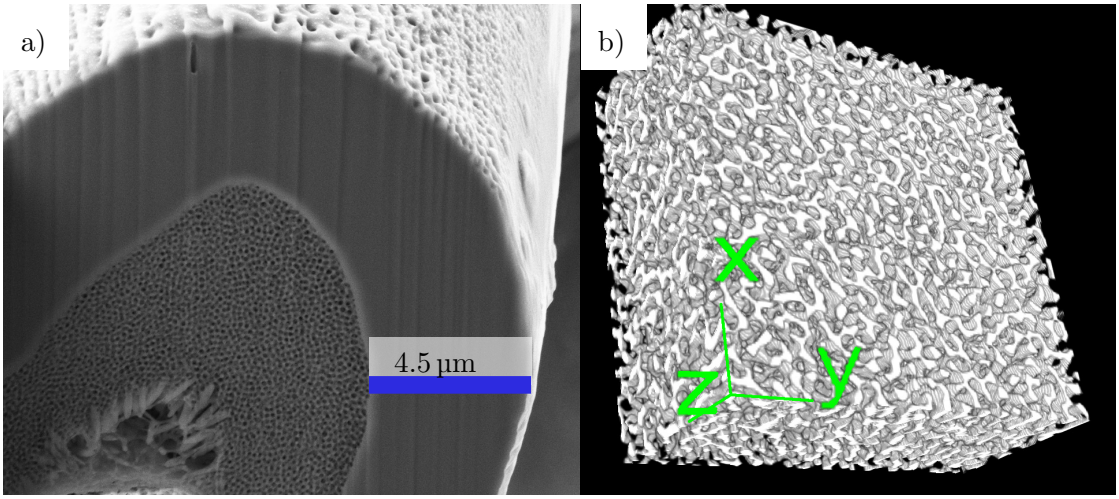

Figure 6.18.: a) shows an example slice through a feather barb of a *Agapornis roseicollis*. b) shows the extracted volume data of 200 such slices, not corrected for the different aspect ratio in z direction coming from a different resolution. The slices where aligned using the outer shell of the feather to correct for uncontrollable drift during the imaging process.

that the basic procedure is ready to be applied on better data. Further work includes the fine tuning of the imaging process, with strong emphasis on analysing the exact slice thickness of the FIB. By introducing the infiltration method to enlarge the keratin to air contrast, further improvements are to be expected. Most recently, a numerical method was published to reconstruct images flawed by the curtaining effect [112]. Another idea to overcome the FIB issue altogether is to utilise a microtome, which is capable of producing slices down to 20 nm thickness. This is still too large for the extraction method to be applied reliably. Further effort could be put in the search for larger scale random network structures, that produce colour with red hue. No species is known until now, however, that possesses a red, non-iridescent structural colour. Instead, in the chapters above the DLW method was proven to be capable of producing amorphous photonic band gap materials with characteristic lengths of around 600 nm. The procedure to examine DLW fabricated structures with the pattern extraction method suggests itself for future research.

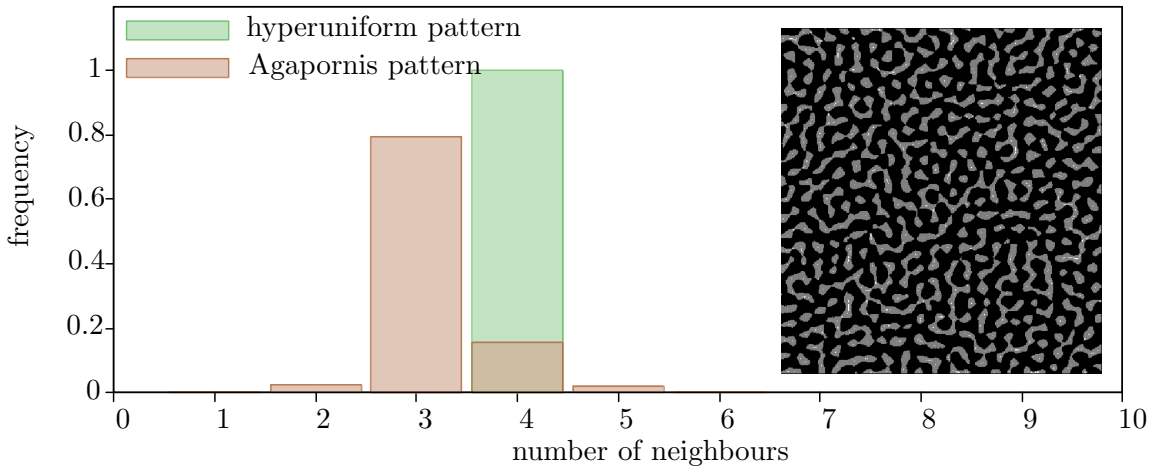

Figure 6.19.: Neighbours distribution of the extracted pattern. A trihedral is present, contrary to the tetrahedral hyperuniform pattern and current belief [28]. The inset shows a slice though the extracted volume data together with the calculated skeleton, visible as light points in the grey keratin structure. The air voids are depicted black.

7. Conclusion and Outlook

A toolbox of considerable size was collected within the course of this work that enables the study of photonic meta materials. It is now possible to successfully simulate, fabricate and moreover characterise meta materials with a photonic band gap. This is of great interest for applications, where waveguides are one possible object of interest, as well as fundamental theoretical investigations, namely identify the properties a pattern needs to posses to form such a photonic band gap, for example. Not only periodic structures were investigated, but also the dataset of an amorphous point pattern was employed, provided by our collaborators Marian Florescu (Princeton University), Paul Chaikin (New York University) and Paul Steinhardt (Princeton University). The pattern posses the property of hyperuniformity, its long range density fluctuations vanish, and according to most recent theories, hyperuniformity is one criterion that enables a band gap.

Built upon the experience from preliminary work of Ropers and Knappe, samples from this data set were fabricated by means of the direct laser writing (DLW) technology. Despite a low refractive index contrast and a filling fraction less than half of the recommended value given by our collaborators, surprisingly, reduced transmittance was found. Close to $\lambda = 1550\,\mathrm{nm}$ wavelength, important for modern telecommunications, an ever so small dip in transmission was found. This peculiar finding needed thorough testing, as even the performed finite-difference time-domain (FDTD) simulations only indicate the weakest change in transmittance, if at all.

The simulations done with the *Meep* software package [80] show that substantially reduced transmittance emerges only for higher refractive index contrasts. Having examined this behaviour further with a systematic parameter sweep, other interesting questions arise, regarding the exact behaviour of a wave in such a medium. The field distribution for waves with frequencies at the band edges could be examined in further research, in order to stress a band gap origin of the reduced transmittance. For waveguides in photonic band gap structures, the penetration depth can give a limit on how close two waveguides can be built before they interact and couple into each other, making further simulations uttermost worthwhile. Point sources inside the structure might be simulated and the flow through concentric flux spheres calculated. By comparing the findings to structures obtained from e.g. Poisson patterns would allow to determine the influence of the structure factor, of interest for the fundamental theory. By writing the *Pointpatterntool*, a software was established that allows for convenient handling of point pattern data sets and generation of basic statistics, and further research is pioneered.

By comparing results with the well known woodpile structure, the authenticity of the measurement of the hyperuniform sample was further assured. The periodicity of the woodpile structure furthermore permits utilisation of Bloch's theorem, allowing to a different kind of simulation: the plane wave expansion method, implemented in the *MPB*

software package [76]. With that, the complete three dimensional dispersion relation was calculated successfully, for a high and low refractive index contrast and furthermore the density of states (DOS) was deduced. A genuine band gap was found for high refractive index contrasts, in compliance with literature [42]. For the low refractive index, interesting properties regarding the coupling of the light into the structure were deduced. A cross check with the FDTD simulation indeed reveals reduced transmittance, for either case.

With the woodpile structure, the fabrication process by means of DLW was greatly improved. It became evident that the final fabricated structures properties depend on a very delicate interplay of the parameters. Moreover, the parameters are not independent of each other, but interact. For example, the line width changes dependent on the very structure itself, for otherwise the same settings. This influences the filling fraction as a fundamental parameter that determines the formation of a band gap. For every structure that one wants to fabricate, the influence of the parameters need to be tested thoroughly. Only then reliable statements e.g. on the filling fraction can be done and a well defined sample can be fabricated. As the simulations predict a more pronounced gap for higher refractive indices, material conversion e.g. with the introduced sol-gel processes together with the calcination of the keratin structure is promising to enhance any present band gap.

The need for non-destructive methods arose, and a scattering experiment was set up. It is possible to collect diffraction patterns of a sample, revealing information on characteristic lengths in the sample. The decoupling of the diffracted light into air was regarded, and the measurement of the characteristic length verified by imaging the samples with the SEM. Thus, with the scattering experiment a valuable method was employed that allows to measure the sample quality without destroying the sample. As the filling fraction is such a crucial quantity, further methods should be developed. One could exploit the change in effective refractive index by infiltration with refractive index liquids, as shown in [59] for the woodpile structures. With that, the optical path length would change slightly, which is then measurable with an interferometer setup. This should be done with large wavelengths with respect to the structural variation, which would imply far infra red wavelengths. These are less prone to scattering but behave like in a homogeneous medium with effective refractive index, which was stressed by the simulations.

With the reconditioned spectroscopy setup transmittance spectra of the samples can now be measured reliably, as proven on the example of the woodpile structure. The measured dip corresponds to the simulated transmittance and dispersion relation, within the range of uncertainty, further stressing the authenticity of the measured reduced transmittance of the hyperuniform structure. By replacing the photo diode in the spectrometer experiment with a camera, and the thermal light source with a tunable laser source, the spectrometer and scattering experiment can be combined. A frequency resolved diffraction pattern can then be measured, revealing more properties of the sample. Furthermore, a spatially resolved transmission spectrum can be taken. This may not only allow for conclusions to a band gap, but also on the light propagation behaviour near a band edge.

The structural colour found in nature, for example in the green medullary cells of the feather barbs of *Agapornis roseicollis*, indicates that a reduced transmittance is very well possible for such low refractive indices. Further examination is consequential, and a thin slice reconstruction with the focused ion beam (FIB) was performed in order to extract the keratin volume information. A dedicated extraction method was contrived, that allows to extract the point pattern of such a keratin network. This extraction method was beforehand tested on artificially generated thin slices to delimit its capabilities. The minimal needed resolution is close to the maximally achievable resolution of the FIB facility, regarding the thickness of a slice. Despite great challenges in the proper settings of the SEM and FIB device, a preliminary data set could be harvested and the extraction method was applied as an experiment. The results proves to be promising and the findings justify further research: instead of possessing a tetrahedral network topology like the hyperuniform data set, a trihedral topology is indicated, contradicting theories in literature. Especially with contrast enhancement, achieved by the sol-gel process, more reliable data can be expected to verify or falsify these very surprising findings.

Summarising, by testing the accuracy of the spectrometer setup, cross checking results with a periodic structure, considering existent band stop structures from nature and monitoring the band gap evolution with change in the refractive index contrast with simulations, strong evidence is given that the reduced transmittance measured for the hyperuniform sample truly stems from a band gap origin. This is the first time reported that an amorphous structure, fabricated purely by means of DLW, possesses a measurable band stop. Furthermore, with the collected methods the path for future research is cleared.

8. Zusammenfassung

Im Verlauf dieser Arbeit wurde eine beachtlicher Werkzeugkasten zusammengestellt um photonische Metamaterialien zu untersuchen. Es ist nun möglich, deren Verhalten zu simulieren, sie erfolgreich herzustellen und zu charakterisieren. Dies ist von großem Interesse in der Anwendung, wo Wellenleiter ein möglicher Gegenstand von Untersuchungen sind, wie auch in der theoretischen Erforschung dieser Materialien, um zum Beispiel herauszufinden, welche Eigenschaften ein Punktmuster besitzen muss um eine Bandlücke zu ermöglichen. Nebst der Untersuchung periodischer Strukturen wurde auch der Datensatz eines amorphen Punktmusters eingesetzt, bereitgestellt von unseren Kollaborateuren Marian Florescu (Princeton University), Paul Chaikin (New York University) und Paul Steinhardt (Princeton University). Das Muster besitzt die Eigenschaft der Hyperuniformität, seine langreichweitigen Dichtefluktuationen verschwinden, was nach den gängigen Theorien ein Kriterium ist, das eine Bandlücke ermöglicht.

Mit der Erfahrung, die durch die Arbeiten von Knappe [30] und Ropers [29] gesammelt wurden, konnten Proben mithilfe des direkten Laserschreibverfahrens (Englisch: direct laser writing, DLW) aus diesem Datensatz hergestellt werden. Trotz des vergleichsweise geringen Kontrasts im Brechungsindex und einem Füllfaktor weniger als halb so groß wie von unseren Kollaborateuren vorgeschlagen, konnte eine verminderte Lichtdurchlässigkeit gemessen werden. Nahe der für die moderne Fernmeldetechnik wichtige Wellenlänge von $\lambda = 1550\,\mathrm{nm}$ konnte ein kleiner Einbruch der Transmission detektiert werden. Dieser unerwartete Fund bedurfte einer gründlichen Untersuchung, da selbst die Finite-Differenzen-Methode (Englisch: finite-difference time-domain, FDTD) nur einen sehr kleinen Einbruch erwarten ließ.

Die Simulationen wurden mit dem *Meep* Sofwarepaket [80] durchgeführt, und lassen eine wesentlich reduzierte Transmission nur für relativ große Kontraste im Brechungsindex erwarten. Durch eine Untersuchung der wesentlichen Parameter wurden weitere interessant Fragen aufgeworfen die das exakte Verhalten einer Welle in einem solchen Medium betrifft. Die Feldverteilung von Wellen mit einer Frequenz an der Bandkante könnte in zukünftigen Untersuchungen weiteren Aufschluss über die Herkunft der verminderten Transmission geben. Für die Anwendung von Wellenleitern in einem solchen Medium ist die Eindringtiefe von großem Interesse, da sie eine Vorstellung geben kann, wie nahe man zwei Wellenleiter bringen kann, bevor sie miteinander wechselwirken und ineinander einkoppeln. Dies macht weitere Simulationen äußerst lohnenswert. Punktquellen in der Struktur könnten simuliert werden, und der Fluss durch konzentrische, kugelförmige Flächen berechnet werden. Die gewonnenen Erkenntnisse können mit Strukturen verglichen werden, die zum Beispiel aus Poissonmustern generiert wurden, um die fundamentale Theorie zu untersuchen. Mit dem *Pointpatterntool* (Englisch für Punktmusterwerkzeug) wurde eine Software entwickelt, die eine passende Handhabung

der Punktmusterdatensätze erlaubt und die die wesentlichen Statistiken erstellen kann, womit die Pionierarbeit für zukünftige Forschung geleistet wurde.

Durch den Vergleich mit Ergebnissen der wohlbekannten Woodpilestruktur (englisch für Holzstapelstruktur) konnte die Glaubwürdigkeit der Messungen an der hyperuniformen Probe bestätigt werden. Des Weiteren erfüllt die Woodpilestruktur mit ihrer Periodizität die Bedingungen um das Blochtheorem anwenden zu können, was wiederum eine andere Art von Simulation ermöglicht: das Expansionsverfahren mit ebenen Wellen (englisch: plane wave expansion method), implementiert im *MPB* Softwarepaket [76]. Mit ihr konnte die komplette dreidimensionale Dispersionsrelation und auch die Zustandsdichte sowohl für einen hohen, als auch einen niedrigen Brechungsindexkontrast erfolgreich berechnet werden. Für den hohen Brechungsindexkontrast wurde in Übereinstimmung mit der Literatur [42] eine echte Bandlücke gefunden. Der niedrige Brechungsindex zeigte hingegen interessante Eigenschaften auf was das ein- und auskoppeln von Licht in die Struktur betrifft. Die Gegenprobe mit der FDTD Simulation ergab tatsächlich eine in beiden Fällen verminderte Transmission.

Durch Zuhilfenahme der Woodpilestruktur konnte der Herstellungsprozess in hohem Maße verbessert werden. Es wurde deutlich, dass die Eigenschaften der endgültigen Probe vom äußerst delikaten Zusammenspiel der Herstellungsparameter abhängen. Zudem sind diese Parameter nicht unabhängig voneinander, sondern beeinflussen beide die gleichen Eigenschaften der Probe. Dies zeigt sich zum Beispiel darin, dass die Strichdicke von der Struktur selbst abhängt. Das beeinflusst den Füllfaktor als essentiellen Parameter für die Bildung einer Bandlücke. Für jede unterschiedliche Struktur die man herstellen möchte muss der Einfluss der Parameter einzeln getestet werden. Nur dann ist gewährleistet, dass die endgültige Struktur die gewünschten, genau definierten Eigenschaften besitzt. Da die Simulationen eine ausgeprägtere Reduktion der Transmission für hohe Brechungsindexkontraste voraussagt ist eine Materialumwandlung vielversprechend um die Bandlücke deutlicher zu machen, zum Beispiel realisierbar durch den vorgestellten Sol-Gel-Prozess, zusammen mit der Kalzinierung des Keratins.

Da Methoden die es erlauben eine Probe zerstörungsfrei zu untersuchen von Nöten waren, wurde ein Streuexperiment aufgebaut. Mit ihm ist es möglich, das Beugungsbild einer Probe aufzunehmen, welches Informationen über charakteristische Längen in der Probe enthält. Die Auskopplung des gestreuten Lichts in Luft wurde beachtet, und die berechneten Ergebnisse für die charakteristischen Längen mit Elektronenmikroskopaufnahmen bestätigt. Daher ist mit dem Streuexperiment ein wertvolles Werkzeug aufgebaut worden, das Rückschlüsse auf die Qualität der Struktur erlaubt, ohne sie zu zerstören. Da der Füllfaktor ein solch wichtiger Parameter für die Bildung einer Bandlücke ist, sollten weitere Methoden entwickelt werden um ebendiesen zu messen. Man könnte zum Beispiel die Änderung des effektiven Brechungsindex ausnutzen, wenn die Probe mit unterschiedlichen Flüssigkeiten infiltriert wird, wie in [59] für die Woodpilestruktur gezeigt. Damit ändert sich der optische Weg durch die Probe, was mit einem Interferometer messbar wäre. Hierbei sollten verglichen mit der Strukturvariation lange Wellenlängen verwendet werden, was ferninfrarotes Licht impliziert. Wie in den Simulationen gezeitg, werden diese weit weniger gestreut, sondern verhalten sich wie in einem homogenen Medium mit effektivem Brechungsindex.

Mit dem verbesserten Spektrometer können nun Transmissionsspektren verlässlich aufgezeichnet werden, wie am Beispiel der Woodpilestrukturen gezeigt wurde. Der gemessene Einbruch in der Transmission stimmt sowohl mit der Simulation, als auch mit der berechneten Dispersionsrelation weitestgehend überein und bestätigt erneut die Echtheit der gemessenen Daten der hyperuniformen Struktur. Würde die Photodiode im Spektrometeraufbau durch einen räumlich auflösenden Chip ersetzt, und die thermische Lichtquelle durch einen durchstimmbaren Laser, könnten Streu- und Spektrometeraufbau kombiniert werden. Ein frequenzaufgelöstes Beugungsmuster könnte gemessen werden, was weitere Eigenschaften der Probe enthüllt. Außerdem kann ein ortsaufgelöstes Transmissionsspektrum gemessen werde. Dies ermöglicht nicht nur Rückschlüsse auf eine Bandlücke, sondern auch auf Transporteigenschaften des Lichts nahe einer Bandlücke.

Die strukturellen Farben in der Natur, zum Beispiel vorhanden in den grünen Markzellen von Federästen der *Agapornis roseicollis*, lassen vermuten, dass eine reduzierte Transmission sehr wohl für solch niedrige Brechungsindexkontraste möglich ist. Eine gründliche Untersuchung ist konsequent und eine Dünnschichtrekonstruktion mit einem fokussierten Ionenstrahl (englisch: focused ion beam, FIB) wurde eingesetzt um die Volumeninformation des Keratins zu erhalten. Eine Methode wurde entwickelt um das Punktmuster der Keratinstruktur zu extrahieren. Deren Möglichkeiten wurde zuerst mit künstlich erstellten Schnittbildern ausgelotet. Die minimal erforderliche Auflösung, was die Schnittdicke betrifft, liegt gerade im Bereich der maximal möglichen Auflösung des FIB-Gerätes. Trotz der großen Herrausforderung was die vielfältigen Einstellungen der Geräte betrifft konnte ein vorläufiger Datensatz über die Volumeninformation generiert werden und die Methode zur Punktextraktion wurde testweise angewandt. Die Ergebnisse scheinen vielversprechend und rechtfertigen weitere Untersuchungen: Anstelle einer vier- wurde eine dreifache Netzwerktopologie gefunden, was den gängigen Theorien widerspricht. Vor allem durch die Verbesserung des Kontrasts durch den Sol-Gel-Prozess werden verlässlichere Daten erwartet, die diese sehr unerwarteten Ergebnisse bestätigen oder widerlegen werden.

Zusammengefasst, durch Prüfung der Genauigkeit des Spektrometers, Vergleich mit periodischen Strukturen, in Betracht ziehen von natürlichen strukturellen Farben und Beobachtung der Bandlückenbildung mit veränderlichem Brechungsindex durch die Simulationen besteht der starke Verdacht, dass die gemessene reduzierte Transmission der hyperuniformen Struktur seinen Ursprung wirklich in einer Bandlücke hat. Dies ist das erste Mal, das von einer amorphen Struktur berichtet wird, die einzig mit dem direkten Laserschreibverfahren hergestellt wurde und eine messbaren Bandsperre besitzt. Zudem wurde mit den zusammengetragenen Methoden der Weg für zukünftige Forschung geebnet.

Bibliography

[1] P. Gargini. The international technology roadmap for semiconductors (itrs): "past, present and future". In *GaAs IC Symposium, 2000. 22nd Annual*, pages 3–5, Nov 2000. (p. 1)

[2] Thomas M. Conte and Paolo A. Gargini. On the foundation of the new computing industry beyond 2020. electronic, 2015. (p. 1)

[3] Alberto Politi, Martin J. Cryan, John G. Rarity, Siyuan Yu, and Jeremy L. O'Brien. Silica-on-silicon waveguide quantum circuits. *Science*, 320(5876):646–649, 2008. (p. 1)

[4] T. D. Ladd, F. Jelezko, R. Laflamme, Y. Nakamura, C. Monroe, and J. L. O/'Brien. Quantum computers. *Nature*, 464(7285):45–53, March 2010. (p. 1)

[5] Malte C. Gather Kristjan Leosson and Petur G. Hermannsson. *Plasmonics and Plasmonic Metamaterials. Analysis and Application*, volume 4 of *Nanoscience and Nanotechnology*, chapter Long-range Surface Plasmon Polarition Waveguides and Devices, page 197ff. World Scientific, 2011. (p. 1)

[6] Lukas Siedentop. Investigating waveguides for plasmons. Bachelor's thesis, University of Konstanz / University of Iceland, September 2013. (p. 1)

[7] Eli Yablonovitch. Inhibited spontaneous emission in solid-state physics and electronics. *Phys. Rev. Lett.*, 58:2059–2062, May 1987. (p. 1, 40)

[8] Sajeev John. Strong localization of photons in certain disordered dielectric superlattices. *Phys. Rev. Lett.*, 58:2486–2489, Jun 1987. (p. 1, 21, 85)

[9] P. W. Anderson. Absence of diffusion in certain random lattices. *Phys. Rev.*, 109:1492–1505, Mar 1958. (p. 1)

[10] Costas M. Soukoulis and Martin Wegener. Past achievements and future challenges in the development of three-dimensional photonic metamaterials. *Nat Photon*, 5(9):523–530, September 2011. (p. 1)

[11] Jonathan C. Knight. Photonic crystal fibres. *Nature*, 424(6950):847–851, August 2003. (p. 1)

[12] S. John. Photonic band gap materials: a semiconductor for light. In *Quantum Electronics and Laser Science Conference, 2002. QELS '02. Technical Digest. Summaries of Papers Presented at the*, pages 73–74, May 2002. (p. 2)

[13] G. B. Benedek. Theory of transparency of the eye. *Appl. Opt.*, 10(3):459–473, Mar 1971. (p. 2, 6)

[14] A. Ishimaru. Wave propagation and scattering in random media and rough surfaces. *Proceedings of the IEEE*, 79(10):1359–1366, Oct 1991. (p. 2, 8)

[15] D. Weaire. Existence of a gap in the electronic density of states of a tetrahedrally bonded solid of arbitrary structure. *Phys. Rev. Lett.*, 26:1541–1543, Jun 1971. (p. 2, 23)

[16] Toralf Scharf Carsten Rockstuhl, editor. *Amorphous Nanophotonics*. Nano-Optics and Nanophotonics. Springer-Verlag Berlin Heidelberg, 1 edition, 2013. (p. 2, 8)

[17] Salvatore Torquato and Frank H. Stillinger. Local density fluctuations, hyperuniformity, and order metrics. *Phys. Rev. E*, 68:041113, Oct 2003. (p. 2, 15, 16, 29)

[18] Weining Man, Marian Florescu, Eric Paul Williamson, Yingquan He, Seyed Reza Hashemizad, Brian YC Leung, Devin Robert Liner, Salvatore Torquato, Paul M Chaikin, and Paul J Steinhardt. Isotropic band gaps and freeform waveguides observed in hyperuniform disordered photonic solids. *Proceedings of the National Academy of Sciences*, 110(40):15886–15891, 2013. (p. 2, 33, 73)

[19] Keiichi Edagawa, Satoshi Kanoko, and Masaya Notomi. Photonic amorphous diamond structure with a 3d photonic band gap. *Phys. Rev. Lett.*, 100:013901, Jan 2008. (p. 2, 22, 40)

[20] Shigeki Imagawa, Keiichi Edagawa, Keisuke Morita, Toshiki Niino, Yutaka Kagawa, and Masaya Notomi. Photonic band-gap formation, light diffusion, and localization in photonic amorphous diamond structures. *Phys. Rev. B*, 82:115116, Sep 2010. (p. 2, 22, 88)

[21] C. V. Raman. The origin of the colours in the plumage of birds. *Proceedings of the Indian Academy of Sciences - Section A*, 1(1):1–7, 1934. (p. 2, 3)

[22] H. J. Swatland. Optical characteristics of natural iridescence in meat. *Journal of Food Science*, 49(3):685–686, 1984. (p. 2)

[23] H.J. Swatland. Iridescence in beef caused by multilayer interference from sarcomere discs. *Meat Science*, 90(2):398 – 401, 2012. (p. 2)

[24] Wei Zhang, Miguel Anaya, Gabriel Lozano, Mauricio E. Calvo, Michael B. Johnston, Hernán Míguez, and Henry J. Snaith. Highly Efficient Perovskite Solar Cells with Tunable Structural Color. *Nano Letters*, 15(3):1698–1702, 2015. PMID: 25650872. (p. 2)

[25] Richard O Prum and Rodolfo H Torres. Structural colouration of mammalian skin: convergent evolution of coherently scattering dermal collagen arrays. *Journal of Experimental Biology*, 207(12):2157–2172, 2004. (p. 2, 5)

[26] RICHARD O Prum. Anatomy, physics, and evolution of structural colors. *Bird coloration*, 1:295–353, 2006. (p. 2)

[27] Eric R. Dufresne, Heeso Noh, Vinodkumar Saranathan, Simon G. J. Mochrie, Hui Cao, and Richard O. Prum. Self-assembly of amorphous biophotonic nanostructures by phase separation. *Soft Matter*, 5:1792–1795, 2009. (p. 2, 5, 7, 39, 52)

[28] Haiwei Yin, Biqin Dong, Xiaohan Liu, Tianrong Zhan, Lei Shi, Jian Zi, and Eli Yablonovitch. Amorphous diamond-structured photonic crystal in the feather barbs of the scarlet macaw. *Proceedings of the National Academy of Sciences*, 109(27):10798–10801, 2012. (p. 2, 89, 91)

[29] Dirk Ropers. Herstellung von nanostrukturen im 3d-laser-lithographieverfahren. Diplomarbeit, Universität Konstanz & Universität Marburg, March 2014. (p. 2, 10, 27, 28, 31, 40, 41, 43, 52, 59, 97)

[30] Philipp Knappe. Charakterisierung photonischer strukturen. Bachelorarbeit, Universität Konstanz, May 2014. (p. 2, 59, 60, 61, 62, 97)

[31] Silvia Vignolini, Paula J. Rudall, Alice V. Rowland, Alison Reed, Edwige Moyroud, Robert B. Faden, Jeremy J. Baumberg, Beverley J. Glover, and Ullrich Steiner. Pointillist structural color in pollia fruit. *Proceedings of the National Academy of Sciences*, 109(39):15712–15715, 2012. (p. 4)

[32] S Kinoshita, S Yoshioka, and J Miyazaki. Physics of structural colors. *Reports on Progress in Physics*, 71(7):076401, 2008. (p. 4, 5)

[33] B. Q. Dong, X. H. Liu, T. R. Zhan, L. P. Jiang, H. W. Yin, F. Liu, and J. Zi. Structural coloration and photonic pseudogap in natural random close-packing photonic structures. *Opt. Express*, 18(14):14430–14438, Jul 2010. (p. 4)

[34] Betty Kientz, Peter Vukusic, Stephen Luke, and Eric Rosenfeld. Iridescence of a marine bacterium and classification of prokaryotic structural colors. *Applied and environmental microbiology*, 78(7):2092–2099, 2012. (p. 4)

[35] Hein L. Leertouwer, Bodo D. Wilts, and Doekele G. Stavenga. Refractive index and dispersion of butterfly chitin and bird keratin measured by polarizing interference microscopy. *Opt. Express*, 19(24):24061–24066, Nov 2011. (p. 4)

[36] Richard O. Prum, Rodolfo Torres, Scott Williamson, and Jan Dyck. Two-dimensional fourier analysis of the spongy medullary keratin of structurally coloured feather barbs. *Proceedings of the Royal Society of London B: Biological Sciences*, 266(1414):13–22, 1999. (p. 4, 5, 6)

[37] Richard O. Prum, Jeff A. Cole, and Rodolfo H. Torres. Blue integumentary structural colours in dragonflies (odonata) are not produced by incoherent tyndall scattering. *Journal of Experimental Biology*, 207(22):3999–4009, 2004. (p. 5)

[38] Richard O. Prum, Rodolfo H. Torres, Scott Williamson, and Jan Dyck. Coherent light scattering by blue feather barbs. *Nature*, 396(6706):28–29, #nov# 1998.

[39] Matthew D Shawkey, Vinodkumar Saranathan, Hildur Pálsdóttir, John Crum, Mark H Ellisman, Manfred Auer, and Richard O Prum. Electron tomography, three-dimensional fourier analysis and colour prediction of a three-dimensional amorphous biophotonic nanostructure. *Journal of The Royal Society Interface*, 6(Suppl 2):S213–S220, 2009. (p. 5, 63)

[40] Lei Shi, Haiwei Yin, Renyuan Zhang, Xiaohan Liu, Jian Zi, and Dongyuan Zhao. Macroporous oxide structures with short-range order and bright structural coloration: a replication from parrot feather barbs. *J. Mater. Chem.*, 20:90–93, 2010. (p. 7, 64)

[41] A. Saito. Material design and structural color inspired by biomimetic approach. *Science and Technology of Advanced Materials*, 12(6):064709, #dec# 2011. (p. 8)

[42] John D Joannopoulos, Steven G Johnson, Joshua N Winn, and Robert D Meade. *Photonic crystals: molding the flow of light*. Princeton university press, 2008. (p. 8, 94, 98)

[43] E. Yablonovitch. Photonic band-gap structures. *J. Opt. Soc. Am. B*, 10(2):283–295, Feb 1993. (p. 8, 39)

[44] Keiichi Edagawa. Photonic crystals, amorphous materials, and quasicrystals. *Science and Technology of Advanced Materials*, 15(3):034805, 2014. (p. 8, 11, 18, 19, 21)

[45] Diederik S. Wiersma. Disordered photonics. *Nat Photon*, 7(3):188–196, #mar# 2013. (p. 8)

[46] Hans Moosmüller and W. Patrick Arnott. Particle optics in the rayleigh regime. *Journal of the Air & Waste Management Association*, 59(9):1028–1031, 2009. (p. 10)

[47] Jesper Serbin and Min Gu. Superprism phenomena in waveguide-coupled woodpile structures fabricated by two-photon polymerization. *Opt. Express*, 14(8):3563–3568, Apr 2006. (p. 11)

[48] Raymond C. Rumpf and Javier J. Pazos. Optimization of planar self-collimating photonic crystals. *J. Opt. Soc. Am. A*, 30(7):1297–1304, Jul 2013. (p. 12)

[49] R. Gross and A. Marx. *Festkörperphysik*. Festkörperphysik. De Gruyter, 2012. (p. 12)

[50] Max Born. Quantenmechanik der stoßvorgänge. *Zeitschrift für Physik*, 38(11):803–827, 1926. (p. 12)

[51] Robert D. Batten, Frank H. Stillinger, and Salvatore Torquato. Classical disordered ground states: Super-ideal gases and stealth and equi-luminous materials. *Journal of Applied Physics*, 104(3):–, 2008. (p. 15, 17)

[52] Obioma U. Uche, Salvatore Torquato, and Frank H. Stillinger. Collective coordinate control of density distributions. *Phys. Rev. E*, 74(3):031104, Sep 2006. (p. 15, 16, 27)

[53] Marian Florescu, Salvatore Torquato, and Paul J. Steinhardt. Designer disordered materials with large, complete photonic band gaps. *Proceedings of the National Academy of Sciences*, 106(49):20658–20663, 2009. (p. 15, 17, 21, 24, 27, 33, 77)

[54] L. S. Froufe-Pérez, M. Engel, P. F. Damasceno, N. Muller, J. Haberko, S. C. Glotzer, and F. Scheffold. The Role of Short-Range Order and Hyperuniformity in the Formation of Band Gaps in Disordered Photonic Materials. *ArXiv e-prints*, February 2016. (p. 15, 18, 27)

[55] Aleksandar Donev, Frank H. Stillinger, and Salvatore Torquato. Unexpected density fluctuations in jammed disordered sphere packings. *Phys. Rev. Lett.*, 95:090604, Aug 2005. (p. 15, 16)

[56] Nicolas Muller, Jakub Haberko, Catherine Marichy, and Frank Scheffold. Silicon hyperuniform disordered photonic materials with a pronounced gap in the short-wave infrared. *Advanced Optical Materials*, 2(2):115–119, 2014. (p. 15, 39)

[57] Yang Jiao, Timothy Lau, Haralampos Hatzikirou, Michael Meyer-Hermann, Joseph C. Corbo, and Salvatore Torquato. Avian photoreceptor patterns represent a disordered hyperuniform solution to a multiscale packing problem. *Phys. Rev. E*, 89:022721, Feb 2014. (p. 16)

[58] Mark Grundland, Jiri Patera, Zuzana Masáková, and Neil A. Dodgson. Image sampling with quasicrystals. *CoRR*, abs/0907.3604, 2009. (p. 16)

[59] B. C. Brüser, I. Staude, G. von Freymann, M. Wegener, and U. Pietsch. Visible light laue diffraction from woodpile photonic crystals. *Applied Optics*, 51(28):6732–6737, October 2012. (p. 16, 55, 56, 77, 79, 94, 98, 112)

[60] Chase E Zachary and Salvatore Torquato. Hyperuniformity in point patterns and two-phase random heterogeneous media. *Journal of Statistical Mechanics: Theory and Experiment*, 2009(12):P12015, 2009. (p. 16)

[61] E. Lidorikis, M. M. Sigalas, E. N. Economou, and C. M. Soukoulis. Tight-binding parametrization for photonic band gap materials. *Phys. Rev. Lett.*, 81:1405–1408, Aug 1998. (p. 18, 21)

[62] E. Lidorikis, M. M. Sigalas, E. N. Economou, and C. M. Soukoulis. Gap deformation and classical wave localization in disordered two-dimensional photonic-band-gap materials. *Phys. Rev. B*, 61:13458–13464, May 2000. (p. 18)

[63] M.A. Omar. *Elementary Solid State Physics: Principles and Applications.* Addison-Wesley series in solid state sciences. Addison-Wesley Publishing Company, 1993. (p. 21)

[64] Carsten Rockstuhl, Ulf Peschel, and Falk Lederer. Correlation between single-cylinder properties and bandgap formation in photonic structures. *Opt. Lett.*, 31(11):1741–1743, Jun 2006. (p. 21)

[65] A. Moroz and A. Tip. Resonance-induced effects in photonic crystals,. *J. Phys. Condens.Matter*, 1999. (p. 21, 22)

[66] E. N. Economou and M. M. Sigalas. Classical wave propagation in periodic structures: Cermet versus network topology. *Phys. Rev. B*, 48:13434–13438, Nov 1993. (p. 22)

[67] M. Maldovan and E.L. Thomas. Simultaneous complete elastic and electromagnetic band gaps in periodic structures. *Applied Physics B*, 83(4):595–600, 2006. (p. 22)

[68] Seng Fatt Liew, Jin-Kyu Yang, Heeso Noh, Carl F. Schreck, Eric R. Dufresne, Corey S. O'Hern, and Hui Cao. Photonic band gaps in three-dimensional network structures with short-range order. *Phys. Rev. A*, 84:063818, Dec 2011. (p. 22)

[69] D. Weaire and M. F. Thorpe. Electronic properties of an amorphous solid. i. a simple tight-binding theory. *Phys. Rev. B*, 4:2508–2520, Oct 1971. (p. 23)

[70] HS Sözüer and Jonathan P Dowling. Photonic band calculations for woodpile structures. *Journal of Modern Optics*, 41(2):231–239, 1994. (p. 23, 39)

[71] K.M. Ho, C.T. Chan, C.M. Soukoulis, R. Biswas, and M. Sigalas. Photonic band gaps in three dimensions: New layer-by-layer periodic structures. *Solid State Communications*, 89(5):413 – 416, 1994. (p. 23, 39, 86)

[72] S. Y. Lin, J. G. Fleming, D. L. Hetherington, B. K. Smith, R. Biswas, K. M. Ho, M. M. Sigalas, W. Zubrzycki, S. R. Kurtz, and Jim Bur. A three-dimensional photonic crystal operating at infrared wavelengths. *Nature*, 394(6690):251–253, July 1998. (p. 23, 39)

[73] Hallam Oaks Pty. Ltd. Persistence of Vision Raytracer (POV-Ray). (p. 26, 28, 69)

[74] private communication. The code to calculate the structure factor and further discussion about it was received from Herbert Kaiser, PhD at the University of Konstanz, Department of Physics. (p. 28, 30)

[75] Ralf Tweer. *Vielfachstreuung von Licht in Systemen dicht gepackter Mie-Streuer : Auf dem Weg zur Anderson-Lokalisierung?* PhD thesis, Universität Konstanz, July 2002. (p. 32)

[76] Steven G. Johnson and J. D. Joannopoulos. Block-iterative frequency-domain methods for maxwell's equations in a planewave basis. *Opt. Express*, 8(3):173–190, Jan 2001. (p. 33, 94, 98)

[77] Aaron J. Danner. An introduction to the plane wave expansion method for calculating photonic crystal band diagrams. HTML, January 2011. (p. 33)

[78] Tushar Prasad, Vicki Colvin, and Daniel Mittleman. Superprism phenomenon in three-dimensional macroporous polymer photonic crystals. *Phys. Rev. B*, 67:165103, Apr 2003. (p. 34, 73)

[79] Kane Yee. Numerical solution of initial boundary value problems involving maxwell's equations in isotropic media. *Antennas and Propagation, IEEE Transactions on*, 14(3):302–307, May 1966. (p. 34, 35)

[80] Ardavan F. Oskooi, David Roundy, Mihai Ibanescu, Peter Bermel, J.D. Joannopoulos, and Steven G. Johnson. Meep: A flexible free-software package for electromagnetic simulations by the fdtd method. *Computer Physics Communications*, 181(3):687 – 702, 2010. (p. 34, 37, 93, 97)

[81] Allen Taflove and Susan C Hagness. *Computational electrodynamics*. Artech house publishers, 2000. (p. 35)

[82] W. Zinth and U. Zinth. *Optik: Lichtstrahlen - Wellen - Photonen*. Oldenbourg, 2009. (p. 37)

[83] Georg von Freymann, Vladimir Kitaev, Bettina V. Lotsch, and Geoffrey A. Ozin. Bottom-up assembly of photonic crystals. *Chem. Soc. Rev.*, 42:2528–2554, 2013. (p. 39)

[84] Zulkifli Ahmad. *Dielectric Material*, chapter Polymeric Dielectric Materials, pages 3–26. InTech, October 2012. (p. 39, 88)

[85] W. N. Man, M. Florescu, K. Matsuyama, P. Yadak, G. Nahal, S. Hashemizad, E. Williamson, P. Steinhardt, S. Torquato, and P. Chaikin. Photonic band gap in isotropic hyperuniform disordered solids with low dielectric contrast. *Optics Express*, 21(17):19972–19981, #aug# 2013. (p. 40)

[86] Joachim Fischer and Martin Wegener. Three-dimensional direct laser writing inspired by stimulated-emission-depletion microscopy. *Opt. Mater. Express*, 1(4):614–624, Aug 2011. (p. 40)

[87] Richard Wollhofen, Julia Katzmann, Calin Hrelescu, Jaroslaw Jacak, and Thomas A. Klar. 120 nm resolution and 55 nm structure size in sted-lithography. *Opt. Express*, 21(9):10831–10840, May 2013. (p. 40)

[88] Florin Jipa, Marian Zamfirescu, Alin Velea, Mihai Popescu, and Razvan Dabu. *Updates in Advanced Lithography*, volume 1, chapter Femtosecond Laser Lithography in Organic and Non-Organic Materials, pages 65–94. InTech, July 2013. (p. 40)

[89] Nanoscribe GmbH, Hermann-von-Helmholtz-Platz 1 76344 Eggenstein-Leopoldshafen Germany. *Nanoscribe Photonic Professional User Manual Version 1.4*, 1.4 edition, June 2011. (p. 40, 41, 48)

[90] Nanoscribe GmbH. nanoscribe - true 3d lithography. electronic, Hermann-von-Helmholtz-Platz 1 76344 Eggenstein-Leopoldshafen Germany, February 2011. (p. 40)

[91] Nadya Anscombe. Direct laser writing. *Nat Photon*, 4(1):22–23, January 2010. (p. 41)

[92] Nanoscribe GmBH, Hermann-von-Helmholtz-Platz 1 76344 Eggenstein-Leopoldshafen. *IP-Photoresist*, germany edition. (p. 40, 56)

[93] Takeji Hashimoto. Dynamics in spinodal decomposition of polymer mixtures. *Phase Transitions*, 12(1):47–119, 1988. (p. 52)

[94] T. Hashimoto, M. Takenaka, and H. Jinnai. Scattering studies of self-assembling processes of polymer blends in spinodal decomposition. *Journal of Applied Crystallography*, 24(5):457–466, Oct 1991. (p. 53)

[95] Naomi Kumano, Takahiro Seki, Masahiko Ishii, Hiroshi Nakamura, and Yukikazu Takeoka. Tunable angle-independent structural color from a phase-separated porous gel. *Angewandte Chemie*, 123(17):4098–4101, 2011. (p. 53)

[96] C. Christiansen. Untersuchungen über die optischen eigenschaften von fein vertheilten körpern. *Annalen der Physik*, 259(10):298–306, 1884. (p. 53)

[97] *SLS202, SLS202/M Stabilized Infrared Light Source User Guide*. (p. 60)

[98] Princeton Instruments. *Operating Instructions Acton Research Corporation SpectraPro-2150i, 0.150 Meter Focal Length Dual Grating Imaging Monochromator / Spectrograph*, rev. 3.08.28 edition. (p. 60)

[99] *Hamamatsu G8370 InGaAs Photodiode Datasheet*. (p. 60, 61)

[100] *Thorlabs FD10D InGaAs Photodiode Datasheet*. (p. 60)

[101] Lucille A Giannuzzi et al. *Introduction to focused ion beams: instrumentation, theory, techniques and practice*. Springer Science & Business Media, 2006. (p. 63)

[102] K.D. Vernon-Parry. Scanning electron microscopy: an introduction. *III-Vs Review*, 13(4):40 – 44, 2000. (p. 63)

[103] private communication. Functionality and settings for SEM imaging and FIB slicing were discussed with Dipl.-Phys. Matthias Hagner, facility manager for the Nanostructure Laboratory, University of Konstanz. (p. 64)

[104] Michael R. Berthold, Nicolas Cebron, Fabian Dill, Thomas R. Gabriel, Tobias Kötter, Thorsten Meinl, Peter Ohl, Christoph Sieb, Kilian Thiel, and Bernd Wiswedel. KNIME: The Konstanz Information Miner. In *Studies in Classification, Data Analysis, and Knowledge Organization (GfKL 2007)*. Springer, 2007. (p. 66)

[105] private communication. Workflow developed in conversation with Christian Dietz, Research assistant at the University of Konstanz, Department of Computer and Information Science. (p. 66)

[106] Karel Zuiderveld. Contrast limited adaptive histogram equalization. In Paul S. Heckbert, editor, *Graphics Gems IV*, chapter Image Processing, pages 474–485. Academic Press Professional, Inc., San Diego, CA, USA, March 1994. (p. 67)

[107] David L. Donoho Ery Arias-Castro. Does median filtering truly preserve edges better than linear filtering? *The Annals of Statistics*, 37(3):1172–1206, 2009. (p. 67)

[108] Ta-Chih Lee, Rangasami L. Kashyap, and Chong-Nam Chu. Building skeleton models via 3-d medial surface/axis thinning algorithms. *CVGIP: Graph. Models Image Process.*, 56(6):462–478, November 1994. (p. 68)

[109] H. Homann. Implementation of a 3d thinning algorithm. *The Insight Journal*, 10 2007. (p. 68)

[110] J. Serbin, A. Ovsianikov, and B. Chichkov. Fabrication of woodpile structures by two-photon polymerization and investigation of their optical properties. *Optics Express*, 12(21):5221–5228, October 2004. (p. 79, 80)

[111] Udo Kaatze. Complex permittivity of water as a function of frequency and temperature. *Journal of Chemical & Engineering Data*, 34(4):371–374, 1989. (p. 88)

[112] J. H. Fitschen, J. Ma, and S. Schuff. Removal of Curtaining Effects by a Variational Model with Directional Forward Differences. *ArXiv e-prints*, July 2015. (p. 90)

A. Woodpile Fabrication

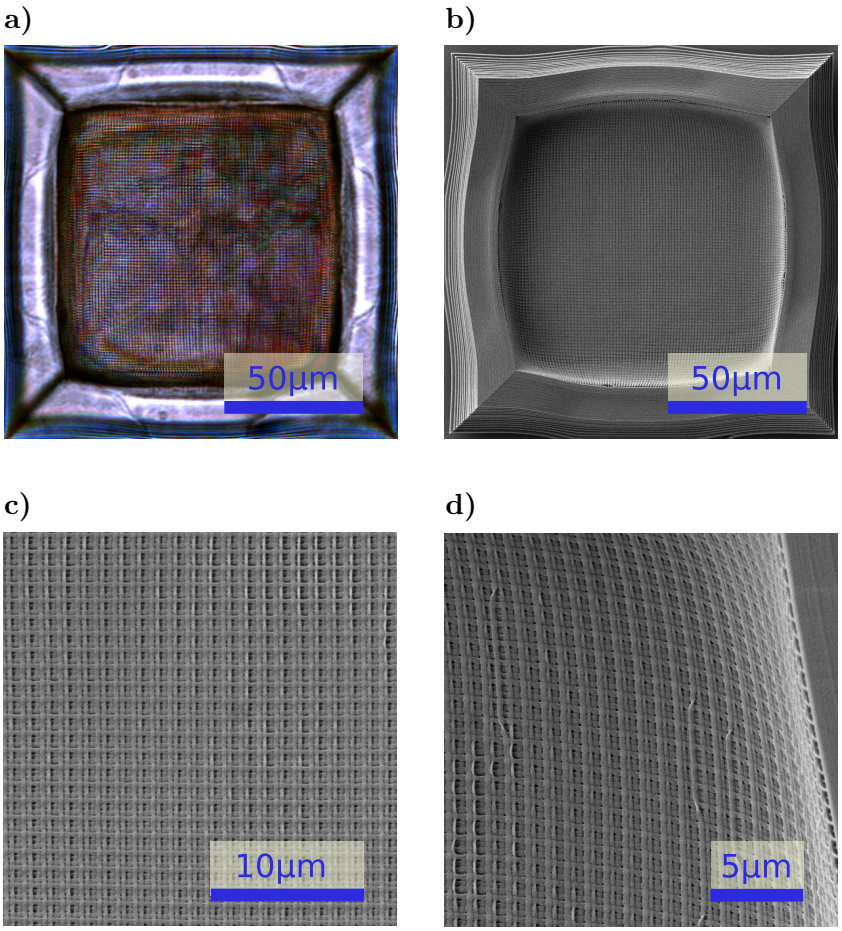

Figure A.1.: Woodpile structure fabricated with 22 % laser power (4.4 mW), otherwise same parameters as in Figure 6.5. Both have a programmed footprint of , 15 µm height and line spacing of $g = 1\,\mu m$. a) shows a transmission light micrograph, b)-d) SEM micrographs. Presumably, the rods fall over due to capillary forces when the developer dries, as the low exposing laser power leaves the structure too weak to resist these forces.

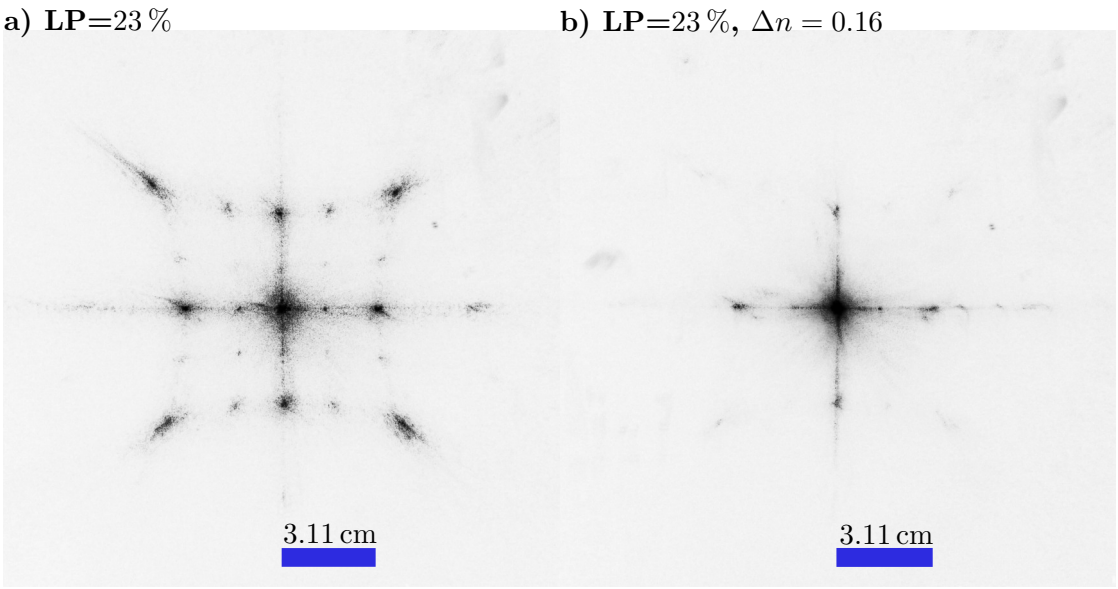

Figure A.2.: Diffraction pattern of a woodpile structures, fabricated with 23 % laser power. a) shows the sample in air and b) infiltrated with ethanol. The blue scale bars denote the distance of the first diffraction peak to the zeroth on the screen. From a sample to screen distance of $d_{\mathrm{ss}} = 5\,\mathrm{cm}$, $d = 975\,\mathrm{nm}$ can be deduced for both cases. As stated in section 5.1, the change in effective refractive index has immeasurable effects. These patterns conform with the ones presented in [59].

B. Woodpile Measurements

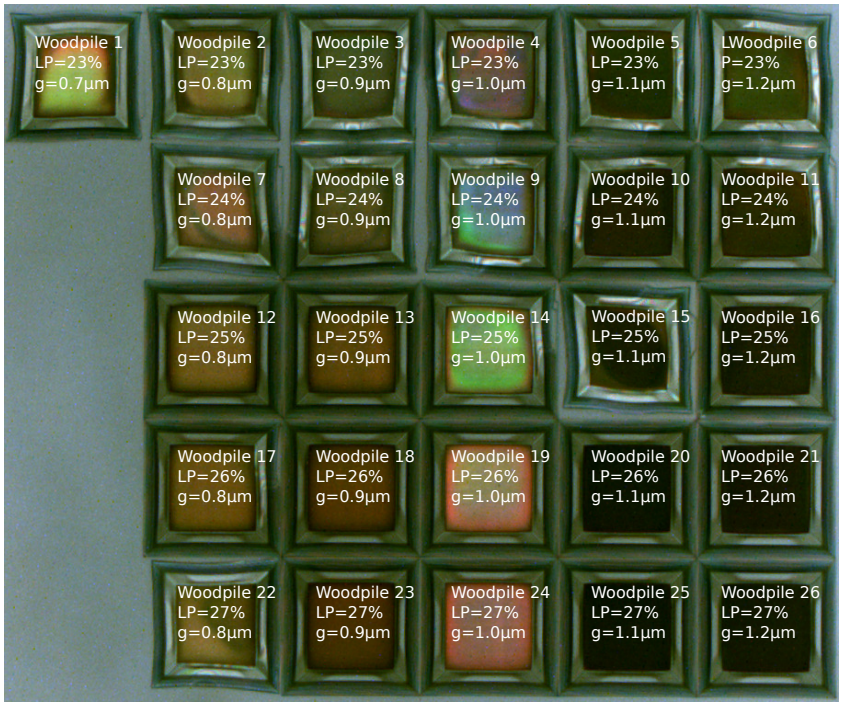

Figure B.1.: Micrographs of 26 woodpiles, fabricated with different parameters. The samples with $g = 1\,\mu m$ posses a fcc structure and show structural colour. The colour changes with increasing laser power used during fabrication, indicating a change in rod thickness.

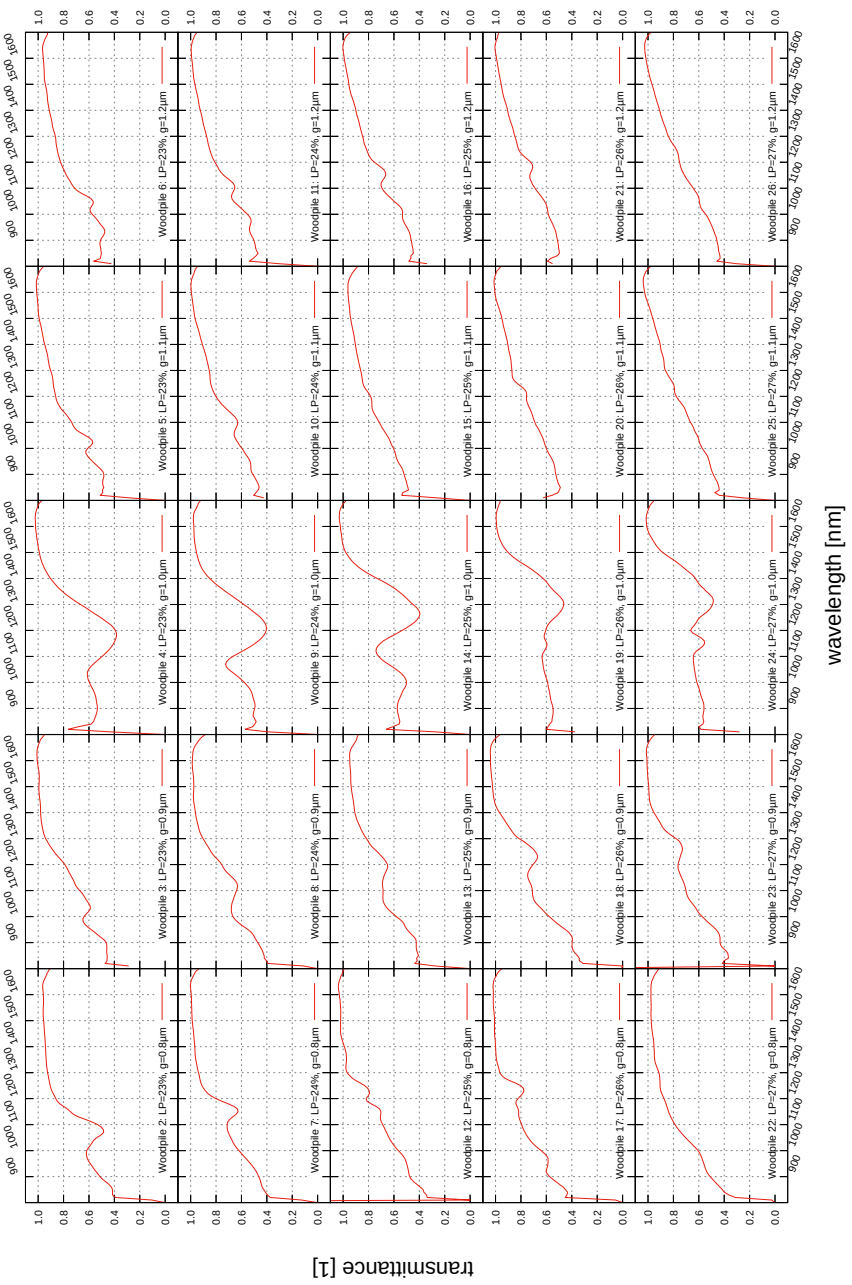

Figure B.2.: Transmittance meassurement of 26 woodpiles, fabricated with different parameters.

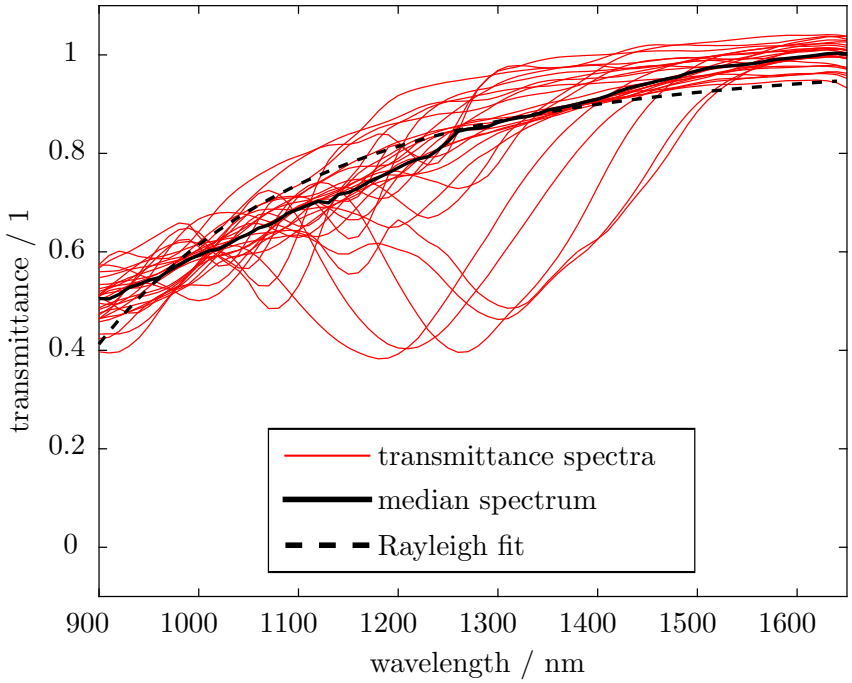

Figure B.3.: Rayleigh fit to the transmittance data of the measured woodpile samples. The fit is done to the median transmittance spectrum to balance out the low transmittance of the dips.

Danksagungen

Während der vergangenen sechs Jahre hatte ich die Möglichkeit unglaublich viele Dinge zu lernen, nicht nur über die Physik. Die vergangenen zwölf Monate markieren den Abschluss meines Physikstudiums, und nun ist es an der Zeit mich bei all jenen zu bedanken, die dies beides ermöglicht und es erst so sehr lohnenswert gemacht haben.

Gebührender Dank geht zunächst an Georg Maret als Leiter seiner tollen Arbeitsgruppe. Vielen Dank dafür überhaupt erst die Möglichkeit geschaffen zu haben das ich hier meine Masterarbeit schreiben konnte. Vielen Dank für die Hilfen beim Interpretieren von allerlei Ergebnissen und für die vielen Diskussionen während den Pausen.

Peter Keim möchte ich mindestens genauso sehr danken, der mit seiner tollen Art ein für mich optimales Arbeitsumfeld schafft. Danke nicht nur für die große Inspiration in Sachen Physik, sondern auch für Surf- und Segelstunden und die dazugehörigen Abende. Ich hoffe wir können noch eine lange Zeit zusammen arbeiten.

Ich möchte mich auch herzlich bei Dirk Ropers bedanken, der mir die Arbeit hier beigebracht hat und mich dann mit vielen Diskussionen weitergebracht hat. Durch seine offene Art konnten wir Dinge ausprobieren die ich nicht für Möglich gehalten hätte. Auch die Abende am Elektronenmikroskop mit selbst gebackenem Brot bleiben mir noch lange in Erinnerung.

Der gesamten Gruppe Maret möchte ich ebenfalls danken. Hoffentlich kann ich in dieser angenehmen Atmosphäre noch eine Weile im „Kinderzimmer“ bleiben.

Vielen Dank an Carola Ebenhoch, für ständige Unterstützung und Motivationsecken, es ist schön mit dir. Natürlich bedanke ich mich auch bei meinen Eltern, Uwe Siedentop und Margot Hurler und meiner Schwester Regine, auf die ich mich immer Verlassen kann.

Zum Abschluss möchte ich mich noch bei jedem Einzelnen unseres tollen Physik Semesters 2009/10 mitsamt Anhang bedanken, ohne das ich die wunderbaren sechs Jahre niemals so sehr genießen hätte können. Vielen Dank für die zahllosen Stunden, Hütten, durchzechten Nächten, Parties, Events und ADK-Runden.

Konec hry

You win!

Ach komm... eins geht noch !